LEIBNIZ-INSTITUT FÜR ATMOSPHÄREN PHYSIK
IAP

In situ measurements of small scale neutral and plasma dynamics in the mesosphere/lower thermosphere region

Dissertation
zur
Erlangung des akademischen Grades
doctor rerum naturalium (Dr. rer. nat.)
der Mathematisch-Naturwissenschaftlichen Fakultät
der Universität Rostock

vorgelegt von
Boris Strelnikov, geb. am 15.09.1975 in Omsk
aus Kühlungsborn

Rostock, 1.09.2006

Gutachter: Prof. Dr. Franz-Josef Lübken (Universität Rostock)
Prof. Dr. Klaus-Ulrich Grossmann (Bergische Universität Wuppertal)

verteidigt am: 15.12.2006

Contents

Chapter 1

Introduction

The upper part of the Earth's atmosphere—namely, the mesosphere/lower thermosphere (MLT) region (roughly from 50 to 120 km)—is of great scientific interest, since it is coupled to the atmospheric layers above and below. On one hand, dynamical processes propagating upward from the troposphere reach mesospheric heights and influence MLT dynamics. On the other hand, solar radiation penetrates well down to MLT altitudes and also influences dynamics and composition of this region. Also, through the circulation processes the MLT is dynamically coupled to other atmospheric layers.

Different scale processes (from centimeters up to thousands of kilometers) are ultimately interconnected. The present work is devoted to the experimental investigation of small-scale processes with characteristic length scales from centimeters to some kilometers. As will be shown further below, these small-scale processes play an essential role in the atmosphere, and the behavior of the entire atmospheric system can only be understood if we account for the small-scale processes.

1.1 General structure of the atmosphere

The distribution of the atmospheric constituents and physical properties of the atmosphere result from both dynamical and chemical processes. In the vertical direction the atmosphere is conventionally divided into layers according to the variation of temperature with height. These layers are called troposphere, stratosphere, mesosphere, and thermosphere, as shown in Fig. 1.1. The upper boundary of each layer is called "pause" (tropopause, stratopause, etc.). Fig. 1.1(right panel) shows a typical example of the temperature variation in the northern atmosphere for summer (solid) and winter (dashed). Fig. 1.1 also demonstrates that the Earth's atmosphere reveals a seasonal temperature variation with most pronounced differences around the mesopause heights at polar latitudes. Regarding terminology, one can also consider the *middle atmosphere*, which includes the stratosphere and mesosphere and which is from approximately 10 km to 100 km. Since the dynamical processes in all these atmospheric layers are coupled, one also considers the *upper atmosphere*, which starts from the stratopause (i.e., $50 - 60$ km) and extends higher up to approximately one thousand kilometers. The specific feature of the upper atmosphere region is that it is the transition region from the *homosphere* ($\sim 0 - 90$ km), where strong turbulent mixing results in a nearly constant mixing ratio of the primary constituents (O_2 and N_2), to the *heterosphere* (from $\sim 90 - 100$ km and higher up), where the diffusive separation in the Earth's gravity field prevails, leading to the increase of the mixing ratio of light elements with altitude. The upper border of the homosphere is also called *turbopause*, since it is also the upper limit of the region

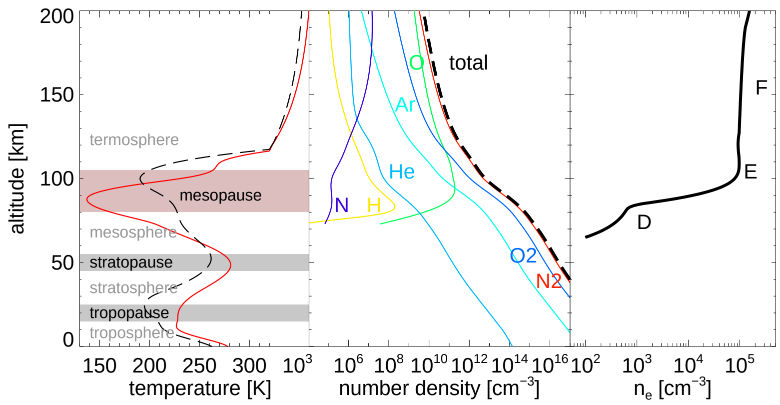

Figure 1.1: Left panel: Temperature variation derived from MSISE-90 model for high latitudes (69 °N). The solid line shows summer, and the dashed line shows winter temperatures. Middle panel: Number density of atmospheric neutral components (solid lines) and total neutral number density (bold dashed line) derived from MSISE-90 model [*Hedin*, 1991]. Right panel: Electron number density derived from IRI-2001 model [*Bilitza*, 2001] for the same latitude and summer season. Ionospheric regions ($D, E, and\ F$) are marked in the plot.

with effective turbulent mixing.

Fig. 1.1 (middle panel) also shows the composition of the atmosphere from ground up to 200 km derived from the empirical Mass-Spectrometer-Incoherent-Scatter (MSIS) model, which is based on experimental data of neutral temperatures and densities [*Hedin*, 1991]. Fig. 1.1 demonstrates that the composition of the atmosphere around the mesopause region is quite complicated, as are the dynamical processes in that region. On one hand, the solar ultra violet (UV) radiation still penetrates down to that altitude. On the other hand, surface layer perturbations (like, e.g., gravity waves) also penetrate into that region from below.

The COSPAR International Reference Atmosphere (CIRA), which is also based on experimental data, also includes the wind field measurements. It exhibits latitudinal variability of mean temperature and zonal wind as shown in Fig. 1.2. It is interesting to note that high latitudes receive the most solar energy in summer (24 hours). Also, much more solar energy absorption occurs at the mesopause heights than at the lower altitudes, but the mesopause at high latitudes in summer is nevertheless the coldest region of the terrestrial atmosphere. It can be seen either from Fig. 1.2(a) or Fig. 1.1 that the temperature difference between winter and summer at mesopause heights is $\sim 80\ K$. The zonal wind around polar summer mesopause (Fig. 1.2(b)) exhibits a change of sign (reversal): That is, the direction of the mean flow changes from a westwardly directed flow in the mesosphere to an eastwardly directed flow above the mesopause. These features (low temperatures and zonal wind reversal) of the polar summer mesopause cannot be explained by a simple consideration of, for example, radiative equilibrium. They deserve a deeper investigation accounting for wave activity and their dissipation, employing neutral dynamics and, of course, with the support of experimental studies.

The upper mesosphere acts as a filter for momentum transfer between the lower and upper parts of the atmosphere. Gravity waves that are created, for example, by strong ground-level winds forced into vertical motions by mountain ranges (orographic wind patterns) can propagate upward and interact with the background neutral atmosphere at mesospheric heights. The gravity waves being damped below ~100 km transfer their momentum and energy to the neutral air in this height region. During this process part of the energy is transferred to turbulent motion, and the momentum transfer results in substantial changes of the prevailing

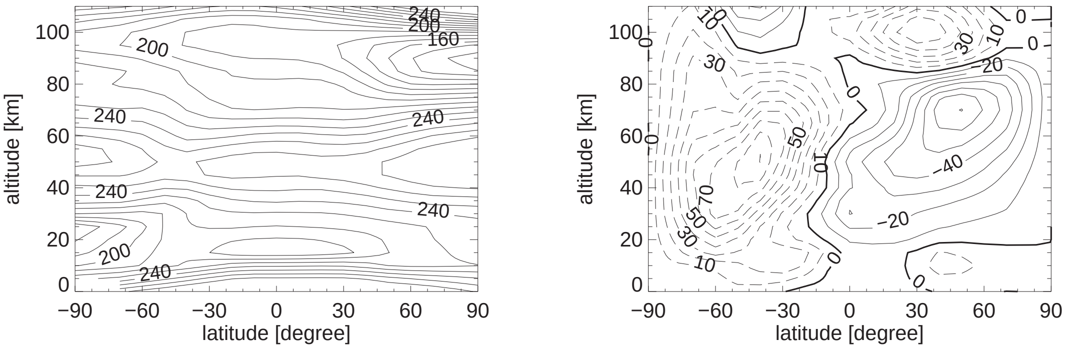

(a) Mean temperature in K.

(b) Mean zonal wind in m/s. Positive wind is eastwardly directed.

Figure 1.2: Latitudinal distribution of meteorological parameters derived from the CIRA-86 [*Fleming et al.*, 1988] for the middle of July.

wind field.

Solar UV radiation ionizes atmospheric components that create the ionosphere: that is, charged constituents, electrons and ions, also referred to as the ionospheric plasma. Fig. 1.1 also shows electron densities derived from the International Reference Ionosphere (IRI) model [*Bilitza*, 2001]. The ionosphere is conventionally divided into the regions D, E, and F, where the third can also be divided into F_1, and F_2. In the D-region ($\approx 60 - 90\ km$) the plasma density is small compared to the neutral air or total number density (factor of $\sim 10^{10}$ difference). The specific feature of the D-region is the presence of negative ions and ion clusters. The E-region ($\approx 90 - 130\ km$) plasma primarily consists of the molecular ions (O_2^+, NO^+, and N_2^+). The F_1-region ($\approx 130 - 180\ km$) is a transition region from the molecular ions to the atomic ions. The F_2-region is characterized by the main maximum of the plasma density in the upper atmosphere, which is formed by the O^+-ions and electrons. All these ionospheric regions are highly variable, and, in particular, there is a significant change between day and night.

The terrestrial ionosphere is also divided into three regions that have rather different properties due to their geomagnetic latitude. These are the low-latitude ($\sim 20° - 30°$ to both sides of the magnetic equator), mid-latitude (from $\sim 20° - 30°$ to $\sim 60°$ to either side of the magnetic equator), and high-latitude regions.

A short overview of ionospheric plasma properties at the high latitudes is given in section 1.2.2, which is followed by a more detailed investigation of some ionospheric plasma phenomena.

1.2 Significance of small scale processes

By small scales we understand spatial structures with characteristic length scales from centimeters to some kilometers. These structures appear as a result of dynamical processes like turbulence or wave breakdown (e.g., gravity waves and two-stream plasma waves).

1.2.1 Neutral air

In this section a modified version of the neutral dynamics equations [see e.g. *Holton*, 2004] is used to show the role of the small-scale atmospheric processes, which are also referred to as *eddies*, to distinguish them from the large-scale processes, referred to as the *mean* flow.

The role of small-scale processes in atmospheric circulation can better be understood by making use of the *transformed Eulerian mean* (TEM) equations introduced by *Andrews and McIntyre* [1976] to describe the wave-mean flow interaction. These equations are derived from the zonally averaged momentum and hydrodynamic equations defining the *residual meridional circulation* $(\overline{v}^*, \overline{w}^*)$. In the quasi-geostrophic approximation and in log-pressure coordinates, the TEM equations read [see e.g. *Holton*, 2004]:

$$\frac{\partial \overline{u}}{\partial t} - f_0 \overline{v}^* = \frac{1}{\rho_0} \nabla \cdot \mathbf{F} + \overline{X} \equiv \overline{G} \tag{1.1}$$

$$\frac{\partial \overline{T}}{\partial t} + \frac{\omega_B^2 H}{R} \overline{w}^* = \frac{\overline{J}}{c_p} \tag{1.2}$$

where $\overline{X}$ designates the mean zonal component of drag due to turbulent friction and $\overline{G}$ includes the effect of friction and waves. f_0 is the Coriolis parameter, and $\overline{u}$ and $\overline{T}$ are the longitudinally averaged zonal wind and temperature. t is time, H is the scale height, ω_B is the Brunt-Väisälä (buoyancy) frequency, $\overline{J}$ is the mean diabatic (Joule) heating rate, R is the universal gas constant, and c_p is the specific heat of air at constant pressure.

Meridional and vertical components of the residual circulation, $\overline{v}^*$ and $\overline{w}^*$, are linked by the continuity equation

$$\frac{\partial \overline{v}^*}{\partial y} + \frac{1}{\rho_0} \frac{\partial (\rho_0 \overline{w}^*)}{\partial z} = 0 \tag{1.3}$$

The quantity $\mathbf{F}$ appearing in Eq.1.1 is called the *Eliassen-Palm* (EP) flux. It is a vector in the meridional plane that has two components ($\mathbf{F} = \mathbf{j}F_y + \mathbf{k}F_z$), given by

$$F_y = -\rho_0 \overline{u'v'} \tag{1.4}$$

$$F_z = \rho_0 f_0 R \overline{v'T'} / (\omega_B^2 H) \tag{1.5}$$

where ρ_0 is mass density of the air and where primed quantities designate the longitudinally varying disturbances (referred to as eddies).

The TEM formalism shows explicitly that the effect of eddies on the mean flow is embodied entirely in one term $\overline{G}$. Two fluxes, the eddy momentum flux $(\overline{u'v'})$ and the eddy heat flux $(\overline{v'T'})$, are combined as components of the single EP flux $\mathbf{F}$.

If diabatic heating can be neglected ($\overline{J} = 0$), changes in zonal mean temperature $(\overline{T})$ occur entirely as an adiabatic response to the vertical component of the residual meridional circulation ($\overline{w}^*$-containing term in Eq. 1.2). Through the continuity equation (Eq. 1.3) a non-zero $\overline{w}^*$-value in turn arises from the momentum equation (Eq. 1.1), but only if the drag force $\overline{G}$ is non-zero. Therefore, $\overline{v}^* \neq 0$.

The non-zero EP-flux divergence, $\nabla \cdot \mathbf{F} \neq 0$, which leads to a non-zero residual circulation, $(\overline{v}^*, \overline{w}^*)$, results from wave dissipation processes (which create turbulence). Thus, the role of the dissipating eddies is to exert a zonal force, $\nabla \cdot \mathbf{F}$, which drives the residual meridional circulation.

A visualization of the residual meridional circulation calculated by *Becker and Schmitz* [2003] using a general circulation model (GCM) is shown in Fig. 1.3. The black contour lines show the residual mass stream function, Ψ, defined by: $(u, v, w) \equiv \mathbf{u} = \nabla\Psi$, and the direction of the mass flow is shown by arrows. The residual circulation reveals upwardly directed air motion in the summer hemisphere and downwelling in the winter hemisphere. Owing to the gravity wave dissipation, the momentum deposition results in a zonal drag between ~ 80 km and 100 km height, which is shown by the white contours.

The upwelling in the summer hemisphere adiabatically cools the middle atmosphere, leading to those extremely low mesopause temperatures as shown in Fig. 1.2(a).

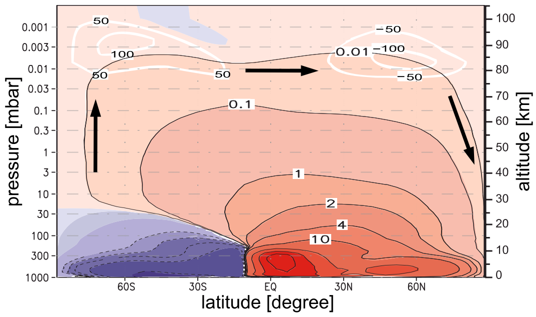

Figure 1.3: Residual mean meridional circulation (black lines) calculated using GCM model by *Becker and Schmitz* [2003]. The residual mass stream function is drawn with black contours in $10^9 kg/s$. The white contours give the total zonal drag (in $m \cdot s^{-1} day^{-1}$) owing to momentum deposition and vertical momentum diffusion generated by gravity waves saturation.

1.2.2 Plasma

Since the middle atmosphere contains not only neutral air but also ionized components, a complete understanding of the MLT dynamics requires also taking plasma properties into consideration. This is particulary important for the high latitudes.

At high latitudes the geomagnetic field lines are nearly vertical. This implies that magnetic field lines connect the ionosphere to the outer part of the magnetosphere, which is in turn driven by the solar wind. As a consequence, the high-latitude ionosphere is much more complicated than that of the low- or the mid-latitude region, and it is a sensitive indicator of coupling processes between different parts of the atmosphere.

The most specific features of the high-latitude ionosphere include the following:

- The high-latitude ionosphere is highly variable both in time and space.
- It is more accessible to the energetic particles. Moreover, at a certain place (polar cusp) the dayside ionosphere is directly accessible to energetic particles from the solar wind.
- The auroral zones are a specific feature of the high latitudes. Arrival of the energetic electrons from the magnetosphere causes "substorms," during which the ionization rate is greatly increased. High currents called electrojets can flow in a narrow layer of the auroral ionosphere. This in turn results in magnetic perturbations, which can also influence ground-based systems.

Small-scale plasma structures in the high-latitude ionosphere result either from neutral dynamical processes through collisions (i.e., in the dense D- and lower E- regions) or from plasma dynamical processes (see, e.g., Chapter 3).

Due to the high collision frequencies between the neutral air particles and the ions in the D- and lower E- regions, the neutrals will drag the ions along in their motion. Since ionospheric plasma and particularly the electrons are rather easy to observe due to their strong interactions with electromagnetic waves, the D- and lower E- region plasmas are often used as a tracer of the neutral gas [e.g. *Thrane and Grandal*, 1981; *Ulwick et al.*, 1988; *Kelley and Ulwick*, 1988; *Kelley et al.*, 1990; *Blix et al.*, 1990a; *Hall et al.*, 1992; *Hall et al.*, 1999].

Higher up, in the upper E- and in the F- regions, plasma density approaches neutral density, and plasma dynamical processes, like plasma instabilities, can influence the neutral air motions and also the heat and momentum budget of the atmosphere. Small-scale plasma irregularities are also used to study the high latitude convection patterns [e.g. **?***Mazaudier et al.*, 1987], ionospheric current distributions [e.g. *Andre and Baumjohann*, 1982], and other high-latitude phenomena.

1.3 Objectives and structure of the thesis

The present study is devoted to the experimental investigation of small-scale structures in the mesosphere/lower thermosphere (MLT) region (70 − 110 km height) at high northern latitudes (69 °N−79 °N) using in situ techniques. The main subject of this work is the small-scale structuring in the neutral air: that is, the neutral air turbulence. In addition, the small-scale structuring in the MLT plasma and its connection to the small scale neutral processes are also considered.

The main problems which are addressed in the presented study are:

neutrals :

1. Spatial organization of the turbulent patches.
2. The role of turbulence in the residual meridional circulation.
3. Latitudinal variability of the turbulence activity at northern latitudes.

plasma :

4. E-region plasma instabilities.
5. Connection of E-region plasma dynamical processes to neutral structuring.

The first point has been developed due to improvement in the analysis technique (section 5.4).

The understanding of the second problem has been experimentally improved since the MIDAS/MaCVAWE sounding rocket campaign in 2002 (section 6.1).

The third problem was first studied (using in situ measurement technique) during the ROMA/SvalRak sounding rocket campaign in 2003 (section 6.2).

This thesis is organized as follows. The chapters 2 and 3 describe the basic terms used in the presented work. The work begins with a description of neutral air turbulence, which is the major topic of this manuscript. This part is followed by an introduction to the small-scale plasma processes relevant for the MLT region. Chapter 4 contains a description of the rocket instruments used in this study. The turbulence analysis technique is described in Chapter 5. It contains both the standard method and the new technique, which is one of the novelties of the presented work. This new analysis technique implies some new geophysical results, which are highlighted in Chapter 5.4. Chapter 6 contains a description of two sounding rocket campaigns (MIDAS/MaCWAVE and ROMA/SvalRack), their results, and geophysical implications. This chapter starts with the MIDAS/MaCWAVE summer campaign (section 6.1). The ROMA/SvalRak campaign is then briefly reviewed, and subsequently the results of neutral and plasma dynamic studies are presented.

Chapter 8 summarizes the results of this work, followed by an outlook to future rocket soundings and anticipated results.

Chapter 2

Turbulence

This chapter presents an introduction of the basic concept and equations, which will help to describe the neutral air turbulence.

2.1 Energy spectrum

The kinetic energy distribution in the turbulent flow field can be described by the energy spectrum shown in Fig. 2.1. It shows how turbulent kinetic energy is distributed over the structures of different scales (eddies of different size). Fig. 2.1 shows an energy spectrum typical for the mesosphere. The ordinate shows the energy density, E. The lower abscissa represents the spatial scales of a turbulent structure, l, which are related to the wave number, k (upper abscissa in Fig. 2.1), as $l = 2\pi/k$. This spectrum can be split into several parts

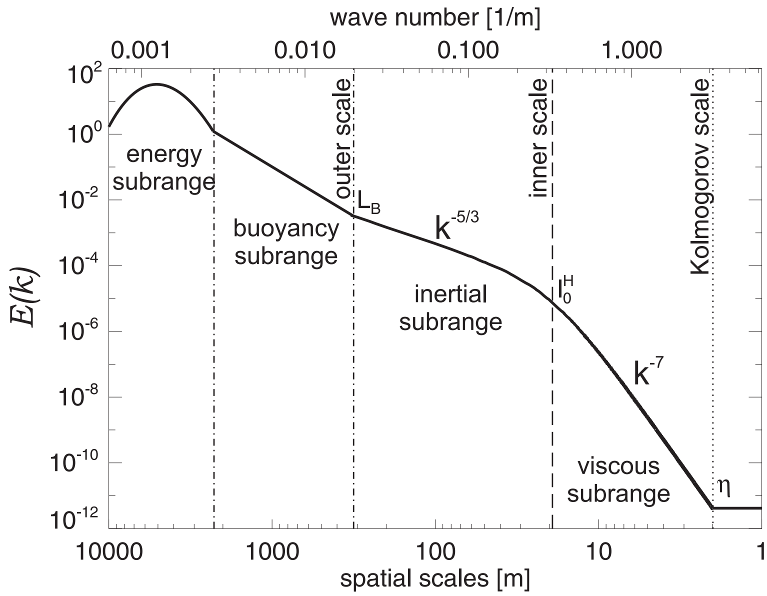

Figure 2.1: Energy spectrum (with typical for the mesosphere values). The spectrum was derived using the spectral model of *Heisenberg* [1948] for the altitude of ~85 km (i.e., kinematic viscosity $\nu = 1\ m^2/s$) and mean dissipation rate ($\varepsilon = 0.7\ mW/kg$) as measured by *Lübken et al.* [2002].

based on the physical processes that dominate at the considered scales. The left-most part of this spectrum (the largest scales) is believed to be the part where turbulence gets its energy (e.g,. from gravity waves) and is called energy subrange (ESR). This acquired kinetic energy is then transferred to the smaller scales by a process generally termed the energy cascade. The next part of the spectrum is called the buoyancy subrange (BSR), since buoyancy forces are dominating. The next two and the most important parts for our study are the inertial and viscous subranges (ISR and VSR, respectively). In the ISR the motion of the turbulent eddies is completely dominated by inertial forces. In the VSR the viscous dissipation plays a significant role: That is, the kinetic energy is dissipated to heat by viscous forces.

The inertial and viscous energy subranges are further considered in more detail, since our measurement technique (as well as most of the turbulent models) deals with this part of the energy spectrum. A mathematical description of the ISR was first derived by *Kolmogoroff* [1941] from dimensional reasoning and is well accepted to be $E(k) \propto k^{-5/3}$ for a one-dimensional spectrum. *Kolmogoroff* also estimated that the viscous part of the energy spectrum should have a much steeper slope. This part can well be described by an exponential law, $E(k) \propto exp(-k^2)$, [e.g. *Batchelor*, 1953; *Novikov*, 1961; *Tatarskii*, 1971; *Hill and Clifford*, 1978; *Driscoll and Kennedy*, 1983]. The energy spectrum in the VSR, however, can also be estimated from the dimensional reasoning, which yields $E(k) \propto k^{-7}$ [*von Weizsäcker*, 1948; *Heisenberg*, 1948]. One has to mention that even though the latest is not a mathematically rigorous description of the VSR, it agrees reasonably well with the exponential description and experimental results.

2.2 Characteristic scales

The energy subranges are limited by characteristic scales, which can be thought of as the sizes of turbulent eddies. The smallest possible size of a turbulent motion is estimated by the Kolmogorov scale (smaller eddies are completely destroyed by the molecular diffusion):

$$\eta = \left(\frac{\nu^3}{\varepsilon}\right)^{1/4} \tag{2.1}$$

where $\nu = \mu/\rho$ is the kinematic viscosity, μ is the dynamic viscosity, ρ is the mass density of air, and ε is the turbulent energy dissipation rate (see the next section).

The inertial forces, driving the eddy's motion in the ISR, begin to be dominated by the viscous forces at certain scales. This transition region defines the inner scale, l_0. The inner scale is defined differently in different models. To compare the inner scales, they can be derived from the models of *Heisenberg* [1948], *Tatarskii* [1971], and *Driscoll and Kennedy* [1983], which yield [*Lübken*, 1993]:

$$\begin{aligned} l_0^H &= 9.90 \cdot \eta \\ l_0^T &= 7.06 \cdot \eta \\ l_0^D &= 6.66 \cdot \eta \end{aligned} \tag{2.2}$$

respectively. The superscript designates the model. This means that comparing the inner scales of turbulence, one has to refer to the model used for the calculation and (if different models are used) take into account the discrepancy in l_0-values shown above.

For equal input parameters, however, these models result in a close η- and, therefore, ε-values because of the slightly different spectral shape in the VSR and within the ISR to VSR transition scales [see e.g. *Lübken et al.*, 1993; *Lübken*, 1993; *Giebeler*, 1995, for comparison of the l_0, η, and ε -values, derived using different models].

The largest scales within the ISR are defined by the outer (buoyancy) scale, L_B. Various formulae are used in the literature for determination of the buoyancy scale [see e.g. *Weinstock*, 1978; *Lübken et al.*, 1993; *Hocking*, 1999]. L_B values presented in the literature are, therefore, ambiguous and have to be considered as an estimate of this characteristic scale. Following *Lübken* [1992, 1993] we use:

$$L_B = 9.97\left(\frac{\varepsilon}{\omega_B^3}\right)^{1/2} \tag{2.3}$$

where ω_B is the Brunt-Väisälä (buoyancy) frequency and ε is the turbulent energy dissipation rate.

2.3 Strength of turbulence

The common way to quantify the influence of turbulence on the mesosphere is to derive the turbulent energy dissipation rate, ε: that is, the rate at which kinetic energy is transferred to heat. It is defined as [e.g. *Landau and Lifschitz*, 1966]:

$$\varepsilon = \frac{\nu}{2}\overline{\left(\frac{\partial u_i}{\partial x_j}\right)^2} \tag{2.4}$$

where ν is kinematic viscosity, u_i is i-th component of the velocity, and x_j is the j-th cartesian coordinate.

This quantity can also be converted to a heating rate considered to be an equivalent characteristic:

$$Heating\ rate \equiv \frac{\partial T}{\partial t} = \frac{\varepsilon}{c_p} \tag{2.5}$$

where c_p is the heat capacity of air at a constant pressure ($c_p \approx 1004\ J \cdot kg^{-1} K^{-1}$).

Turbulence can also be described in terms of eddy diffusion, which is analogous with the molecular diffusion [e.g. *Zimmerman and Murphy*, 1977]. This introduces the turbulence (eddy) diffusion coefficient for momentum, K, which is usually derived from the expression [e.g. *Weinstock*, 1978; *Hocking*, 1999]:

$$K = C_K \cdot \frac{\varepsilon}{\omega_B^2} \tag{2.6}$$

where the constant C_K normally ranges from 0.2 to 1.25 [*Hocking*, 1999]. Such an ambiguity in the choice of this constant implies an additional uncertainty and makes it difficult to compare different measurements. Since in most cases the only important velocity gradients are the vertical shears of horizontal winds ($\partial u/\partial z$), it can be shown [e.g. *Lübken*, 1993] that $C_K = Ri$, where Ri is the Richardson number. In our calculations we use $C_K = Ri = 0.81$ [*Lübken*, 1992, 1993, 1997; *Lübken et al.*, 1993].

2.4 Sources of MLT turbulence

Kelvin-Helmholtz shear instability and gravity wave breaking are believed to be the two major sources of turbulence generation near the mesopause [see e.g. *Fritts et al.*, 2003]. The two flows both share common characteristics related to turbulence transition, evolution, and duration, and they exhibit a number of differences that have important implications for layered structures and atmospheric observations at mesopause altitudes. Common features related to layering include sharp, local gradients in turbulent kinetic energy production, dissipation, and magnitude as well as a clear spatial separation of the maxima of turbulent kinetic energy dissipation and thermal dissipation accompanying vigorous turbulence. Differences arise because shear instabilities cause turbulence and mixing confined by stratification to a narrow layer, whereas gravity wave breaking leads to a maximum of turbulence activity that moves with the phase of the wave [*Fritts et al.*, 2003; *Achatz*, 2005]. As a result, the effects of turbulence due to shear instability likely persist for much longer than those of turbulence due to gravity wave breaking [see e.g. *Müllemann et al.*, 2003, where different sources of MLT turbulence were experimentally identified].

2.5 Mesospheric turbulence: Overview of in situ soundings

Experimental studies of turbulence at the northern latitudes around the mesopause heights have been intensively conducted in the last two decades, using different in situ and remote sensing techniques. Due to numerous rocket soundings, the observational data base of the in situ measured turbulence parameters has grown. This allowed the deduction of mean values that reflect a "normal" state of turbulence of the high-latitude MLT region. The results of these previous in situ turbulence measurements are discussed and summarized elsewhere [see *Thrane et al.*, 1994; *Lübken*, 1997; *Hall et al.*, 1999; *Lübken et al.*, 2002]. These studies yielded the following:

- ✓ ε-profile with vertical resolution of one kilometer derived from the in situ measurements of neutral density fluctuations.
- ✓ Estimate of characteristic scales of mesospheric turbulence.
- ✓ Comparison of the results deduced from the measurements of the different tracers: Plasma and neutrals.
- ✓ Comparison of the results deduced using different methods and spectral models.

The mean profile of the strength of turbulence, ε, derived from measurements of neutral air density fluctuation in summer at Andøya (69 °N), is shown in Fig. 2.2(a). This shows that neutral air turbulence activity in the MLT region <u>in summer</u> is confined to a quite narrow altitude region from 82 to 95 km, with the strongest part being at around the mesopause (~87 km). In situ measurements also show that turbulence appears in thin layers with a typical vertical extent of several kilometers (it is not seen from Fig. 2.2).

The dashed line shows an estimate of the smallest possible inner scale of turbulence, l_{min} [*Lübken*, 1993; *Lübken et al.*, 1993; *Strelnikov et al.*, 2003]. This value can be derived if we set the extent of the inertial energy subrange to zero or, equally, $L_B = l_0$. This implies $\varepsilon_{min} = \nu\omega_B^2$. The same result can be derived by assuming that the eddy diffusion coefficient equals the molecular diffusion coefficient, $K = D$. We emphasize that this is only an estimate and cannot be considered as an absolute physical limit. Note that from the definition of the energy dissipation rate (Eq. 2.4), there is no global minima in the ε-field.

Typical length scales of the smallest turbulent eddies (Kolmogorov scale) in the MLT region range from tens of centimeters to tens of meters. The inner scale, l_0, of MLT turbulence can vary from ten to hundreds of meters, as schematically shown in Fig.2.2(b). The estimate of the outer (buoyancy) scale, L_B, gives values from hundred meters to some kilometers.

Briefly, the current status of our knowledge is the following.

1. At Andøya (69 °N) in summer, turbulence is always acting around the mesopause heights.
2. Typical turbulence energy dissipation rates lie within the range $0.5 - 200$ mW/kg (heating rate $0.04 - 20$ K/d).

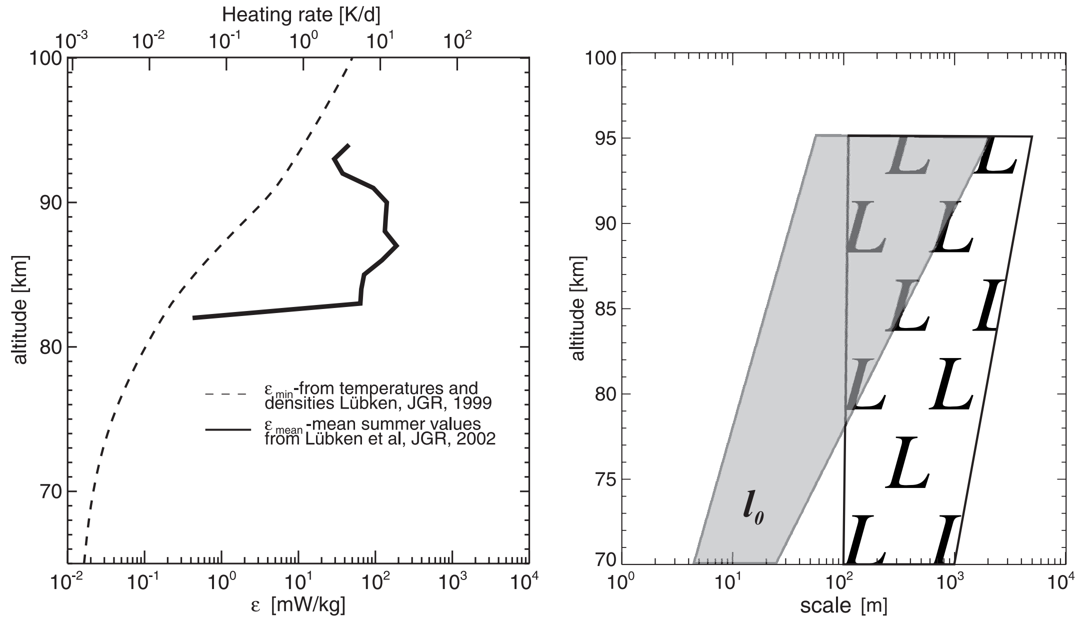

(a) Mean strength of turbulence as kinetic energy dissipation rate, ε in mW/kg, or heating rate in K/day. After *Lübken et al.* [2002].

(b) Characteristic scales of turbulence. l_0 designates the inner scale, and L is the outer scale (see section 2.2). After *Lübken* [1997].

Figure 2.2: Mean summer turbulence characteristics derived from the in situ measurements.

3. The corresponding inner scales, l_0^H, range from ∼10 to ∼50 meters (or Kolmogorov scale, η, from ∼1 to ∼5 m).

4. The outer (buoyancy) scale can vary from ∼100 m to a couple of kilometers.

5. The entire region of the turbulence activity is confined to the altitudes from 82 to 95 km.

6. The vertical extent of a single turbulent patch varies from at least 1 km (resolution of the technique) to ∼6 km.

2.6 Mesospheric turbulence: Open issues

Aside from the progress in the experimental studies of MLT turbulence, there are still many open questions, some of which this work aims to address.

These questions include the morphology and time development of turbulent structure. By morphology we mean whether the structure is isotropic, two- or three-dimensional, and homogeneous; what the mean width of MLT turbulence patch is; and also the probability distribution of a different thickness of turbulence. By time development we mean the following: It is already well accepted that turbulence passes through different stages of development, which are referred to as *active, active-fossil*, and *fossil* turbulence [see e.g. *Gibson*, 1999]. At each stage turbulence reveals different characteristics (such as scales, energy dissipation rate) and properties (such as mixing, heat and momentum transfer). These differences allow us to identify the stage of development and estimate the lifetime of the structure. This has never been done yet for the MLT turbulence.

Models used in the studies of the mesospheric turbulence (see previous sections) draw on some assumptions about the morphology of turbulence (homogeneity, isotropy, and three-dimensionality), and they also suggest that we deal with a fully developed active turbulence. This can lead to errors in estimating the strength of turbulence.

This work does not aim to answer the fundamental turbulence theory questions. The intention is rather to deduce the geophysical implications of the neutral air turbulence in the dynamics of the MLT region.

Thus, using the new analysis method (section 5.3), which decomposes measured time series into time−frequency (in our case, the same as altitude−spatial scale) space, the work aims to gain insight into the morphology of the MLT turbulence (Chapter 5.4). This technique allows a qualitative scale analysis and makes a quantitative study of the MLT turbulence possible. Also, a potential of the new data analysis technique in conjunction with our future soundings is discussed in Chapter 8.

Although significant advances in theoretical understanding of the role of turbulence in the large-scale circulation have been achieved (see section 1.2), and although some experimental evidence has also been found, the most consistent and comprehensive set of independent simultaneous measurements that consistently supports our current understanding of the significance of MLT turbulence in the atmospheric system is introduced in this manuscript. In section 6.1 the small-scale neutral dynamics (turbulence activity) in the MLT region is connected to the planetary-scale processes (global circulation). This experimental evidence reveals the role of MLT turbulence in the planetary atmosphere.

Aside from the local spatial organization (which we called "morphology"), since turbulence plays an essential role in the planetary atmospheric circulation, it is also important to know the latitudinal distribution of the MLT turbulence. In section 6.2 the first in situ turbulence measurements (the most precise to date) conducted at very high northern latitudes (79 °N) are presented. These results are then further discussed in section 6.2.4, where our observations are compared to the results of a mechanistic general circulation model and scrutinize the underlying physical causes leading to the presented model state.

Chapter 3

Plasma

3.1 Ionospheric conductivity

The presence of free electrons and ions allows the ionospheric layers to carry currents in the presence of electric fields. At high latitudes the ionospheric conductivity and, therefore, currents become very large and become a major factor in the behavior of the ionosphere.

In the absence of a magnetic field, the conductivity of the ionized gas is simply the product of the total charge per unit volume, Ne, with the mobility of the charge carrier (its velocity in a unit electric field), $e/(m\nu)$ [see e.g. **?***Hunsucker and Hargreaves*, 2002]:

$$\sigma_{||} = \frac{Ne^2}{m\nu} \tag{3.1}$$

where N is the number density of particles with charge e, ν is the collision frequency of these particles with neutrals, and m is the mass of the particles. If different charge carriers are presented, then the total conductivity is the sum of the conductivities of each species.

In the presence of a magnetic field, the Lorentz force will interact with the velocity component of the charged particles, which is perpendicular to the magnetic field. This leads to the conductivities [see e.g. *Hunsucker and Hargreaves*, 2002]:

$$\sigma_P = \left(\frac{N_e}{m_e \nu_e} \frac{\nu_e^2}{(\nu_e^2 + \omega_e^2)} + \frac{N_i}{m_i \nu_i} \frac{\nu_i^2}{(\nu_i^2 + \omega_i^2)} \right) e^2 \tag{3.2}$$

$$\sigma_H = \left(\frac{N_e}{m_e \nu_e} \frac{\nu_e \omega_e}{(\nu_e^2 + \omega_e^2)} - \frac{N_i}{m_i \nu_i} \frac{\nu_i \omega_i}{(\nu_i^2 + \omega_i^2)} \right) e^2 \tag{3.3}$$

The subscripts e and i refer to electrons and ions, respectively. $\omega = eB/m$ is the gyrofrequency, where B is Earth's magnetic field.

The quantities $\sigma_{||}, \sigma_P$, and σ_H are called *parallel*, *Pedersen*, and *Hall* conductivities respectively. The parallel conductivity results in the current, $j_{||}$, which is parallel to the magnetic field. As collisions with neutrals become more numerous, $\sigma_{||}$ decreases. The opposite is true for the perpendicular conductivities, σ_P and σ_H, which only exist due to collisions. Without collisions the drift velocity perpendicular to the magnetic field will be equal for ions and electrons: however, when ν_i becomes larger than ν_e, this difference results in a relative difference in the drift velocities and, therefore, in ionospheric currents. Conductivities σ_P and σ_H result in the currents j_P and j_H, respectively, which are perpendicular to the magnetic field. The Pedersen current, j_P, flows in the direction of the electric field. The Hall current, j_H, flows perpendicular to both E- and B- fields.

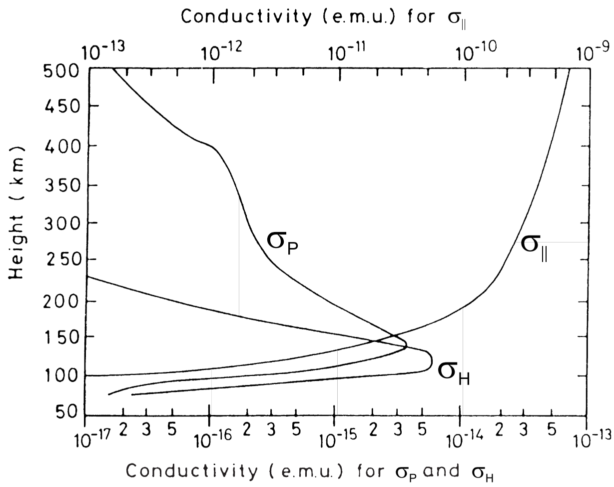

Figure 3.1: Height profiles of the ionospheric conductivities calculated for middle latitude at noon (Akasofu and Chapman, after *Hunsucker and Hargreaves* [2002]). To convert to the SI units ($\Omega^{-1}m^{-1}$), σ-values have to be multiplied by 10^{11}.

As it is seen from Eqq. 3.2 and 3.3, these conductivities depend on the ratio ω/ν and are, therefore, height-dependent. Fig. 3.1 shows typical curves for the variation of $\sigma_{||}, \sigma_P$, and σ_H with altitude. This demonstrates that up to the lower F-region, the Hall conductivity, σ_H, plays a major role, whereas in the upper ionosphere the parallel conductivity, $\sigma_{||}$, heavily dominates.

To calculate the Hall and Pedersen conductivities, σ_H and σ_P, we need to know the ion and electron densities, N_i and N_e, and their collision frequencies, ν_i and ν_e.

The ion-neutral collision frequency, ν_i, can be derived as [e.g. *Schunk and Nagy*, 2004]:

$$\nu_i = 2.21\pi \frac{n_n m_n}{m_i + m_n} \left(\frac{\gamma_n e^2}{\mu_{in}} \right)^{1/2} \tag{3.4}$$

where m_i is mean ion mass in amu, m_n and γ_n are the mean mass (in amu) and polarizability (in 10^{24} cm^3) of neutral gas of a certain sort, respectively, and n_n is the neutral air number density in cm^{-3}. To calculate full collision rate between ions and neutrals, one has to sum over the neutral gas components (see Fig. 1.1). Experimentally derived polarizabilities, γ_n, for different neutral gases can be found in the literature [see e.g. *Schunk and Nagy*, 2004, Table 4.1].

The electron-neutral collision frequency, ν_e, depends on neutral density, n_n, and electron temperature, T_e, as [e.g. *Schunk and Nagy*, 2004]:

$$\nu_e = (3.78 \cdot 10^{-11}\sqrt{T}e + 1.98 \cdot 10^{-11} Te) \cdot n_n \tag{3.5}$$

where n_n is in cm^{-3} and T_e in K.

Fig. 3.2 shows calculated collision frequencies typical for high northern latitudes. It demonstrates that below ~130 km the ion-neutral collision rate significantly exceeds the electron-neutral collision rate, which makes ions become strongly coupled to neutral air in the lower ionosphere.

Fig. 3.3 shows gyro- to collision-frequency ratios derived from in situ measurements conducted at 79 °N (see chapter 7 and *Strelnikov et al.* [2007]). It shows that starting from ~75 km and higher up, electrons are magnetized ($k = \omega/\nu > 1$), whereas ions are non-magnetized ($k = \omega/\nu < 1$) below ~110 km.

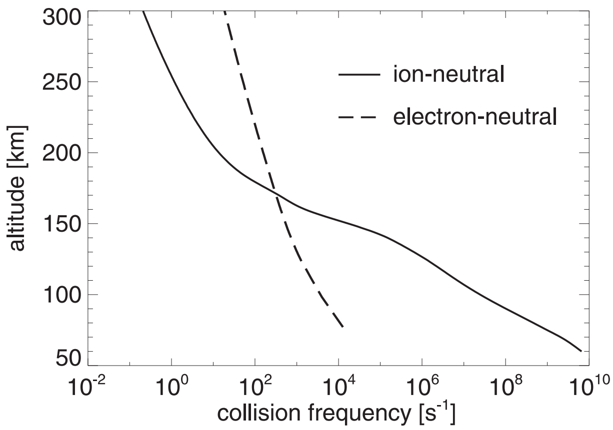

Figure 3.2: Ion-neutral (solid) and electron-neutral (dashed) collision frequencies calculated using Eqq. 3.4 and 3.5 and models MSISE-90 [*Hedin*, 1991] and IRI-2001 [*Bilitza*, 2001].

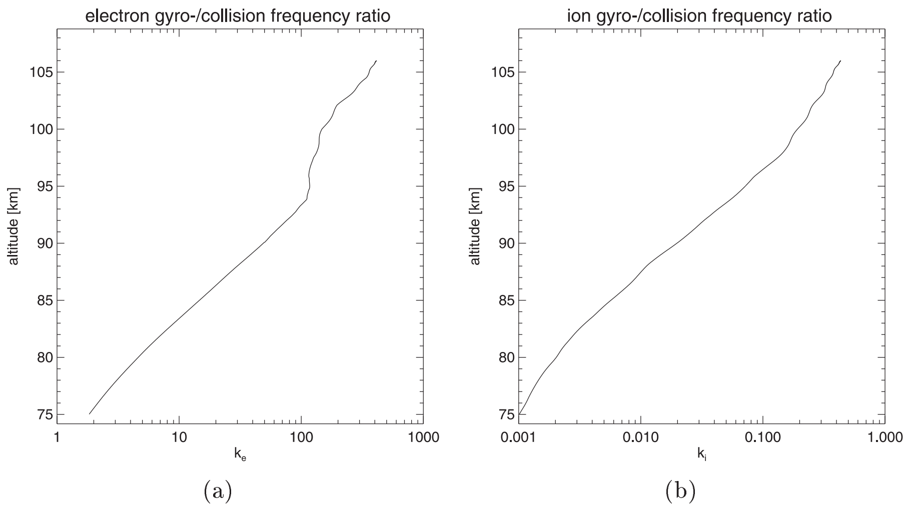

Figure 3.3: Gyro-to-collision frequency ratios calculated using in situ measurements at 79 °N, by *Strelnikov et al.* [2007].

3.2 Ionospheric currents

The relationship between currents and electric field is given by the generalized Ohm's law: $\mathbf{j} = \sigma \cdot (\mathbf{E} + \mathbf{v} \times \mathbf{B})$, where $\mathbf{v}$ is the velocity of the reference frame where the electric field, $\mathbf{E}$, is measured. Note that $\mathbf{E}$ is different in different frames of reference, while $\mathbf{E} + \mathbf{v} \times \mathbf{B}$ is an invariant equal to $\mathbf{E}$ in the frame of reference where $\mathbf{v} = 0$. In ionospheric physics one usually takes $\mathbf{v} = \mathbf{v_n}$, where $\mathbf{v_n}$ is the velocity of the neutral gas. Thus, for the ionospheric current density one can write [e.g. **?**]:

$$\mathbf{j} = \sigma_P(\mathbf{E}_\perp + \mathbf{v_n} \times \mathbf{B}) + \sigma_H \mathbf{B} \times (\mathbf{E}_\perp + \mathbf{v_n} \times \mathbf{B})/B + \sigma_{||}\mathbf{E}_{||} \tag{3.6}$$

Here $\mathbf{E}_{||}$ and $\mathbf{E}_\perp$ are the components of the ionospheric electric field, which are parallel and perpendicular to the Earth's magnetic field, $\mathbf{B}$, respectively.

In the upper ionosphere, because the parallel conductivity, $\sigma_{||}$, is very high, the electric field component $E_{||}$ along the geomagnetic field lines will generally be much smaller than the perpendicular field components $E_\perp$. Geomagnetic field lines can often be considered as perfectly conducting. At high latitudes this implies that ionospheric layers at different altitudes are effectively coupled, and this in turn means that the horizontal electric field becomes almost height-independent. This also leads to the concept of height-integrated conductivities [e.g. **?**]:

$$\begin{aligned} \Sigma_P &= \int \sigma_P \cdot dh \\ \Sigma_H &= \int \sigma_H \cdot dh \end{aligned} \tag{3.7}$$

and height-integrated current density [A/m]:

$$J = \int j \cdot dh \tag{3.8}$$

where integration must be done over the altitude region where ionospheric currents flow (usually 90-120 km).

Another conductivity that is sometimes used is the Cowling conductivity. It is given by:

$$\sigma_C = \sigma_P + \frac{\sigma_H^2}{\sigma_P} \tag{3.9}$$

It relates to the power dissipation or Joule heating due to the currents that are transverse to the magnetic field, per unit volume, given by:

$$Q = j_\perp \cdot (\mathbf{E}_\perp + \mathbf{v_n} \times \mathbf{B}) = \sigma_P(\mathbf{E}_\perp + \mathbf{v_n} \times \mathbf{B})^2 = \frac{j_\perp^2}{\sigma_C} \tag{3.10}$$

3.3 E-region plasma instabilities

Strong ionospheric currents in the height region from 90 to 120 km at high latitudes are known as the auroral electrojet. These currents produce plasma irregularities and can lead to plasma instabilities: that is, plasma waves that grow in time exponentially or faster. Plasma irregularities in the auroral electrojet region have been studied for over six decades both theoretically and experimentally [for reviews on both the theory and the observations see **????***Fejer*, 1996].

The two primary plasma instabilities in the E-region are the two-stream and gradient drift instabilities. The two-stream instability is the fundamental mechanism responsible for direct generation of small-scale irregularities in the electrojet plasma (from centimeters to tens of meters). The gradient drift instability in turn creates plasma irregularities at spatial scales from tens of meters to some kilometers, which in our terminology is still a small-scale structure. The driving force for the two-stream and gradient drift instabilities is the electric field.

Under the influence of a horizontal electric field and Earth's nearly vertical magnetic field, electrons and ions drift perpendicular to both the E- and B-field ($\mathbf{E} \times \mathbf{B}$ drift). Electrons can move very quickly, whereas ions are collisionally dominated, and their velocities are, therefore, much smaller. This results in a relative drift between ions and electrons with a velocity $\mathbf{V_D} = \mathbf{V_e} - \mathbf{V_i}$, which is the difference between the electron stream velocity $\mathbf{V_e}$ and ion stream velocity $\mathbf{V_i}$. If this drift velocity exceeds a threshold value, an instability develops. The threshold condition was first derived by **?** and **?**:

$$V_D \geq C_s(1 + \psi_0). \tag{3.11}$$

In this equation ψ_0 is defined as $\psi_0 = \nu_e \nu_i / \omega_e \omega_i$, where ν_i is the ion-neutral collision frequency, ν_e is the electron collision frequency with neutrals, and C_s is the ion acoustic velocity given by:

$$C_s = \sqrt{k_B(T_i + T_e)/m_i} \tag{3.12}$$

where k_B is Boltzmann's constant and T_i and T_e are the ion and electron temperatures.

The gradient drift instability develops if, additionally to the electric field, gradient in the background plasma density takes place. In contrast to the two-stream mechanism, this type of instability does not need a strong electric field.

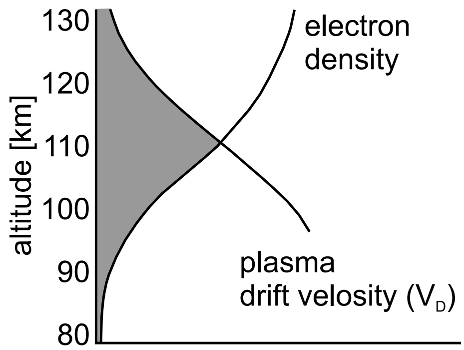

Figure 3.4: The altitude of occurrence of E-region plasma instabilities. Electron density grows with height, and plasma drift velocity, V_D, decreases with altitude. The shaded area shows the altitude range where plasma instabilities can develop. After **?**.

The altitude of occurrence of E-region plasma instabilities is schematically shown in Fig. 3.4. It shows a typical profile of electron density, which grows with height, and a profile of the plasma drift velocity, V_D, which decreases with altitude because the ion drift velocity, V_i, approaches the electron drift velocity, V_e, due to decreasing collision frequency (see Fig. 3.2). The typical plasma drift velocities observed at high northern latitudes range from some meters per second to some thousands m/s [see e.g. *Fejer*, 1996; *Hunsucker and Hargreaves*, 2002; *Schunk and Nagy*, 2004].

Other physical mechanisms have been proposed to explain plasma irregularities, but such instabilities occur comparatively rarely, and their effects are rather small [see e.g. *Fejer*, 1996].

Chapter 4

Experimental technique

In this chapter our general concept of measuring mesospheric turbulence is described and a short overview of the in situ techniques used for this purpose is given. In section 4.5 a short description of the rocketborne instruments involved in this work is presented, and in the following subsections a more detailed description of two instruments that are the main data providers for the presented study are given.

4.1 In situ vs remote soundings

For a review of the different MLT turbulence measurement techniques, the reader is referred to [e.g. *Lübken*, 1993; *Hocking*, 1999; *Hall et al.*, 1999]. Each technique, remote radar soundings or in situ measurements, has its own advantages. The strengths of the in situ measurements [discussed in e.g. *Lübken*, 1993] are that they are able to measure very small-scale structures (i.e., down to centimeter-scales) and at the same time allow measurement of a wide range of scales, covering both the ISR and VSR. This yields the energy spectrum (section 2.1, Fig. 2.1) with a resolved dissipating part (viscous subrange), which in turn allows application of the spectral model method (see below) to quantify turbulence.

4.2 Turbulence: In situ detection techniques

Since it is not possible in the Mesosphere/ Lower Thermosphere (MLT) region to measure the velocity fluctuations directly (with sufficient spatial, temporal, and spectral resolution), the different tracers are used to study the effects produced by the turbulence and thereby to draw conclusions on turbulence parameters. A simple schematic shown in Fig. 4.1 demonstrates how turbulence creates signatures in different quantities like temperature or density so that these quantities can be used as a tracer for turbulence.

A turbulent eddy mechanically moves an air parcel to a different height. The time of collisional relaxation inside the air parcel is large compared to the time of the mechanical transport by the turbulent motion, so this process can be considered as adiabatic. As a result, the temperature (or density) at that new location will deviate from the background temperature (density) profile. *Hillert* [1992] and *Lübken* [1993] showed that for the MLT region this deviation is expected to be of the order of $\sim$ 1 − 2 %.

The microstructure of the temperature field was also examined in detail, e.g., in *Oboukhov* [1949]; *Yaglom* [1949]; *Corrsin* [1951], and *Batchelor* [1958]. *Tatarskii* [1971] summarizes some of these works and shows that the temperature and density fluctuations describe the turbulent field similarly to how it describes the velocity field. He also shows that density

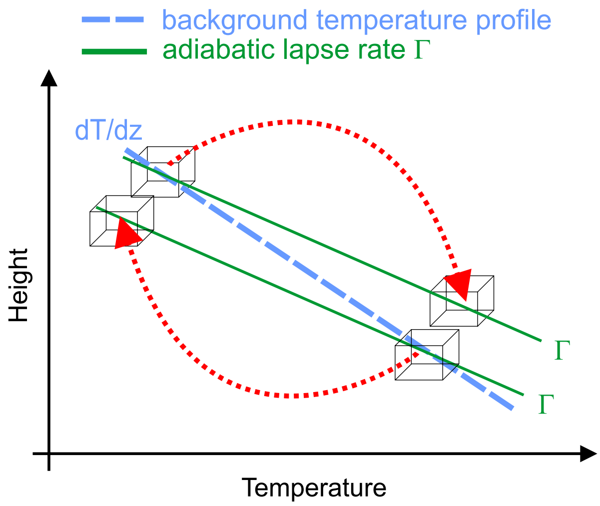

Figure 4.1: Turbulent eddies adiabatically move an air parcel to a different height. This creates fluctuations of quantities like temperature or density.

fluctuations are suitable tracers for turbulent velocity fluctuations. The density fluctuations can be described by the equations of the same type as for velocity fluctuations.

Thus, one can use not only the density as a tracer of turbulence but also other properties or substances like humidity, permittivity, etc. The only requirement is that the tracer must be passive and conservative: that is, it can be affected only by turbulent motions and must not in turn disturb the turbulent field.

It is necessarily to notice here that in that respect the temperature is not a rigorous passive tracer, since the buoyancy force appearing due to temperature deviation from its mean value will influence the turbulence regime: however, if temperature fluctuations are small compared to the background temperature field, the mentioned effect is not significant. The density fluctuations in turn are not influenced by this effect [*Tatarskii*, 1971].

The tracers used in the mesospheric turbulence studies are different substances, released from the rockets (like chemical releases or chaff clouds, [e.g. *Blamont*, 1963; *Zimmerman and Champion*, 1963; *Roper*, 1966; *Lloyd et al.*, 1972; *Rees et al.*, 1972]), meteor trails [e.g. *Kelley et al.*, 2003], or natural atmospheric constituents [e.g. *Thrane and Grandal*, 1981; *Thrane et al.*, 1987; *Blix et al.*, 1990a; *Lübken*, 1992]. The first turbulence measurements that made use of the density fluctuations as a tracer were based on the measurements of small-scale plasma density variations [e.g. *Thrane and Grandal*, 1981; *Thrane et al.*, 1987; *Ulwick et al.*, 1988; *Kelley and Ulwick*, 1988; *Kelley et al.*, 1990; *Blix et al.*, 1990a, b; *Blix and Thrane*, 1991]. It was then shown that the plasma–namely, electrons and positive ions–can be affected by non-turbulent processes like enhanced recombination of electrons with cluster ions [*Röttger and La Hoz*, 1990], the effect of charged ice particles in PMSE [*Cho et al.*, 1992], or plasma instabilities [*Blix et al.*, 1994]. Thus the plasma irregularities can be used as a tracer for turbulence only conditionally in a limited altitude region which is not well defined and that has to be estimated from the conditions of each particular experiment: however, it was also shown that the relative fluctuations of neutral air density are a more universal tracer for the in situ turbulence measurements in the MLT region [*Lübken*, 1993; *Thrane et al.*, 1994]. The "TOTAL" instrument (the name emphasizes that total number densities are measured) was developed by the atmospheric physics laboratory at Bonn University [*Lübken*, 1987; *Hillert*, 1992; *Lübken*, 1993; *Hillert et al.*, 1994, and references therein]. The TOTAL is basically an ionization gauge adapted to the measurements under the mesospheric conditions. This instrument was successfully launched in 16 sounding rocket flights [see the list in e.g. *Rapp et al.*, 2001].

This concept of using ionization gauges onboard the sounding rockets was then further developed, and the "CONE" instrument (COmbined sensor for Neutrals and Electrons, which is the improved version of the "TOTAL") was developed by the same group [*Giebeler et al.*, 1993]. This instrument was also successfully launched in 19 sounding rocket flights [*Lübken*, 1992, 1997; *Müllemann et al.*, 2002, and references therein] and is still intensively being used in experimental studies of MLT dynamics [e.g. *Strelnikov et al.*, 2006]. The results of all these measurements up to the year 2000 are summarized in *Lübken* [1997] and *Lübken et al.* [2002].

We use relative density fluctuations as a tracer of turbulence [e.g. *Lübken*, 1992, 1993; *Lübken et al.*, 2002; *Müllemann et al.*, 2002; *Strelnikov et al.*, 2003, 2006]. Therefore, only the in situ methods based on the measurements of such fluctuations are considered here. All such techniques are based upon the following concept.

An instrument measures in situ a height profile (that is, a one-dimensional section of a real atmospheric structure) of relative (plasma or neutral) density fluctuations. Then the Fourier power spectral density of the measured altitude profile is derived and analyzed in terms of its spectral shape.

The presence of an inertial energy subrange (that is, the part of the spectrum characterized by a $k^{-5/3}$ spectral dependence) indicates the presence of turbulence. Investigators of the MLT region turbulence usually follow the work of *Lübken* [1992] if their measurements resolve both the inertial and viscous energy subranges, and fit the Heisenberg model [*Heisenberg*, 1948] to the measured power spectrum [e.g. *Croskey et al.*, 2004; *Lehmacher et al.*, 2006].

From this fit we derive the "breakpoint" of the spectrum (the inner scale, l_0): i.e., the transition scale from the inertial to the viscous subrange. From the inner scale and the atmospheric background parameters using Eqq. 2.1 and 2.2, the energy dissipation rate, ε, is finally derived.

As a final quantitative result of turbulence measurements in the MLT region, the altitude profile of the turbulence energy dissipation rate, ε, is usually supplied [e.g. *Lübken et al.*, 1993; *Lübken*, 1997; *Hocking*, 1999; *Lübken et al.*, 2002; *Müllemann et al.*, 2002; *Rapp et al.*, 2004; *Strelnikov et al.*, 2006].

Two primary methods used to deduce the ε-profile from the in situ measurements are the so-called structure function constant, C_n^2, -method [*Blix et al.*, 1990a, applied primarily to the plasma density measurements] and the spectral model method [*Lübken*, 1992, 1993, 1997; *Lübken et al.*, 1993]. We use the spectral model method to derive the turbulence strength, ε, from our measurements. As pointed out by *Lübken* [1992, 1993, 1997], an advantage of the spectral method is that it does not depend upon the constants (appearing in the C_n^2-method) that cannot be measured or precisely derived, e.g., from models. In the following subsection the spectral model method is explained in detail.

Spectral model method

The spectral model method is based on the idea that the spatial structure in a limited altitude range (which is identical to the temporal evolution of eddies at a fixed point if we assume ergodicity–i.e., that the time mean is equal to the space mean almost everywhere) of a turbulent tracer can be described by an analytical expression in terms of energy spectral density as a dependence of the size of the structure (spectral model). This expression includes turbulence parameters that can be unambiguously derived by comparing the model spectrum with the measured spectrum. Such models describe the inertial and viscous parts of the energy spectrum (Fig. 2.1, section 2.1). This implies that to be able to apply the spectral model method, one needs to have measurements that resolve both the ISR and VSR. For the mesospheric studies, that means we need to resolve spatial structures of the size from some meters to approximately one kilometer [see e.g. *Lübken*, 1992].

This method is further demonstrated on the *Heisenberg* [1948] spectral model. In the inertial subrange this model exhibits the classical $k^{-5/3}$ power law, and in the viscous subrange this model obeys the k^{-7} power law. Between these subranges a smooth transition takes place. Fig. 2.1 shows the spectrum as derived from the Heisenberg model. The energy vs frequency spectrum in this model is given by:

$$W(w) = \left[\frac{\Gamma(5/3)\sin(\pi/3)}{2\pi v_R}\right] C_n^2 f_a \left[\frac{(w/v_R)^{-5/3}}{(1+[(w/v_R)/k_0]^{8/3})^2}\right] \tag{4.1}$$

where Γ is the Gamma function ($\Gamma(5/3)$=0.902745) and v_R is the rocket velocity. $w = 2\pi f$ is the cyclic frequency measured in the reference frame of the sounding rocket.

$$C_n^2 = a^2 N_\vartheta / \varepsilon^{1/3} \tag{4.2}$$

is the structure function constant, ε is the turbulent energy dissipation rate, and N_ϑ is the variability (or inhomogeneity) dissipation rate [see *Lübken*, 1992, 1993, for more detailed explanation].

f_a is a normalization factor (we use $f_a = 2$):

$$f_a = \begin{cases} 1, & \text{e.g. } \textit{Tatarskii } [1971], \\ 2, & \text{e.g. } \textit{Lübken } [1992]; \textit{ Lübken et al. } [1993]. \end{cases} \tag{4.3}$$

The constant a^2=1.74 was obtained from laboratory experiments [see e.g. *Lübken*, 1992, 1993, 1997].

The spatial scale, l, at which the transition between the inertial and viscous energy subranges takes place, is called *inner scale*, l_0 and is related to the wave number, k_0, corresponding to this transition as:

$$l_0^H \equiv \frac{2\pi}{k_0} \tag{4.4}$$

The superscript H denotes that we use inner scale as defined in the *Heisenberg* [1948] spectral model (see section 2.2, Eq. 2.2).

Thus, to calculate the Heisenberg power spectrum from our rocket measurements, we have the following expression:

$$\mathbf{W}(2\pi \boldsymbol{f}) = \frac{\Gamma(5/3)\sin(\pi/3)}{2\pi \boldsymbol{v_R}} \; a^2 \frac{N_\vartheta}{\varepsilon^{1/3}} f_a \frac{(2\pi \boldsymbol{f}/\boldsymbol{v_R})^{-5/3}}{\left(1+\left[\left(2\pi \boldsymbol{f}/\boldsymbol{v_R}\right)/\left(2\cdot 9.90\pi\left(\boldsymbol{\nu}^3/\varepsilon\right)^{1/4}\right)\right]^{8/3}\right)^2} \tag{4.5}$$

The bold symbols denote the measured quantities. Two values ε and N_ϑ are the unknowns that characterize turbulence and are the final output of this technique. The other values included in Eq. 4.5 are the constants described above.

The kinematic viscosity ν can be calculated from measurements of neutral temperature and density as recommended by the US Standard Atmosphere [*Sissenwine et al.*, 1962]:

$$\nu = \mu/\rho, \qquad \mu = \frac{\beta T^{3/2}}{T+S} \tag{4.6}$$

where μ is the dynamic viscosity, ρ is the mass density of the air, T is temperature, $S = 110.4\ K$ is Sutherland's constant, and $\beta = 1.458 \cdot 10^{-6}\ kg/(s \cdot m \cdot K^{1/2})$ is another experimental constant.

Varying ε and N_ϑ, we get different spectra from Eq.4.5. Thus, we can fit this calculated spectrum to a measured spectrum using, e.g., least square methods [see e.g. *Numerical Recipes in C, Press et al.*, 1989]. For the complete formulary see Appendix A.

4.3 Background atmosphere: Measurement techniques

The previous section shows that for the derivation of the turbulent parameters we need to know the atmospheric temperature, T, and density, ρ, measured in the same volume. These parameters (T and ρ), however, must not include small-scale variation but must be smoothed over spatial distance of the size of largest eddy. These mean values are called the background parameters, also referred to as the *background atmosphere*.

For background temperatures and densities we use the smoothed altitude-profiles, derived either from the CONE measurements (if available, see section 4.5.1) or with the falling sphere (FS) technique (see section 4.5.3). If neither of the measurements is available, one can also use an empirical model, the Mass-Spectrometer-Incoherent-Scatter (MSIS) model [*Hedin*, 1991], or the COSPAR International Reference Atmosphere (CIRA) [*Labitzke et al.*, 1985; *Fleming et al.*, 1988; *Rycroft et al.*, 1990].

4.4 Plasma: Measurement techniques

In contrast to the neutral gas, the atmospheric plasma can interact with electromagnetic radiation, which allows investigation of its characteristics also remotely: i.e., using radars.

The in situ measurements of plasma parameters can often be done with high altitude resolution covering small-scale plasma structuring. The plasma parameters that are usually measured in situ include electron and ion density, electric field fluctuations, and ion and electron temperature.

These measurements utilize such techniques as fixed biased (electrostatic) and swept Langmuir probes, radio wave propagation experiments, E-field probes, and Faraday cups. Some of these techniques are briefly described in section 4.5.3.

4.5 Description of the rocket instruments

There are some obvious requirements for the instruments operating onboard the sounding rockets. One is that the time constant of the instrument must be small enough to allow a good altitude resolution. Usually, a sounding rocket passes through the mesosphere with a velocity of about 1000 m/s. This means that we need a time resolution of 1 ms in order to measure with 1 m altitude resolution.

In the presented work two instruments are used to sound small-scale structures in the middle atmosphere. These are the CONE (COmbined sensor for Neutral and Electrons) and the PIP (Positive Ion Probe), which are described in more detail in the following subsections (sections 4.5.1 and 4.5.2 respectively).

These two sensors are usually mounted either in the front or the rear of the payload so that they look along the rocket velocity vector.

A number of accompanying experiments are also employed in the presented work. In the following subsections those experiments that are relevant to this study are briefly described.

4.5.1 CONE instrument

The CONE is a combination of an ionization gauge and a fixed biased Langmuir probe. A schematic of the CONE instrument is shown in Fig. 4.2. This instrument was developed in the atmospheric physics laboratory of Bonn University, which then moved to the Leibniz-Institute of Atmospheric Physics. The CONE was successfully used in more than 30 sounding rocket flights. The basic reference to the technical description of the CONE instrument is *Giebeler et al.* [1993].

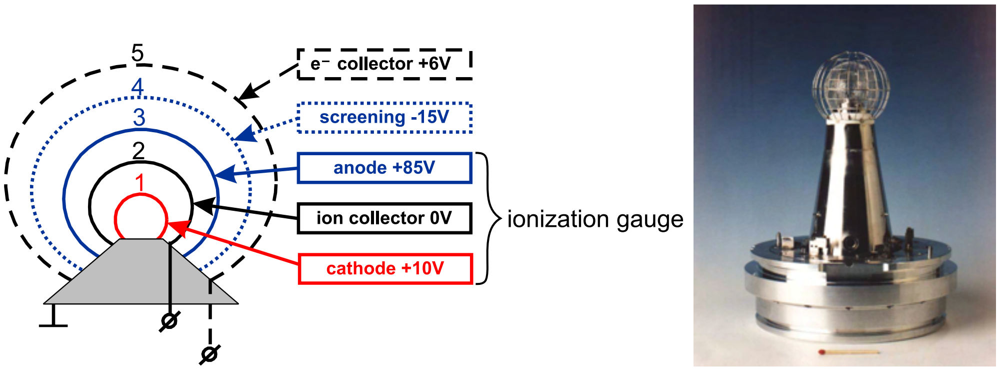

Figure 4.2: Schematic and photo of the CONE instrument.

Briefly, this instrument functions as follows. The outermost grid of the CONE instrument (it is marked by the number 5 in Fig. 4.2) is positively biased: therefore, it attracts negatively charged atmospheric constituents. Obviously, this grid also works as a shield for positive ions. The next grid (number 4 in Fig. 4.2) is negatively biased, and hence, it shields the ionization gauge against the rest of the ambient plasma. The innermost cathode, collecting electrode, and anode (numbers 1, 2, and 3 in Fig. 4.2, respectively) form the ionization gauge itself.

The outermost grid of CONE (electron collector) and the inner grid of the ionization gauge (ion collector) are connected to sensitive electrometers. Thus, the currents measured by them are proportional to the number of the collected elements: i.e., to the local electron and neutral number density, respectively.

The time constant of both the electron and neutral density measurements is less than 1 ms. For a typical rocket flight this implies an altitude resolution of tens of centimeters. The precision of the measurements with the CONE instrument is better than 0.1 %.

The high precision and small time constant of the CONE instrument make it possible to detect small-scale density fluctuations in both species (neutrals and electrons) that arise due to processes like neutral air turbulence [*Lübken et al.*, 2002] or plasma instabilities [e.g. *Blix et al.*, 1994].

Making use of an absolute laboratory calibration for the CONE instrument allows to derive an absolute neutral air density altitude-profile [*Lübken*, 1993; *Rapp et al.*, 2001]. Also, because of the disturbed density filed due to the shock front, for the absolute density derivation aerodynamical calculations must be used to correct the measurements [*Rapp et al.*, 2001]. This, however, does not affect the measurements of the small-scale density fluctuations, which are used in the turbulence detection technique. In addition, the height profile of neutral number densities can be integrated assuming hydrostatic equilibrium to yield a temperature profile at $\sim$200 m altitude resolution and an accuracy of $\sim$3 K [*Rapp et al.*, 2001, 2002].

4.5.2 PIP instrument

The PIP instrument was developed by the Norwegian Defence Research Establishment (FFI). The PIP is an electrostatic (or fixed biased Langmuir) probe. The time constant of this instrument is also less than 1 ms, making it possible to detect ion irregularities on a spatial scale as small as ten centimeters. The precision of the measurements with the PIP instrument is better than 0.1 %. Together with the radio wave propagation experiment, the PIP sensor further allows us to derive absolute ion densities. For a detailed description of the PIP instrument, the reader is referred to *Blix et al.* [1990a]. The PIP is shown schematically in Fig. 4.3. The outermost grid is under the rocket body potential. The inner grid is negatively biased: therefore, it collects positive ions.

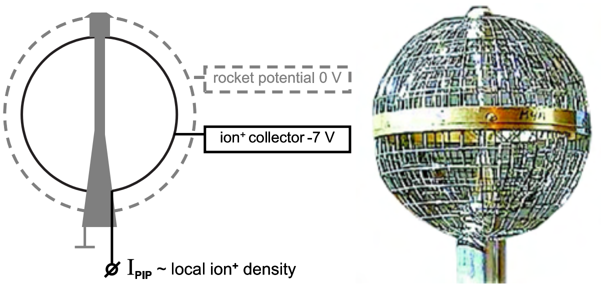

Figure 4.3: Schematic and photo of the PIP instrument.

The high precision and small time constant of the PIP instrument allow to detect small-scale plasma density fluctuations that arise due to processes like plasma instabilities [e.g. *Blix et al.*, 1994].

The PIP instrument was also used to study neutral air turbulence [e.g. *Thrane and Grandal*, 1981; *Thrane et al.*, 1987; *Blix et al.*, 1990a, b; *Blix and Thrane*, 1991], since positive ions can conditionally be used as a tracer for turbulence (see above).

4.5.3 Other instruments

Radio Wave Propagation Experiment

The radio wave propagation experiment yields a high-precision electron density measurement. Basically, this is realized by transmitting a radio signal from the ground and receiving it by a pair of antennas on the rocket. The theoretical basis and practical application of this technique are described, for example, in *Bennett et al.* [1972] and *Smith* [1986]. The transmitted linearly polarized electromagnetic wave may be considered the resultant of two circularly polarized waves with equal electric field vectors rotating in opposite directions. When propagating through the ionospheric plasma, these two waves differ in absorption and phase velocity. The difference in absorbtion causes the resultant wave to become elliptically polarized (differential absorption). In addition, the difference in phase velocity causes the major axis of the polarization ellipse to rotate as the wave propagates (Faraday rotation). Since both differential absorption and Faraday rotation directly depend on the electron number density along the path of the radio signal through the ionosphere, the height-resolved measurements of both quantities can be used to precisely derive the electron number density profile at a typical vertical resolution of ~1 km (defined by the rocket velocity and the rocket spin rate). Importantly, these measurements are not influenced by unwanted effects due to the interaction of the payload with the ambient plasma like, e.g., payload charging.

The combination of this technique with high-resolution measurements of positive ion densities with the PIP and electron densities with the CONE instrument yields the fine-scale absolute ion and electron density profiles.

Cold Plasma Probe

The Cold Plasma Probe (CPP) usually mounted on the front side of the payload is a swept Langmuir probe. A description of the operation principle of such probes can be found, for example, in *Thrane* [1986]; *Laframboise and Sonmor* [1993]. For a detailed description of the CPP instrument and its operation see *Thrane* [1986]; *Blix et al.* [2004]; *Svenes et al.* [2005].

Briefly, the CPP consists of the spherical electrode surrounded by a spherical grid. The idea is to apply a retarding potential to the outer grid and measure the current on the inner electrode. All the retarded particles (electrons or ions) with a kinetic energy greater than the applied potential will be collected. Changing the applied potential we can derive an energy spectrum of the collected elements (electrons or ions). From the analysis of these spectra, the plasma parameters can be determined. Most important for our application, this technique allows us to derive the electron temperature.

The resolution of this technique is limited by the time of at least one scan (the change of the retarding potential). For a typical rocket flight the altitude resolution of CPP is ~1 km.

Falling spheres

The falling sphere (FS) technique is based on the following concept. A small rocket delivers an inflatable sphere to heights of ~90-120 km. The sphere is inflated at the apogee and falls down. It experiences horizontal advection by the neutral winds and deceleration by friction with neutral gas. The sphere is precisely tracked by a ground-based radar. From the first derivative of the trajectory one can derive neutral winds. From the second derivative (i.e., deceleration), one can derive the neutral air density. A more detailed description can be found e.g. in *Meyer* [1988]; *Schmidlin* [1991]; *Schmidlin et al.* [1991]; *Müllemann* [2004].

Chapter 5

Analysis technique: Turbulence

In this chapter a detailed description of the "standard" analysis technique based on the Fourier spectral analysis is given (section 5.2). Section 5.3 introduces a new turbulence analysis technique based on the wavelet spectral analysis instead of the Fourier spectral analysis method. This technique is described in detail. Then in Chapter 5.4 the advantages are demonstrated, and new results emerging from the improved analysis method are presented.

5.1 Data reduction

As described above, the primary steps of our turbulence detection technique are the following. Applying electrostatic probes [e.g. *Blix et al.*, 1990a] or ionization gauges [e.g. *Giebeler et al.*, 1993], we measure current $I(t)$ as a function of flight time t at altitudes between ~70 and ~110 km (Fig. 5.1, left panel). As shown in, e.g., *Lübken* [1993], $I(t)$ is directly proportional to atmospheric number density $n(t)$. This current is then converted to the relative density fluctuations, also called residuals, $r(t)$, which are determined as:

$$r(t) \equiv \frac{\Delta n}{< n >}(t) = \frac{n(t) - n_{ref}(t)}{n_{ref}(t)} = \frac{I(t) - I_{ref}(t)}{I_{ref}(t)} \tag{5.1}$$

where the reference current $I_{ref}(t)$ can be derived either by a polynomial fit to the measured current $I(t)$ [e.g. *Lübken*, 1992] or as a running average of the measured time series $I(t)$ [e.g. *Blix et al.*, 1990a]. This conversion procedure is demonstrated in Fig. 5.1.

The resultant residual fluctuations (shown in the right panel of Fig. 5.1) are then used as a tracer for turbulence. We use the spectral model method [see e.g. *Lübken*, 1992, 1993, 1997; *Lübken et al.*, 1993] to characterize detected fluctuations. Specifically, we fit a theoretical model to the power spectra of the measured fluctuations. The standard and well developed tool to examine the spectral content of a measured time series is the Fourier analysis. We use this tool in our standard technique, as described in section 5.2. There is, however, another relatively new spectral analysis tool−wavelet analysis, which we use in the improved version of our technique. This part of the analysis algorithm is introduced in section 5.3.

5.2 Standard methodology: Fourier technique

Our standard technique to analyze neutral air density fluctuations with respect to turbulence has been described in detail in *Lübken* [1992, 1993]; *Lübken et al.* [1993]; *Lübken* [1997].

Here we summarize the primary steps and the complete formulary is presented in Appendix A.

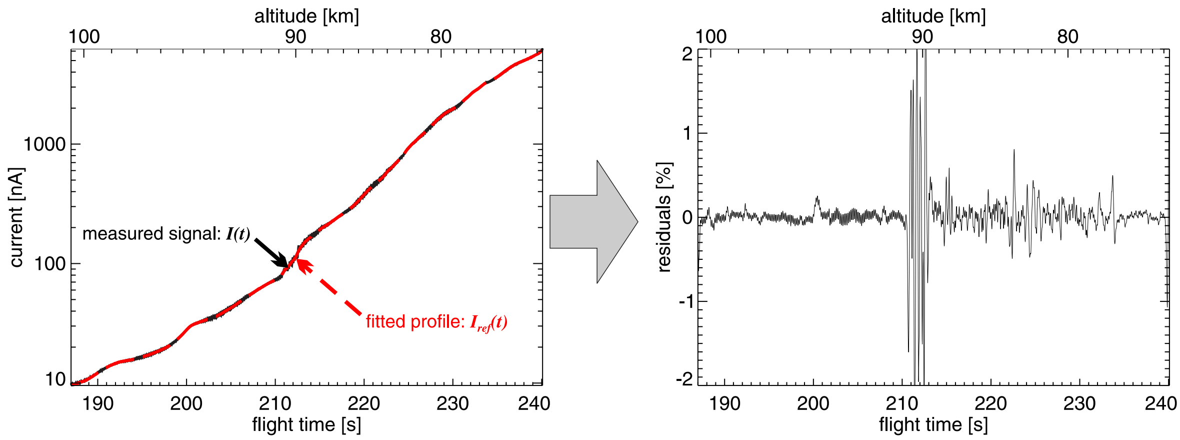

Figure 5.1: Left panel: Measured current (black profile) as a dependence of the rocket flight time (lower axis) or altitude (upper axis). The red solid line is the fitted reference current I_{ref}, used in Eq. 5.1 for the conversion to the residuals. Right panel: Residuals $r(t)$ resulting from the current conversion (Eq. 5.1).

Using rocket trajectory, the measured currents (Fig. 5.1, $I(t)$ in the left panel) are subdivided into altitude bins, typically of 1−5 km extent. Then we derive the residuals, $r(t)$, for each altitude bin using Eq. 5.1. Two examples of such a bins are shown in Fig. 5.2.

We then calculate the Fourier power spectrum of the derived residuals, $r(t)$, applying the Hanning-windowed Fast Fourier Transform (FFT). The power spectrum is normalized to yield the variance, σ, of the observed relative fluctuations:

$$\int_{-\infty}^{\infty} W(w)dw = \sigma^2 \tag{5.2}$$

Subsequently, the power spectrum of each bin is fitted by a spectral turbulence model [e.g. *Heisenberg*, 1948], where the main free fitting parameter is the turbulent energy dissipation rate, ε (see section 4.2, Eq. 4.5).

Fig. 5.3 presents the Fourier power spectra derived for the altitude bins shown in Fig. 5.2. The lower axis shows the frequency, f, measured in the rocket domain. The upper axis represents the spatial scales, l, derived as:

$$l = v_R/f \tag{5.3}$$

where v_R is the rocket velocity. l is the length scale of the mesospheric structures as observed from the ground. Representing the spectra as a dependence of the spatial scales is necessary to enable comparison of different measurements conducted at different rocket velocities and different time resolutions of the instruments. It is also more natural to think of the turbulent structures in terms of the sizes of the eddies in the physical space.

The left panel of Fig. 5.3 represents the Fourier power spectrum (solid line) of the residuals shown in the left panel of Fig. 5.2 and the fitting results. The dashed line is the model spectrum [*Heisenberg*, 1948] fitted to the measured spectrum. The vertical dash-dotted line marks the derived inner scale of turbulence, l_0^H. The dash-dot-dotted line shows an estimate of the outer (buoyancy) scale, L_B (see section 2.1, Eq. 2.3).

The right panel of Fig. 5.3 represents the Fourier power spectrum (solid line) of the residuals shown in the right panel of Fig. 5.2. The fitting process did not converge in this case. It is also

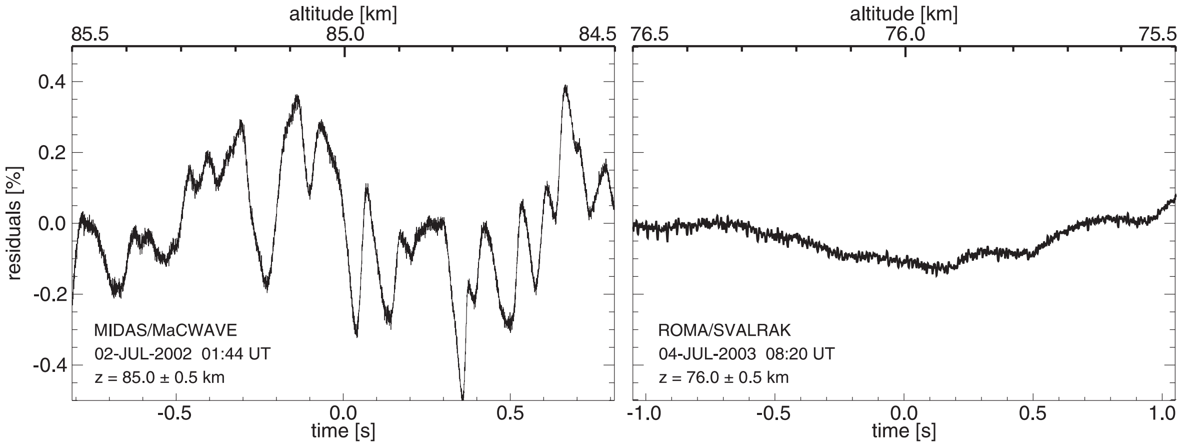

Figure 5.2: An example of the residuals taken from a 1 km altitude bins. Left panel: flight MM-MI-12, 2-JUL-2002. Right panel: flight RO-MI-02, 4-JUL-2003.

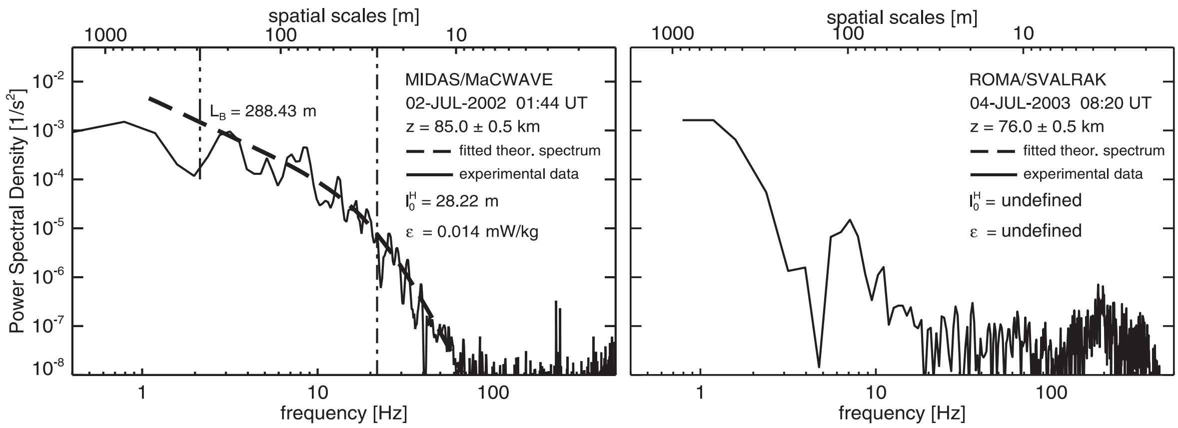

Figure 5.3: Power spectral density (black solid line) of the residuals measured during the flight MM-MI-12 (left panel) and RO-MI-02 (right panel). The dashed line on the left panel shows the best fit of the model of *Heisenberg* [1948].

seen that the spectral shape in the right panel of Fig. 5.3 is far from that of the Kolmogorov's type (compare with Fig. 2.1). This implies that no turbulence was detected at these altitudes.

The final result of our standard technique is an ε-profile with a typical altitude resolution of 1-5 km (e.g. Fig. 5.4).

5.3 Improved approach: Wavelet technique

Our new turbulence analysis technique using wavelet analysis was first described in *Strelnikov et al.* [2003]. Here we expound this issue with some more details.

The wavelet analysis is a relatively new and still developing spectral analysis tool. In contrast to the Fourier analysis, which decomposes time series into a sum of the infinite in-time harmonic functions, namely sine and cosine, the wavelet analysis decomposes the signal into the time-frequency domain, also referred to as the phase space [e.g. *Holschneider*, 1993]. That is, it allows the detection of the time intervals where detected frequencies appear in the

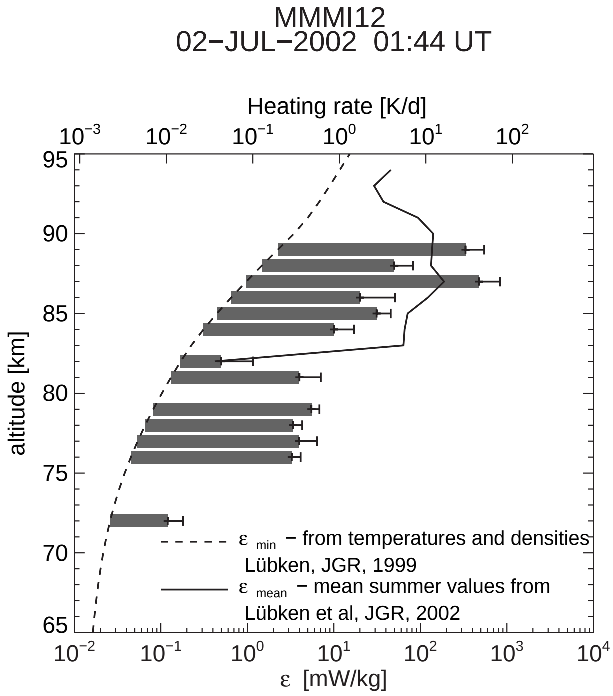

Figure 5.4: The typical result of the standard turbulence analysis technique. Turbulent energy dissipation rate, ε altitude-profile with the 1 km altitude resolution. Flight: MM-MI-12, 2-JUL-2002, Andøya Rocket Range, 69 °N, 15 °E.

time series. For the description of the basic principles, mathematical details, and different applications of the wavelet analysis the reader is referred to the numerous and continuously appearing publications and Web resources. Some of them are cited in the next sections.

5.3.1 Wavelet analysis: Definitions

The wavelet transform of a time series $x(t)$ is defined as [e.g. *Daubechies*, 1992; *Kumar and Foufoula-Georgiou*, 1997]:

$$(\mathbb{W}x)(\tau, s) = \int x(t)\ \psi^*_{\tau,s}(t)\ dt \tag{5.4}$$

The function ψ is called *"mother wavelet"* (equally *"wavelet function"*) and * indicates the complex conjugate. Each function from the family

$$\psi_{\tau,s}(t) = \frac{1}{\sqrt{s}}\psi\left(- \frac{t-\tau}{s}\right) \tag{5.5}$$

is called *"daughter wavelet,"* where τ and s are parameters.

To be a wavelet, a function $\psi(t)$ must be well localized in both time and frequency space [e.g. *Daubechies*, 1992; *Lewalle*, 1995; *Farge et al.*, 1999]: That is, it must have a finite energy and zero mean. The latter condition is also known as admissibility condition:

$$\int_{-\infty}^{\infty} \psi(t)dt = 0 \tag{5.6}$$

There are many different wavelet functions, but generally they can be divided into orthogonal and nonorthogonal [e.g. *Daubechies*, 1992; *Lewalle*, 1995; *Torrence and Compo*, 1998].

There are two sorts of the wavelet transform: continuous and discrete [e.g. *Daubechies*, 1992; *Lewalle*, 1995; *Torrence and Compo*, 1998]. In the continuous case parameters s and τ can change continuously. In the discrete wavelet transform s and τ can only take on discrete values. Each wavelet function is only applicable either for the continuous (nonorthogonal) or discrete (orthogonal) analysis algorithm. One can also try to construct a new wavelet that can be more suitable for the particular problem [e.g. *Sweldens and Schröder*, 1996].

We further consider only the *Morlet* wavelet function, which is defined as [*Grossmann and Morlet*, 1984]

$$\psi(\eta) = \sqrt[4]{\frac{1}{\pi}} exp\Bigg(i\omega_0\eta\Bigg) exp\Bigg(-\frac{\eta^2}{2}\Bigg), \qquad \eta = \frac{t-\tau}{s} \tag{5.7}$$

where ω_0 is a non-dimensional frequency parameter of the wavelet function and η is a non-dimensional time parameter. The Morlet wavelet is a nonorthogonal complex-valued function and. Therefore, we only consider the continuous wavelet transform here.

The Morlet wavelet consists of a plane wave modulated by a Gaussian envelope of width ω_0/π [*Lewalle et al.*, 2005]. The envelope factor ω_0 controls the number of oscillations of the wavelet (the higher ω_0-value, the more oscillations). Fig. 5.5 shows an example of two Morlet wavelets with $\omega_0 = 6$ (left panel) and $\omega_0 = 12$ (right panel), and η is arbitrary but the same for both cases. The upper panel shows these functions in the time space: The solid line displays the real part, and the dashed line displays the imaginary part. The lower panel shows the same functions in the frequency space.

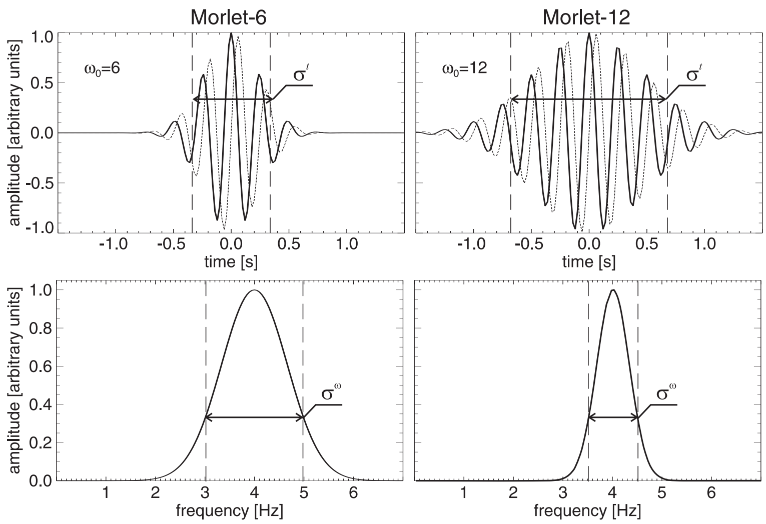

Figure 5.5: Upper panel: Real (solid line) and imaginary part (dashed line) of a Morlet wavelet in the time space with ω_0=6 (left) and ω_0=12 (right). Lower panel: The same wavelet functions in the Fourier space. Dashed lines mark the width of the function, which is denoted by σ^t and σ^ω for the time and frequency space, respectively.

One sees that the higher order Morlet function (larger ω_0-value) has larger time and smaller frequency support (or the widths σ^t and σ^ω). This is the direct consequence of Heisenberg's uncertainty principle, which can be written as:

$$\sigma^t\sigma^\omega = \sigma^t\ 2\pi\sigma^f \geq \frac{1}{2} \tag{5.8}$$

where σ^t and σ^ω are the width of the wavelet function in time (time support) and frequency space (frequency support), respectively. We discuss these values later in this section.

Changing parameter τ of a wavelet function $\psi_{\tau,s}$, one changes the time localization of the wavelet:

$$\psi_{\tau,s}(t)\Bigg|_{s=const} = \frac{1}{\sqrt{s}}\psi\left(-\frac{t-\tau}{s}\right), \qquad \tau = \tau_1, \tau_2, ... \tag{5.9}$$

This operation is called *translation* of the mother wavelet. Each function $\psi_{\tau,s}(t)$ is localized around the time point $t = \tau$. Changing parameter τ, one shifts the localization point of the function $\psi_{\tau,s}(t)$ along the time axis t (translates). The translation of the Morlet-12 wavelet is demonstrated in Fig. 5.6, where the upper panel shows the signal to be analyzed in the time space. The lower panels show two translated versions of the wavelet function in the same (as for the signal) time domain. The wavelet function must have the same number of points as the investigated signal, but its energy is concentrated around the time point $t = \tau$.

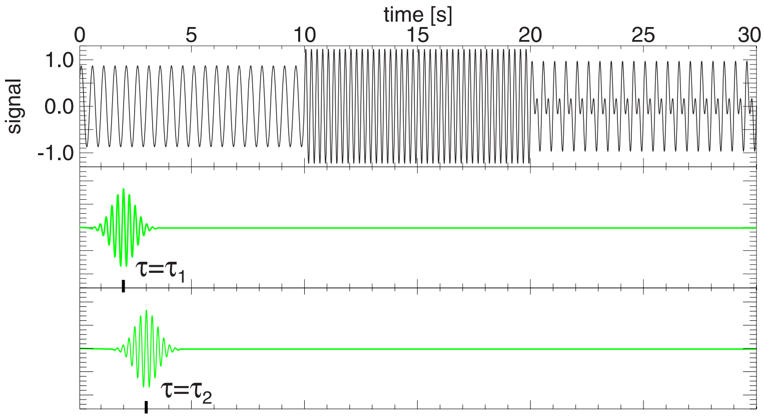

Figure 5.6: Translation of the wavelet function. The upper panel shows the signal to be analyzed. The lower panels show two translated Morlet-12 wavelet functions at a fixed scale.

Changing parameter s, also called *wavelet scale*, one changes the frequency of the function:

$$\psi_{\tau,s}(t)\Bigg|_{\tau=const} = \frac{1}{\sqrt{s}}\psi\left(-\frac{t-\tau}{s}\right), \qquad s = s_1, s_2, ... \tag{5.10}$$

This operation is called *scaling* of the mother wavelet. Large values of the scaling parameter s correspond to the low frequencies or the large scales of the function $\psi_{\tau,s}$. Small s-values correspond to the high frequencies or the small scales of $\psi_{\tau,s}$. Fig. 5.7 demonstrates the scaling of the Morlet wavelet function. The left panels in Fig. 5.7 show the Morlet-12 wavelet (ω_0=12) at the scale s_1, which corresponds to the frequency of 4 Hz. The right panels in Fig. 5.7 show the same Morlet-12 wavelet but at the scale $s_2 > s_1$, which corresponds to the frequency of 2 Hz.

Simply speaking, the wavelet transform correlates the signal with the wavelet function in the following sequence:

1. Moving the wavelet of a fixed scale (frequency) along the time axis (translation) find the time regions where the correlation is high.

2. Change the scale (frequency) of the wavelet function (scaling).

3. Repeat the steps 1 and 2 until we fill up the scale (frequency) range we are interested in.

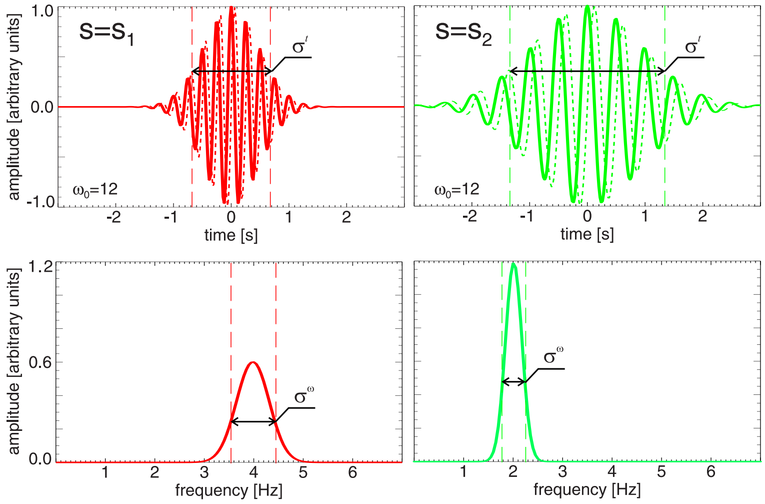

Figure 5.7: Scaling of the wavelet function. Upper plots show the Morlet-12 wavelet function (complex valued) in the time domain. The solid line is the real part, and the dashed line is the imaginary part. The lower plots show the same functions in the Fourier domain. Left panel: The scale of the Morlet function corresponds to the frequency of 4 Hz. Right panel: The scale of the Morlet function corresponds to the frequency of 2 Hz. The larger scales correspond to the lower frequency.

5.3.2 Wavelet analysis: Properties

Auto adjustable

A specific and valuable feature of the wavelet functions (seen, e.g., from Fig. 5.7) is that their width in the time space changes with frequency. High-frequency wavelet functions are narrow in the time space; conversely, low-frequency wavelets are broad in the time space. This allows the investigation of a quickly changing high-frequency content of a signal.

Reversibility

One can also reconstruct the signal using the formula (resolution of identity) [*Daubechies*, 1992; *Kumar and Foufoula-Georgiou*, 1997; *Torrence and Compo*, 1998]

$$x(t) = \frac{1}{C_\psi} \int_0^\infty \int_{-\infty}^\infty \frac{1}{\sqrt{s}} \psi\left(- \frac{t-\tau}{s} \right) \left(\mathbb{W}f(\tau, s) \right) d\tau \frac{ds}{s^2} \tag{5.11}$$

Coefficient C_ψ depends only upon the wavelet function ψ and is defined as:

$$C_\psi = \int_{-\infty}^\infty \frac{\left| \widehat{\psi}(\zeta) \right|^2}{\zeta} d\zeta \tag{5.12}$$

where $\widehat{\psi}$ is the Fourier transform of ψ.

Amplitude and Phase

After applying the wavelet transform to the time series $x(t)$, we get a two-dimensional matrix of wavelet coefficients, which constitute the wavelet transform, $\mathbb{W}x(t, s)$, of $x(t)$. One dimension of that matrix reflects the time, and another dimension reflects the scale (frequency) dependence of the transform. The value of the wavelet coefficient describes the wavelet transform $\mathbb{W}x$ at a certain point in the phase (time-frequency) space.

Because the wavelet function ψ is generally complex, the wavelet transform $\mathbb{W}x$ is also complex. The transform can then be divided into the real part, $Re(\mathbb{W}x)$, and imaginary part, $Im(\mathbb{W}x)$, or amplitude, $|\mathbb{W}x|$, and phase, $\tan^{-1}[Re(\mathbb{W}x)/Im(\mathbb{W}x)]$.

Power spectrum

The wavelet transform is an energy-preserving transformation: That is, integrals are equal [e.g. *Lewalle*, 1995; *Perrier et al.*, 1995; *Kumar and Foufoula-Georgiou*, 1997]:

$$\int_{-\infty}^{\infty} \Big|x(t)\Big|^2 dt = \frac{1}{C_\psi} \int_{-\infty}^{\infty} \int_{0}^{\infty} \Big|\mathbb{W}x(s,t)\Big|^2 s^{-2} ds dt \tag{5.13}$$

where the left part gives the full energy in the signal and the right side term gives full energy in the energy distribution, which results from the wavelet transform $\mathbb{W}x$. The expression under the integral can be interpreted as energy density. Eq. 5.13 is the analogy to Parseval's theorem for the Fourier analysis [see e.g. *Jenkins and Watts*, 1969]. Similarly to the Fourier analysis, one can also define the *wavelet energy spectrum* as:

$$E(s,t) = K_{norm} \Big|\mathbb{W}x\Big|^2 \tag{5.14}$$

where the normalization constant K_{norm} is discussed later. The function $\Big|\mathbb{W}x\Big|^2$ is also referred to as *scalogram* [e.g. *Kumar and Foufoula-Georgiou*, 1997] or *power spectrum* [e.g. *Torrence and Compo*, 1998].

Normalization

The wavelet function $\psi_{\tau,s}(t)$ at each scale (frequency) is normalized to have unit energy. This ensures that the wavelet transforms $\mathbb{W}x$ for each scale (frequency) are comparable to each other.

The normalization for the power spectrum (Eq. 5.14), proposed by *Torrence and Compo* [1998] to make it easier to compare different wavelet power spectra, is the same as we use for the normalization of the Fourier power spectra in our standard technique (section 5.2):

$$\Big|\mathbb{W}x\Big|^2 = \sigma^2 \tag{5.15}$$

where σ is the variance of the time series. This allows us to compare both techniques.

Cone of influence

Because most time series are finite in time and are not cyclic signals, they have a singularity at the edges. Therefore, the wavelet transform $\mathbb{W}x$ will be influenced by an edge effect. That is, the result of the wavelet transform will not reflect the "true" energy content of the signal around the edges. The region where this uncertainty takes place is called *cone of influence* (COI). It is defined by the width of the wavelet function in the time space. The width of the wavelet function, however, is different for each function and it is often not obvious what to consider the width of the wavelet to be. Following *Torrence and Compo* [1998], we define the width of a wavelet function (in the time or frequency space) as an interval where the amplitude of the function decreases e-times ($e - folding\ time,\ \tau_e$) and where e is the base of the natural logarithm. The width of the wavelet function in time ($\sigma^t = \tau_e$) and frequency ($\sigma^\omega = \tau_e$) space is shown in Fig. 5.5 and 5.7 by the vertical dashed lines.

One can choose any other criteria, however, for the width of the wavelet function: for example, *Jordan et al.* [1997] using a formula proposed for the Morlet wavelet:

$$\sigma_0^\omega = \sqrt{2\ ln(\chi)} \tag{5.16}$$

where $0.0 < \chi < 1.0$ describes the part of the wavelet function where amplitude (in the Fourier space) decreases χ-times. Thus, taking $\chi = 1/e = 0.37$ we get the e-folding time, $\sigma^\omega = \tau_e$. Value χ near 0.0 describes most of the energy localization (results in a larger σ^ω-value), whereas χ near 1.0 describes the vicinity of the wavelet maxima ($\chi \to 1 \Rightarrow \sigma^\omega \to 0$).

Resolution

The width of the wavelet function in the time and frequency spaces at a scale s can be found as [e.g. *Kumar and Foufoula-Georgiou*, 1997; *Jordan et al.*, 1997]:

$$\sigma_s^t = \sigma_0^t \cdot s \tag{5.17}$$

$$\sigma_s^\omega = 2\pi\ \sigma_s^f = \sigma_0^\omega / s = 2\pi\ \sigma_0^f / s \tag{5.18}$$

where σ_0^t and σ_0^f are the width of the mother wavelet ($s = 0$) in the time and frequency space respectively.

The center frequency of the Morlet wavelet function (the frequency of the maxima in the frequency space) can be found as [*Kumar and Foufoula-Georgiou*, 1997]:

$$\omega_s^{max} = 2\pi f_s^{max} = \omega_0 / s \tag{5.19}$$

Again, following *Torrence and Compo* [1998] and taking the e-folding time as the width of the wavelet function ($\sigma_0^t = \tau_e, \sigma_0^\omega = 2\pi\sigma_0^f = \tau_e$), we can write:

$$\sigma_s^t = \tau_e \cdot s \tag{5.20}$$

$$\sigma_s^\omega = 2\pi\ \sigma_s^f = \tau_e / s \tag{5.21}$$

The localization properties of wavelets are discussed in further depth by *Daubechies* [1990] and *Holschneider* [1993].

The time-frequency resolution of the wavelet analysis can be considered in terms of the Heisenberg box $[\sigma^t \times \sigma^\omega]$ schematically shown in Fig. 5.8. The area of this box remains constant while scaling the wavelet function ($\sigma^t \cdot \sigma^\omega = const$).

Since we convert the time of the rocket flight to the altitude (using rocket trajectory) and frequency to the spatial scales (see section 5.2), it is also helpful to convert the time-width of the resolution box (σ^t) to the altitude resolution (σ^z) of the analysis and relate it to the spatial scales (l) of the detected structures.

Using wavelet scale (s) to frequency (f) conversion formula [*Torrence and Compo*, 1998], we can write for the frequency, measured in the rocket domain:

$$f = \frac{1}{s \cdot K_F} \tag{5.22}$$

where the conversion coefficient K_F is unique for each wavelet function, independent of the wavelet scale, and can be derived numerically [see e.g. *Farge*, 1992].

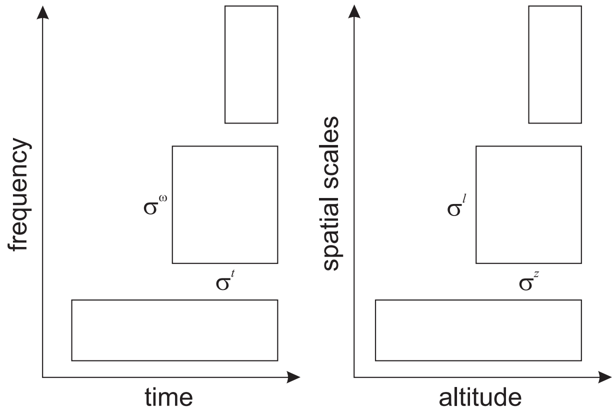

Figure 5.8: Resolution of the wavelet analysis demonstrated using the Heisenberg box. Left panel: σ^{ω} is the width of the wavelet function in frequency, and σ^{t} is the width of the wavelet function in time space (frequency and time support). Right panel: σ^{l} is the width of the wavelet function in spatial scale, and σ^{z} is the width of the wavelet function in altitude space (as converted from frequency and time, see text for details).

Combining Eq. 5.3 and Eq. 5.22, for the wavelet scale we get:

$$s = \frac{l}{v_R \cdot K_F} \tag{5.23}$$

Inserting Eq. 5.23 in Eq. 5.20, for the time resolution of the analysis at a wavelet scale s we get:

$$\sigma_s^t = \frac{l}{v_R} \cdot \frac{\tau_e}{K_F} = \frac{l}{v_R} \cdot K, \qquad K \equiv \frac{\tau_e}{K_F} \tag{5.24}$$

where the introduced constant K only depends on the choice of the wavelet function.

On the other hand, during the time $t = \sigma_s^t$, the sounding rocket passes through the spatial distance $l = \sigma_s^z$ at the velocity v_R. That is:

$$\sigma_s^t = \frac{\sigma_s^z}{v_R} \tag{5.25}$$

Finally, combining Eq. 5.24 and Eq. 5.25, we get the expression connecting the measured spatial scales (l) and the spatial resolution of the analysis (σ_s^z):

$$\sigma_s^z = l \cdot K, \qquad K \equiv \frac{\tau_e}{K_F} \tag{5.26}$$

Thus, for all the Morlet wavelet functions, $\tau_e = \sqrt{2} \approx 1.4$. The K_F-value and, therefore, K depend on the parameter ω_0:

$\omega_0 = 6 \quad \Rightarrow \quad K_F \approx 1.033, \quad K \approx 1, \quad \sigma^z \approx 1l$
$\omega_0 = 12 \quad \Rightarrow \quad K_F \approx 0.626, \quad K \approx 3, \quad \sigma^z \approx 3l$
$\omega_0 = 24 \quad \Rightarrow \quad K_F \approx 0.522, \quad K \approx 5, \quad \sigma^z \approx 5l$

That is, applying Morlet-6 wavelet analysis to the measured time series, we can resolve the change of the detected structure of length l at the rate σ^z, which is equal to the size of the structure ($\sigma^z = l$). Applying higher order Morlet ($\omega_0 > 6$) wavelet analysis we smooth out the resolution of the measurements at a certain rate.

Global wavelet spectrum

After applying the wavelet transform, the resulting matrix $\mathbb{W}x$ has dimensions $n_t \times n_s$, where n_t is the number of points in the time series and n_s is the number of scales (frequency points). One can average the wavelet transform matrix $\mathbb{W}x$ over the n_t-dimension and thereby derive the *global* wavelet spectrum. The global wavelet spectrum is a one-dimensional (like the Fourier spectrum) power spectrum that corresponds to the smoothed (over the frequency axis) version of the Fourier power spectrum [e.g. *Holschneider*, 1993; *Perrier et al.*, 1995; *Jordan et al.*, 1997; *Kumar and Foufoula-Georgiou*, 1997]. The global wavelet spectrum can, therefore, be used instead of the Fourier power spectrum if one-dimensional representation is needed.

Comparison with the Fourier spectrum

For a detailed comparison and proper mathematical treatment of a different aspects of the Fourier and wavelet analyses, the reader is referred e.g., to *Perrier et al.* [1995]. Here we consider the difference in the resolution of these techniques.

The frequency resolution of the Fourier analysis is constant for a given time series [*Jenkins and Watts*, 1969]:

$$\sigma_F^f = \frac{1}{N\Delta t} = \frac{1}{N} f \tag{5.27}$$

where N is the number of points in time series and Δt is the time sampling interval.

The frequency resolution of the Morlet wavelet analysis depends on the sampling frequency (f) and wavelet function:

$$\sigma_W^f = \frac{\tau_e}{s} = f \cdot \tau_e K_F \tag{5.28}$$

where τ_e and K_F are the characteristics of the wavelet function. The higher the wavelet order (larger ω_0), the smaller the K_F-value and, therefore the smaller the frequency resolution window σ_W^f (i.e. better resolution). Eq. 5.28 explicitly shows that the frequency resolution of the wavelet analysis decreases (σ_W^f grows) with increasing frequency.

The time resolution of the Fourier analysis is defined by the length of the time series. That is, the Fourier analysis itself can deal only with the entire time series: however, we can split the data into subsets and thereby achieve some coarse time resolution. That is exactly what we do in our standard turbulence analysis technique (section 5.2), dividing the ~40 km data set into 1 km subsets and analyzing them separately, thereby achieving altitude resolution of 1 km. This "resolution" is constant for all the scales, however, from centimeters to one kilometer.

The time resolution of the wavelet analysis (σ_W^t) is in turn inversely proportional to the frequency resolution ($\sigma_W^t \propto 1/\sigma_W^f$). It is, therefore, high (small σ_W^t-values) for high frequencies and decreases (σ_W^t grows) with the frequency:

$$\sigma_W^t = \frac{1}{f} \cdot \frac{\tau_e}{K_F} \tag{5.29}$$

Thus, for all the Morlet wavelet functions, $\tau_e = \sqrt{2} \approx 1.4$. The K_F-value and, therefore, $K_F \cdot \tau_e$ depend on the parameter ω_0:

$\omega_0 = 6 \quad \Rightarrow \quad K_F \approx 1.033, \quad K_F \cdot \tau_e \approx 1.5, \quad \sigma^f \approx 1.5f$
$\omega_0 = 12 \quad \Rightarrow \quad K_F \approx 0.626, \quad K_F \cdot \tau_e \approx 0.9, \quad \sigma^f \approx 1f$
$\omega_0 = 24 \quad \Rightarrow \quad K_F \approx 0.522, \quad K_F \cdot \tau_e \approx 0.7, \quad \sigma^f \approx 0.7f$

The similarity between the Fourier and wavelet analyses is that they both decompose the time series into the set of self-similar basis-functions. In the Fourier analysis these functions are the sine and cosine, and in the wavelet analysis they are the wavelet functions. This means that to get a more precise (more close to the true) spectral content of the time series, one has to find such basis functions, the form of which would resemble the one contained in the investigated signal. That in turn also means that the Morlet wavelet analysis should give us results quite similar to those of the Fourier analysis, since Morlet wavelet consists of a similar basis (plane waves).

The windowed Fourier transform (WFT) also yields a time-resolved power spectra. It has, however, a fixed time resolution defined by the width of the window [e.g. *Jenkins and Watts*, 1969]. This also implies that the number of oscillations beneath the window decreases with the frequency decrease. This limits the frequency resolution of the WFT [e.g. *Perrier et al.*, 1995]. In contrast, the wavelet basis conserves the number of oscillations with changing frequency.

In summary, among the other advantages of the wavelet technique, the most important is the frequency-dependent time resolution of the analysis. Applied to the turbulence analysis, it means that in time the wavelet analysis resolves the small scales (high frequencies, see Eq. 5.3) better than the large scales.

5.3.3 Wavelet analysis: Example

We demonstrate the continuous wavelet analysis technique on an artificially constructed time series $x(t)$ using Morlet-12 (ω_0=12) wavelet.

We synthesize the time series $x(t)$ as follows. During the first ten seconds the only frequency of 2 Hz is presented in the signal. From ten to twenty seconds the only frequency of 4 Hz is presented in the signal. During the last ten seconds we introduce both those frequencies (2 and 4 Hz) simultaneously (Fig. 5.6, 5.9, upper panels).

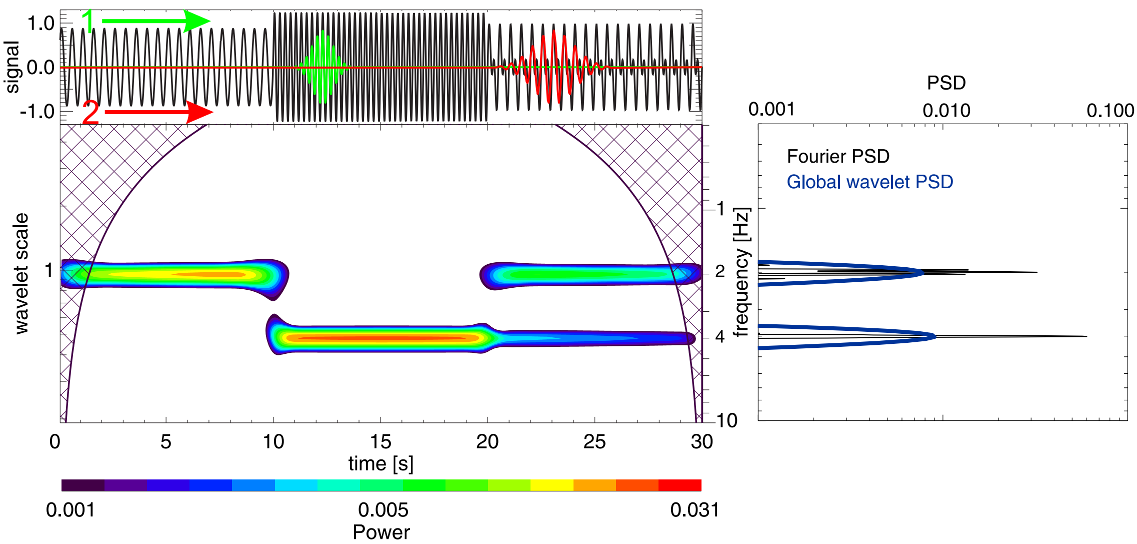

Figure 5.9: Upper panel: Synthetically constructed time series (in black) and two differently scaled wavelet functions (in color). Lower left panel: Wavelet power spectrum of the time series ($\left|\mathbb{W}x\right|^2$). Lower right panel: Global wavelet spectrum and Fourier spectrum of the time series.

Then we construct the Morlet wavelet (in the time space) as follows. The number of points must be equal to the number of points in the time series. Let us take the scale $s = s1$ such that the corresponding frequency will be equal to, e.g., 4 Hz. We take the translation time τ=0 and find how much $x(t)$ is similar to the constructed Morlet-12 function $\psi_{\tau=0,s1}$. Then we translate the Morlet-12 function ($\tau = d\tau, 2d\tau, 3d\tau, ...$), and subsequently for each translation time τ we find how much $x(t)$ is similar to the constructed Morlet-12 function $\psi_{\tau,s1}$. Strong similarity will be reflected in a high wavelet transform value, $\mathbb{W}x$, and conversely, no similarity will result in a small $\mathbb{W}x$-value. Thus, the number of operations will be equal to the number of the translation times τ. The time step $d\tau$ can be taken as equal to the time sampling interval dt of the time series $x(t)$. This first part of the analysis is schematically shown in the upper panel of Fig. 5.9 by the green wavelet (constructed for the $s = s1 \sim f = 4\ Hz$) and green arrow, showing the direction in which we "shift" the wavelet function during the translation.

In other words, we find the convolution of the time series $x(t)$ and the translated version of the constructed wavelet function $\psi_{\tau,s1}$. The convolution of two functions x and ψ is defined as:

$$(x * \psi) = \int x(t)\psi(\tau - t)dt \tag{5.30}$$

Then we scale the mother wavelet: We take the scale $s_2 \geq s_1$, which corresponds to the frequency of, e.g., 2 Hz and again find the convolution of the time series $x(t)$ and the translated version of the constructed wavelet function $\psi_{\tau,s2}$. This second part (translation of ψ at the fixed scale s_2) is schematically shown in the upper panel of Fig. 5.9 by the red wavelet and arrow.

The set of the scales (frequencies) or the scale (frequency) step can be arbitrarily chosen and not necessarily evenly spaced, although it can be optimized for any particular problem.

The lower left panel in Fig. 5.9 shows the resultant wavelet power spectrum (scalogram) of the test signal. High power appears at the frequencies and only during the time consistent with how $x(t)$ was constructed.

The right panel of Fig. 5.9 shows the global wavelet spectrum (bold blue line): that is, the local wavelet spectra (shown in color in the left panel of Fig. 5.9) averaged over the entire time interval. We show also the Fourier power spectrum of the same time series as a black profile in the right panel of Fig. 5.9. One sees that both the Fourier and global wavelet spectra show two maxima at the frequencies 2 and 4 Hz (as introduced by construction). One can also see that the difference of the amplitude of the peak maxima is larger for the Fourier spectrum than for the global wavelet spectrum. Also, the absolute value of the amplitude of the maxima is larger for the Fourier spectrum. The width of the global wavelet spectrum is larger, which results from the difference in the resolution of these methods (see above). Due to the width of the wavelet filter in Fourier space at high frequencies (small wavelet scales), the wavelet function gets broader in frequency: therefore, peaks in the spectrum get smoothed out. At low frequencies (large wavelet scales) the wavelet is narrower in frequency: therefore, the peaks are sharper and have a larger amplitude.

5.4 Improved analysis technique: New benefits

5.4.1 Wavelet PSD - visualization of the structures

After we derive the residuals for the entire time series (from ∼70 km to the apogee of the rocket trajectory; see right panel of Fig. 5.1), the next step in our new technique is to calculate the wavelet power spectrum. This spectrum is usually presented as a color-coded image in the wave number (spatial scale) -altitude plane, as explained in detail in section 5.2. An example of the scalogram derived for the residuals shown in the right panel of Fig. 5.1 is presented in Fig. 5.10.

From this scalogram one can see how structures of different sizes are organized in space along the rocket trajectory. Red color reflects high power values; black, the instrumental noise. One can see that structures of the size of a kilometer appear almost everywhere along the rocket trajectory, whereas small-scale structures intermittently appear at certain altitudes with a high variability at scales of ∼ 10 m.

This three-dimensional spectrum (the third dimension is color-coded) consists of ∼ 170 000 (= number or points in the time series) two-dimensional *local* wavelet power spectra. Each of these local spectra can now be analyzed with respect to turbulence, as is done in the standard analysis (section 5.2) with the Fourier spectra. That is, one can fit a theoretical model [e.g. *Heisenberg*, 1948] to each of the local spectra to yield the turbulence dissipation rate, ε.

The time resolution of the wavelet analysis, however, decreases the reasonable number of fitting operations. It is more reasonable to average the local spectra over some altitude (time) interval that gives the *global* wavelet spectrum over this altitude range. These global wavelet spectra are subject to the fitting procedure in our turbulence analysis technique. The appropriate width of the averaging window depends on the time resolution of the wavelet analysis. For the Morlet-24 we have the altitude resolution $\sigma^z \approx 5l$, where l is the spatial scale. That means that using Morlet-24 analysis we smooth the structures of a ∼20 m extent over ∼100 meters. Note that the Fourier analysis does such a smoothing over the entire altitude bin (that is, over ∼1 kilometer); however, making use of the Morlet-6 wavelet function allows resolution of ten meter structures at nearly ten meters of vertical resolution. The 20 m spatial scale is the typical value for the inner scale of the mesospheric turbulence [*Lübken*, 1993; *Lübken et al.*, 1993]. This implies that the viscous part of the turbulence spectrum lies between ∼20 m down to some meters. This means, that using Morlet-24 analysis we are able to catch the change of the dissipating part of the energy spectrum at a ∼100 m resolution.

If we compare the scalogram presented in Fig. 5.10 with the power spectrum of the same time series but derived using Morlet-6 wavelet analysis (with the finer/coarser time/frequency resolution), presented in Fig. 5.11, we see nearly the same structuring within the meters scales and a general qualitative agreement within the hundred to thousand meter scales.

We further compare these wavelet analyses (Morlet-6 and 24) in the following subsection. Here we note that we choose Morlet-6 analysis whenever it is possible; however, if data quality is poor (e.g., due to changing spin frequency), we recommend using Morlet-24 analysis, since it has better frequency resolution.

Note als, that from the presented plots (Fig. 5.10 and 5.11), because the time (altitude) range is too large, we cannot see much variability and difference within the dissipating part of the energy spectrum: that is, from meter to ∼50 meter scales.

5.4.2 Dissipation rates - improved resolution

The benefits of the wavelet spectral analysis in application to mesospheric turbulence can be better demonstrated if we zoom the wavelet spectrum to the 1 km bin analyzed by the standard

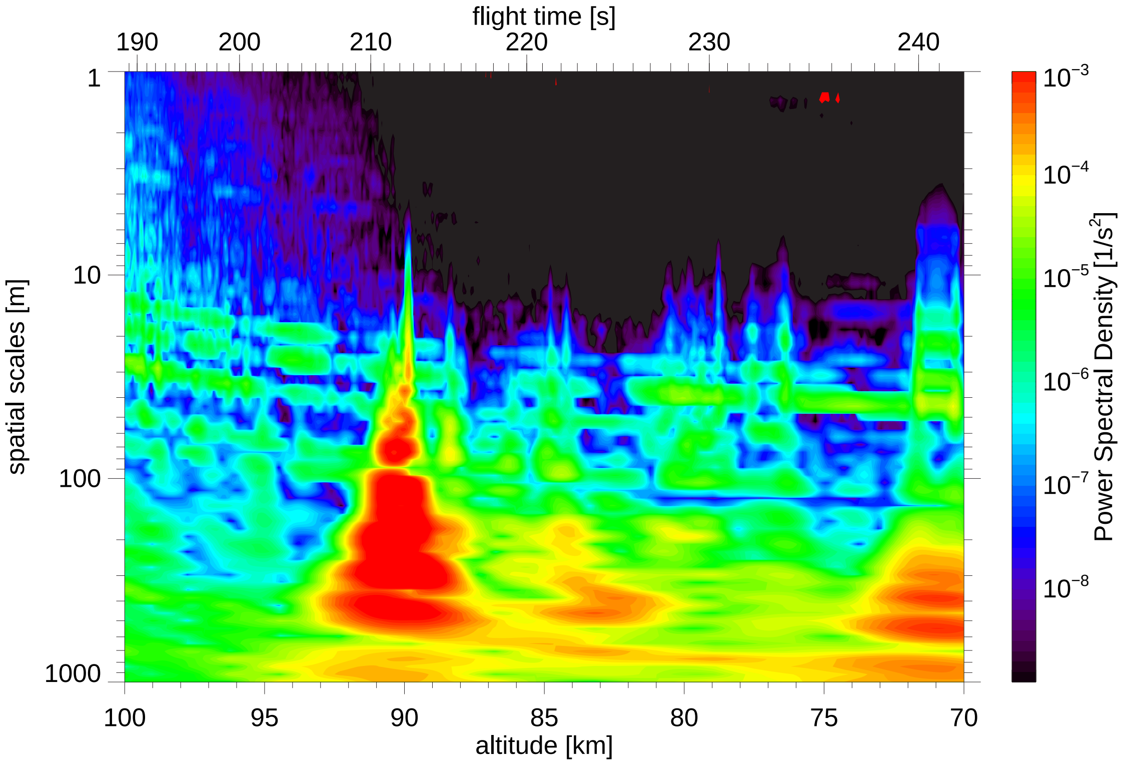

Figure 5.10: Wavelet power spectrum of the relative neutral air density fluctuations. Wavelet function: Morlet-24. Flight: MM-MI-12, date: 2 July 2002, time: 1:44 UT.

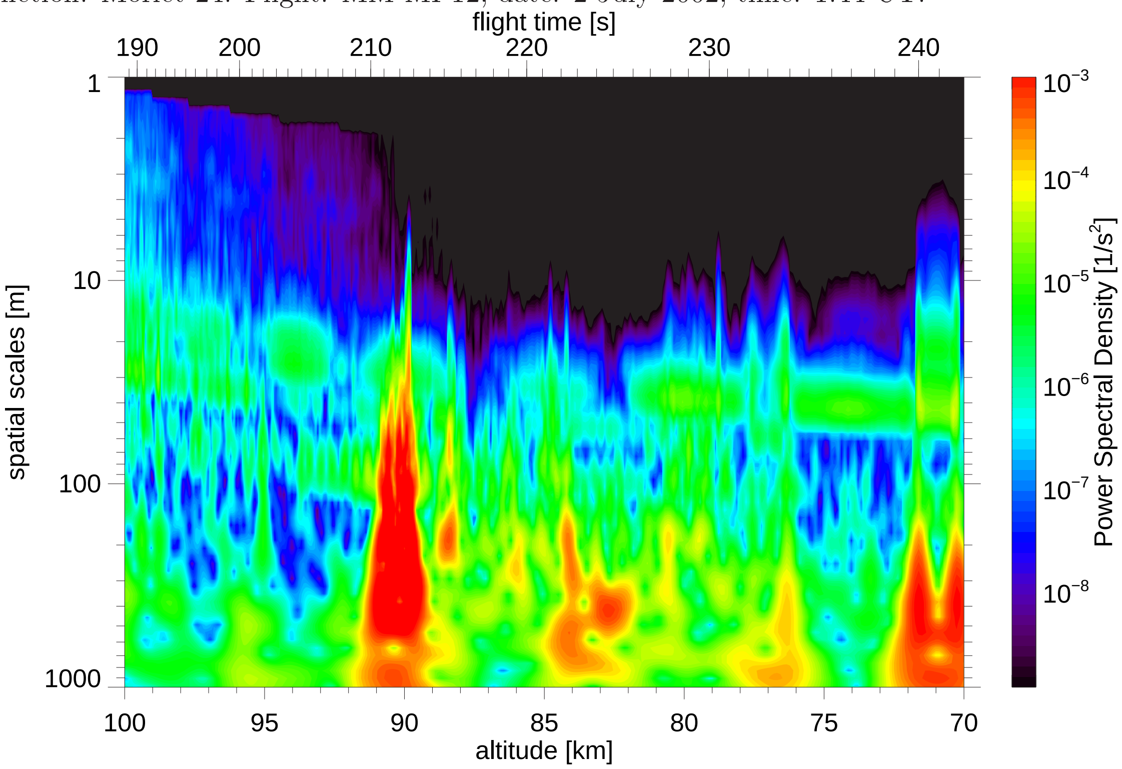

Figure 5.11: The same as 5.10 but using Morlet-6 wavelet function.

Fourier method in the previous chapter. Fig. 5.12 shows an enlarged part of the scalogram shown in Fig. 5.10 around 85 km. The blue color which corresponds to the power values of $\sim 5 \cdot 10^{-7}\ s^{-2}$ reveals a structuring within the height intervals of ~100 m extent, which is about the resolution of the analysis. The corresponding contour line, which corresponds to the transition between the smallest scales resolved by our instrument and instrumental noise, varies significantly within the 1 km height interval. This means that the viscous part of the energy spectrum, and hence the dissipation rate, ε, changes.

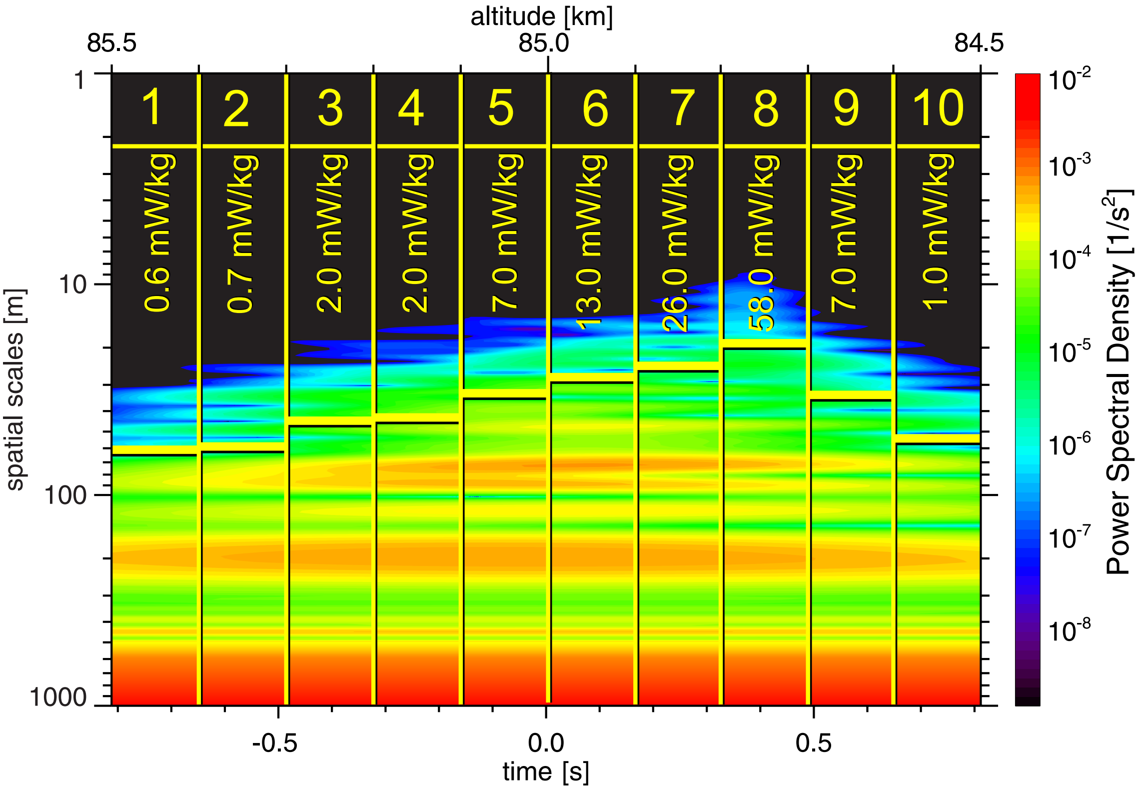

Figure 5.12: Wavelet power spectrum of the 1 km bin taken at the 85 km altitude. The bin was split into 100 m sub-bins which is shown by the vertical lines and its sequence number. The global wavelet spectrum of each of the 100 m sub-bins was fitted by the spectral model, and results are shown: The horizontal line marks the derived inner scale (l_0^H), and energy dissipation rate (ε) value in mW/kg is printed for each bin.

To better demonstrate the described behavior we subdivide this 1 km bin into 100 m sub-bins. This is demonstrated in Fig. 5.12 by the vertical lines. Then we fit the same (as in the standard case) spectral model [*Heisenberg*, 1948] to each of these sub-bins. This yields the inner scales marked by the horizontal line for each 100 m interval. The turbulence dissipation rates converted from the inner scales are also shown in the plot. It is seen that the inner scale changes from 60 m to 20 m, which implies that the dissipation rate varies from 0.6 mW/kg to ~60 mW/kg: that is, two orders of magnitude. Note that the standard technique that uses entire 1 km bin results in a value of ~13 mW/kg.

To more traditionally demonstrate the same result, we compare the global wavelet power spectra of these smaller bins with the global wavelet and the Fourier spectrum of the entire 1 km bin. Fig 5.13 shows this comparison. Each plot in Fig. 5.13 shows the Fourier power spectrum of the entire 1 km bin as dotted profile (the same spectrum as shown in the left panel of Fig. 5.3). The left upper-most plot in Fig. 5.13 demonstrates that the global wavelet spectrum of the entire altitude bin (black bold profile) gives us the smoothed version of the Fourier power spectrum. After the fitting of a theoretical spectrum (red dashed line) this yields the same turbulent characteristics as our Fourier technique does.

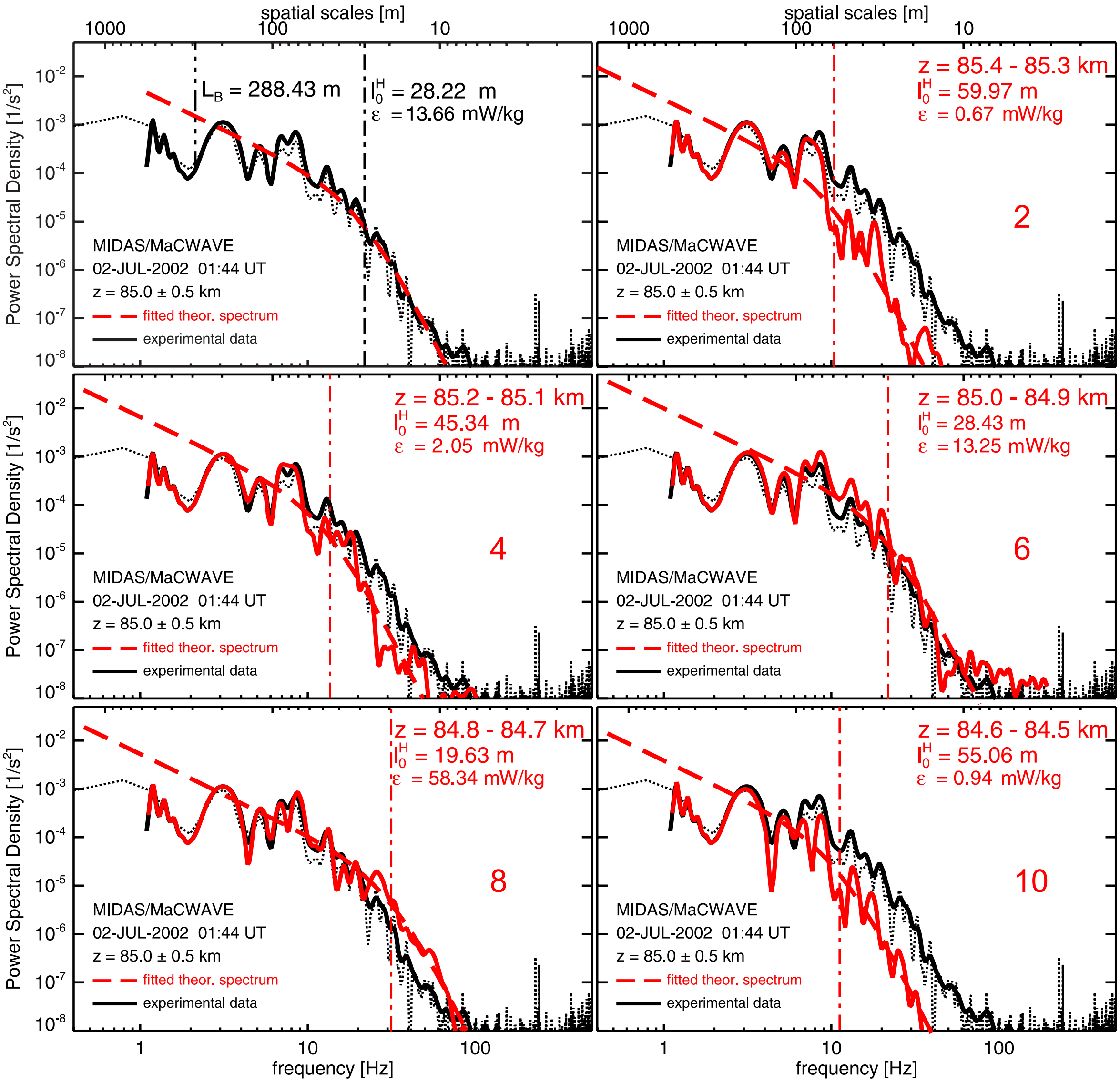

Figure 5.13: Global wavelet power spectra of the 100 m sub-bins within the 1 km bin taken at the 85 km altitude. The dotted profile shows the Fourier power spectrum of the entire 1 km bin (also shown in the left panel of Fig. 5.3). The bold black profile shows the global wavelet spectrum of the entire 1 km bin. The bold red profiles represent the global wavelet spectra of the 100 m sub-bins marked in Fig. 5.12 by numbers also shown here. The red dashed curve shows the fitted spectral model of *Heisenberg* [1948]. The vertical dash-dotted line marks the inner scale, l_0^H, derived from the fit.

Then we pick up five global wavelet spectra of the 100 m sub-bins within this kilometer bin and show them (red bold profiles) together with the fitting results. The red dashed line represents the fitted theoretical spectrum, and the vertical dash-dot line marks the derived inner scale. The dissipation rate, ε, is also shown in each case. Plots in Fig. 5.13 are marked by the numbers that correspond to the numbers shown at the top of Fig. 5.12.

It is seen that the dissipation range of the spectra changes around the mean power spectrum (black bold profile in Fig. 5.13) to the both sides, to the stronger and to the weaker turbulence (smaller and larger scales). Only one spectrum (number 6) results in the dissipation rate that is close to the mean value ~13 mW/kg.

If we apply the same procedure to the wavelet power spectrum derived using Morlet-6 wavelet function, we get the following results (Fig. 5.14). Qualitatively, the Morlet-6 spectrum repeats the behavior shown by the Morlet-24 spectrum (Fig. 5.12): however, as discussed in section 5.3, the time (altitude) resolution of the Morlet-6 analysis is better (at the expense of the frequency resolution) and corresponds to the vertical resolution of the order of the measured spatial scales. It allows us to see the actual vertical size of the mesospheric turbulent structures.

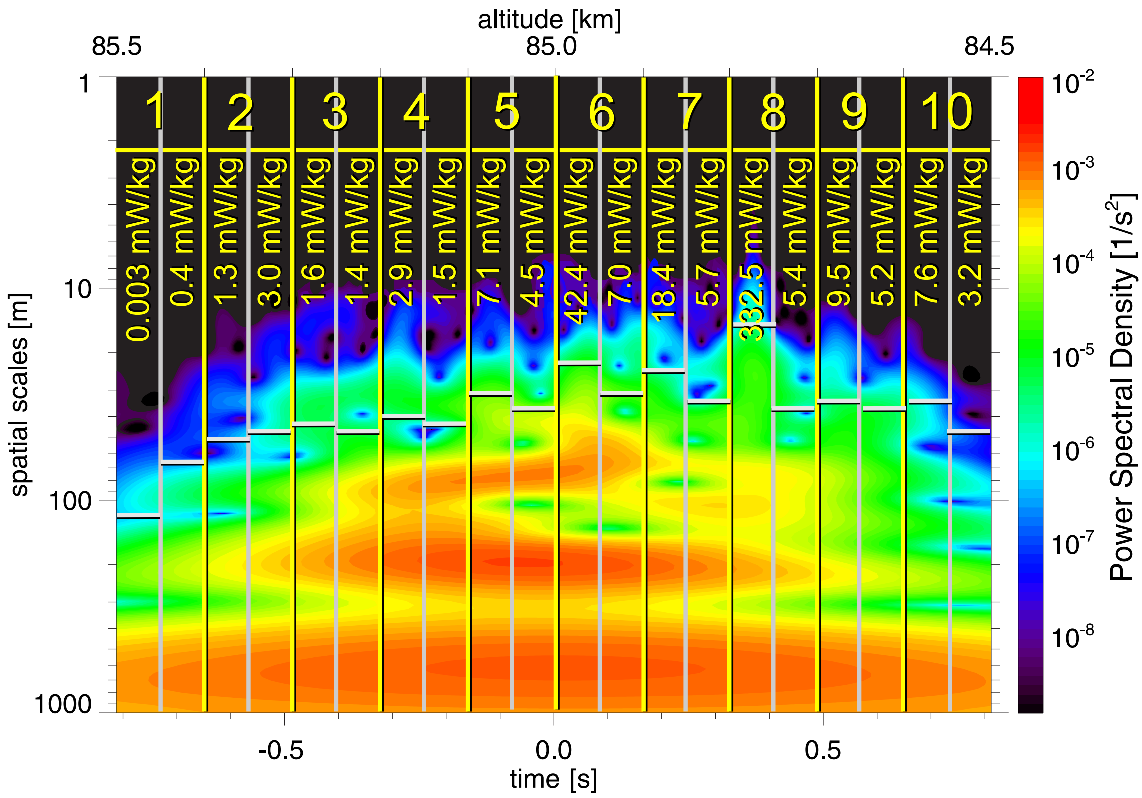

Figure 5.14: Wavelet power spectrum of the 1 km bin taken at the 85 km altitude. Morlet-6. The bin was split into 100 m sub-bins, which is shown by the vertical lines and its sequence number. The global wavelet spectrum of each of the 100 m sub-bins was fitted by the spectral model, and results are shown: The horizontal line marks the derived inner scale (l_0^H), and energy dissipation rate (ε) value in mW/kg is printed for each bin.

The scalogram in Fig. 5.14 discovers more time (altitude) variability of the structures at different scales. The investigated turbulent patch (85 km bin) has even finer structuring within the dissipation energy subrange than it was found above (using Morlet-24 analysis). Aside from the highly variable structuring on the scale of tens of meters, there is also quite a variability on the scales of hundreds of meters. Since we are interested in the change of scales around the turbulent inner scale ($l_0 \simeq 50 - 10$ m) and smaller, a vertical resolution of 50 m is a realistically reasonable choice for deriving the global wavelet spectra.

We perform the same procedure as we applied to the Morlet-24 power spectrum, and we deduce the inner scales, l_0^H, and energy dissipation rates, ε, for 100 m sub-bins. The derived values (not shown in Fig. 5.14) are close to those derived above using Morlet-24 analysis (Fig. 5.12). Next, we further subdivide the investigated 1 km bin into 50 m sub-bins and perform the same analysis. The derived inner scales are shown in Fig. 5.14 as horizontal lines. On average, they reveal a similar behavior as in the case of a vertical resolution of 100 m: however, one sees a more variable l_0 (ε) -field. It is also clear that the maximum of the l_0 (ε) -profile, or the strongest part of the turbulent patch, has an even smaller vertical extent than the 100 m resolution technique implied.

Finally, in Fig. 5.15 we compare the Fourier spectrum with the wavelet spectra using time (altitude) -resolved color scalogram (and the same vertical, horizontal, and color scales). It

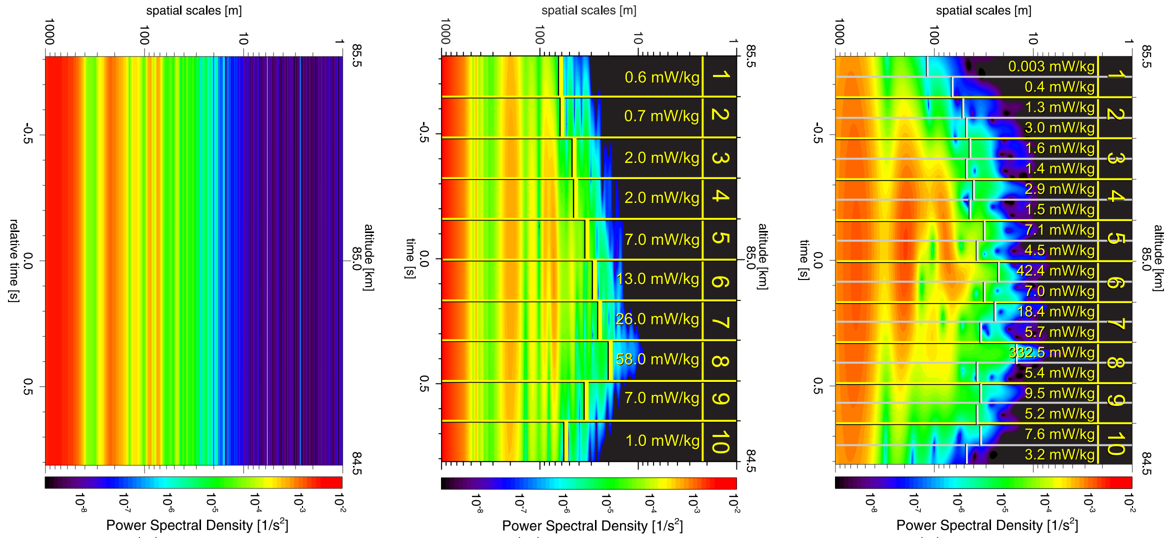

(a) Fourier (b) Morlet-24 (c) Morlet-6

Figure 5.15: Comparison of the time (altitude) resolution of the Fourier power spectrum and wavelet spectra.

shows that the Fourier analysis (which is by definition heavily smoothed in time) gives a rather rough estimate of the real structuring, and although the 100 m smoothed analysis does not resolve the actual vortex pattern, it already shows a much more realistic structuring.

Though the Morlet-6 wavelet analysis seems to be a nearly perfect choice, rocket-specific features (like spin frequency modulation), however, force a trade-off between time and frequency resolution, and very often the Morlet-24 analysis is a better choice.

Another argument for the time-resolved analysis (wavelet against the Fourier) of the turbulent structures comes from the fact that the mean over the highly resolved ε-values (which should better reflect the reality) does not approach the ε-value derived from the spectrum, which is smoothed over the same altitude interval. Also, the wider the smoothing window, the bigger the difference. We demonstrate this difference in Fig. 5.16 where the solid line shows the result of the Fourier analysis, which has the coarsest time (altitude) resolution: i.e., the entire 1 km bin. The dashed histogram represents the ε-value, deduced from the 100 m smoothed spectra derived using Morlet-24 analysis. The dash-dotted histogram uses the 50 m smoothed spectra derived using Morlet-6 wavelet analysis.

The horizontal dashed and dash-dotted lines in Fig. 5.16 represent the mean values, derived from the 100 m and 50 m smoothed spectra, respectively.

The implications of the improved analysis technique are also demonstrated in Fig. 5.17

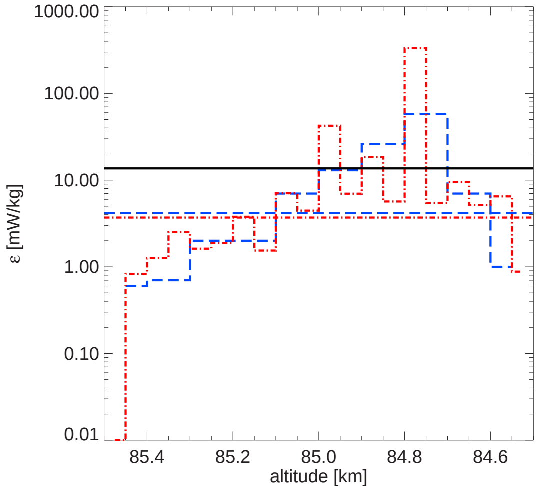

Figure 5.16: Comparison of different resolutions. The solid line represents the result of the Fourier technique (most coarse). The dashed line represents the ε-values derived from the Morlet-24 analysis (≈100 m resolution), and the dash-dotted line utilizes the 50 m resolved spectra (derived from the Morlet-6 analysis)

where red crosses represent the result of the old (standard) analysis technique and the blue histogram with green error-bars shows the new result. It is seen that the two results generally agree, but the new result reveals the finely structured turbulent energy dissipation field, as it was derived from the scalograms. One can clearly see sharp gradients in the turbulence dissipation field discovered by the fine resolved ε-values (blue histogram) which cannot be seen from the coarse-resolution technique (red crosses). The dashed line in Fig. 5.17 shows an estimate of the smallest possible inner scale of turbulence, l_{min}, described in section 2.5.

The best choice from the time/altitude resolution point of view is the Morlet-6 wavelet function. The Morlet-24 wavelet analysis also gives very high time/altitude resolution of ~100 m for our typical rocket flight. They give reasonably close quantitative results, however. The Fourier analysis gives extremely coarse time/altitude resolution in comparison with the wavelet analysis.

5.4.3 Morphology of turbulent structures

In this section we address the question of how turbulent structures of different spatial scales (eddies of a different size) are organized in space. We start with the discussion of large scales, from ~100 m to ~1 km, reflected by the scalograms. It is seen that the altitude (rocket flight time) variation of the structure within these spatial scales is better reflected by the Morlet-6 scalogram (Fig. 5.11). Let us consider a slice of this spectrum at, for example, 800 m along the altitude axis (horizontal in the plane of the plot). Following from 70 km altitude up to ~93 km, we see four active regions as marked in Fig. 5.18: 1) from $\sim 70\ km$ to $\sim 72.5\ km$, 2) $75.5 - 78\ km$, 3) $82 - 85\ km$, and 4) $90 - 92\ km$. Let us call them turbulent "patches." Starting from ~700 m scales (and further to smaller scales) these patches begin to split into sub-patches. Let us take another slice at 200 meters. Now we can recognize more patches: e.g., at least another two active regions between patches 2 and 3. These new structures do not extend to scales as large as the four bigger ones. This may imply that either energy input at bigger scales had already been finished some time before we probed that region or energy input takes place at these scales. The first interpretation comes directly from the

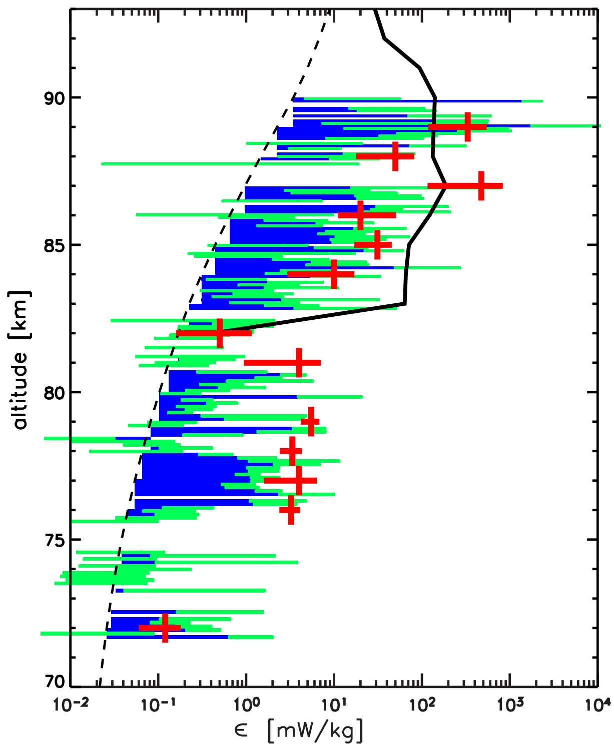

Figure 5.17: Comparison of the old (standard) turbulence analysis technique represented by the red crosses and the new turbulence analysis technique represented by the blue histogram with green error bars. Flight: MM-MI-12, 2-JUL-2002, Andøya Rocket Range, 69 °N, 15 °E. After *Strelnikov et al.* [2003].

energy cascade hypothesis (see section 2.1). The second assumption is not consistent with the energy spectrum (section 2.1, Fig. 2.1) of turbulence if we consider local wavelet spectra (see section 5.3 and further Fig. 5.13), since buoyancy and energy subranges are missing (power at larger scales goes down). Therefore, it is not likely the reason.

Such a tendency of the patches to subsequently split into sub-patches can further be seen when following from large scales to smaller ones (for most of the patches seen in the plot, see also Fig. 5.14). It is consistent with the energy cascade hypothesis.

To study the morphology of the turbulent patches we further go to the smaller scales. Though the Morlet-24 analysis (Fig. 5.10) smoothes the measured structure in the time domain, this effect cannot be seen within the smallest scales, from meters to ∼100 m, at the presented scaling of the plots (Fig. 5.10 and 5.11). Within the smallest spatial scales one sees the same features, and, therefore, we discuss them using one of them in the following plot (Fig. 5.18). In this plot we concentrate on the structure that takes its origin at the largest scales between ∼76 and 78 km altitude (patch 2). In Fig. 5.18 we overplotted the inner scales, l_0^H, derived using global spectra smoothed over 100 m. These values reflect the strength of turbulence: The smaller the l_0^H-value the stronger the turbulence (see Eqq. 2.1 and 2.2). One sees that the strongest turbulence occurs at the edges of the considered patch. The same is also clearly seen from ε-profile shown in Fig. 5.17. Such behavior can be found in the majority of the structuring as reflected by the scalograms. Though this is likely a common feature of the detected structuring, it is, however, not as obvious in some cases. Thus, considering the height region from 88 to 92 kilometers as a single patch, we get the strongest turbulence in the middle (see also Fig. 5.17). The reason for such a difference is potentially related to different

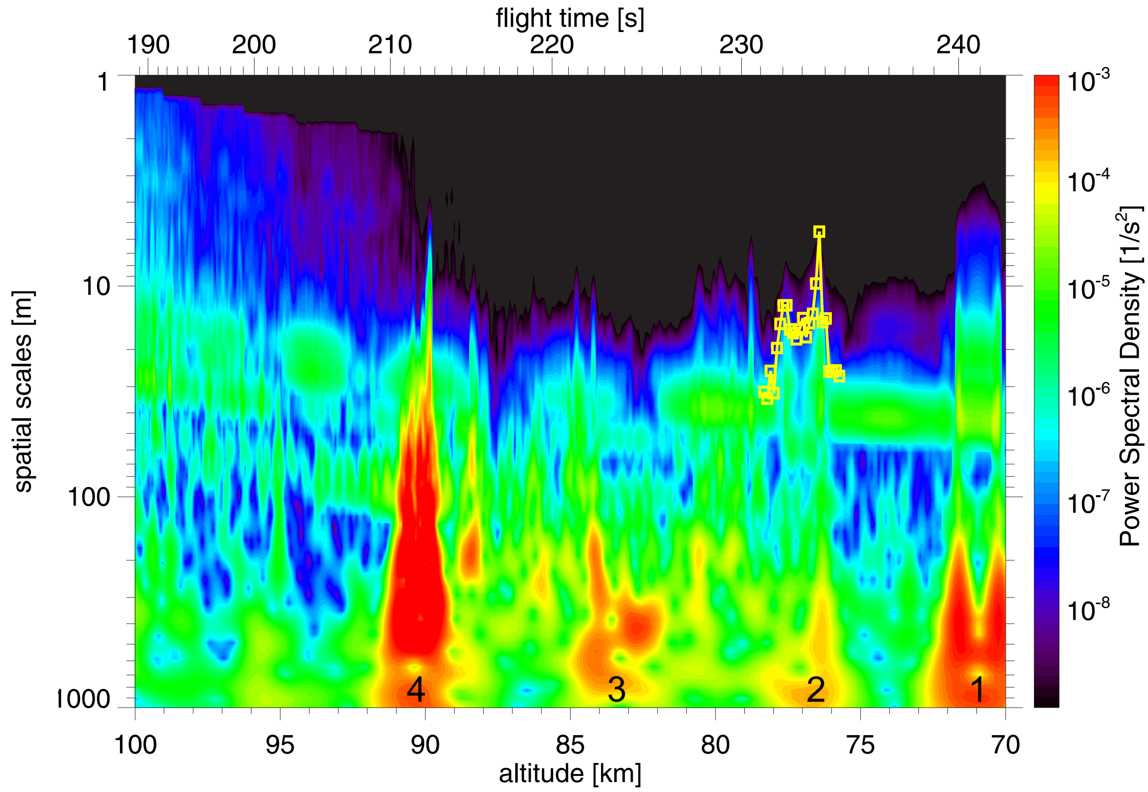

Figure 5.18: The same as Fig. 5.11. Additionally, the derived inner scales, l_0^H, for turbulent patch 2 (see text) are overplotted. The figure shows that the strongest turbulence (smallest l_0^H-values) are approximately at the edges of the patch.

sources of MLT turbulence [see e.g. *Fritts et al.*, 2003] and is planned for further investigation in the near future.

Coming back to the smallest scales, we point out on another feature of the turbulence field that can now be seen from both the scalograms and ε-profile plot (Fig. 5.17). The structures are highly intermittent (remember that we assume ergodicity): that is, the layers are sharp, thin, ε-value changes rapidly and discontinuously. This emphasizes the advantage of the wavelet technique (as discussed in section 5.3.2) that allows resolution of the small scale (high frequency) content that changes quickly in time (altitude) domain.

Most of the experimentally discovered features discussed above were previously observed in different turbulent flows and are the guiding line for turbulence modelers [see, e.g., review by *Farge et al.*, 1999]. The discussed advantages of the wavelet transform attract the developers of the turbulence models to use the wavelet instead of Fourier basis in their simulations [e.g. *Farge*, 1992; *Kumar and Foufoula-Georgiou*, 1997; *Farge et al.*, 1999] .

5.5 Analysis technique: Summary

The first novelty of the presented work is the improvement of the analysis technique. In this chapter we demonstrated new possibilities that rise if we apply this method to the in situ measured neutral density fluctuations. These new implications are:

1. Time/altitude – frequency/spatial scale resolved energy spectrum.

2. Turbulence dissipation rate, ε, profile with a high altitude resolution: smoothing window

of ∼100 m and less against the 1 km at the best of the old (standard) technique.

The first advantage of the time-resolved analysis allows us to gain insight into the spatial organization of the turbulent structures (section 5.4.3). Such a scale analysis, however, must certainly be improved to give quantitative criteria to distinguish between different types of structures and thereby draw conclusions about the sources that created these structures.

The second implication explicitly shows the turbulence dissipation field with its vast of features hidden by the old analysis method. These features are the intermittency, sharp gradients, and distribution of the dissipation within the single patch.

Chapter 6

Geophysical results: Turbulence

In this chapter the results of the turbulence measurements conducted during two sounding rocket campaigns are presented. These are the MIDAS/MaCVAVE and ROMA/SvalRak campaigns. A short overview of these campaigns is given in sections 6.1.1 and 6.2.1, respectively. Then, for each of these two campaigns, a detailed examination of the measurements and summary of the important results are subsequently presented. Finally, the results of these campaigns are compared, and an outlook to near future rocket soundings and anticipated geophysical results are given.

6.1 MIDAS/MaCWAVE project (69 °N)

6.1.1 Campaign overview

The MIDAS/MaCWAVE, a collaborative sounding rocket and ground-based measurement campaign, was a joint European-American project devoted to the investigation of dynamical processes in the middle atmosphere. This campaign was conducted in July 2002 from the Andøya Rocket Range (ARR, 69.3 °N, 16.0 °E).

The American **MaCWAVE** (**M**ountain **a**nd **C**onvective **W**aves **A**scending **Ve**rtically) program included both winter and summer soundings. The summer part of their project was focused on gravity wave propagation, instability, and wave-wave and wave-mean flow interaction dynamics contributing to summer mesopause structure and variability.

The European **MIDAS** (**MI**ddle Atmosphere **D**ynamics **A**nd **S**tructure) program was a collaborative German-Norwegian project focused on small-scale dynamical and microphysical processes near the summer mesopause.

In summer 2002, our merged program yielded a comprehensive data set comprising two ∼12-hour rocket salvoes, including 25 MET rockets and five sounding rockets, ground-based lidar and radar data, balloon soundings, and coordinated overpasses of the TIMED satellite. Results from this campaign were highlighted in a special issue of the journal Geophys. Res. Lett. [*Goldberg and Fritts*, 2004] and the overview of the campaign can be found in *Goldberg et al.* [2004].

In this chapter we concentrate on the turbulence measurements conducted by means of the CONE instrument (see section 4.5.1) onboard the MIDAS payloads. We also use the results of the MET rocket soundings (namely, falling spheres (FS), see section 4.5.3) and radar measurements. In Appendix B.1 such technical details as date, time, label, and apogee of the rocket flights as well as the instrumentation set for each launched rocket are summarized.

The Polar Mesospheric Summer Echoes (PMSE) recorded by the ALOMAR Wind (ALWIN) radar [*Latteck et al.*, 1999] during the days of the rocket flights are shown in Fig. 6.1. The rocket flight times are marked by the vertical lines in Fig. 6.1. It is seen that most of the rockets were launched under conditions of strong PMSE, which is indirect evidence for dynamical activity in the MLT region [see *Rapp and Lübken*, 2004, for a detailed review on PMSE].

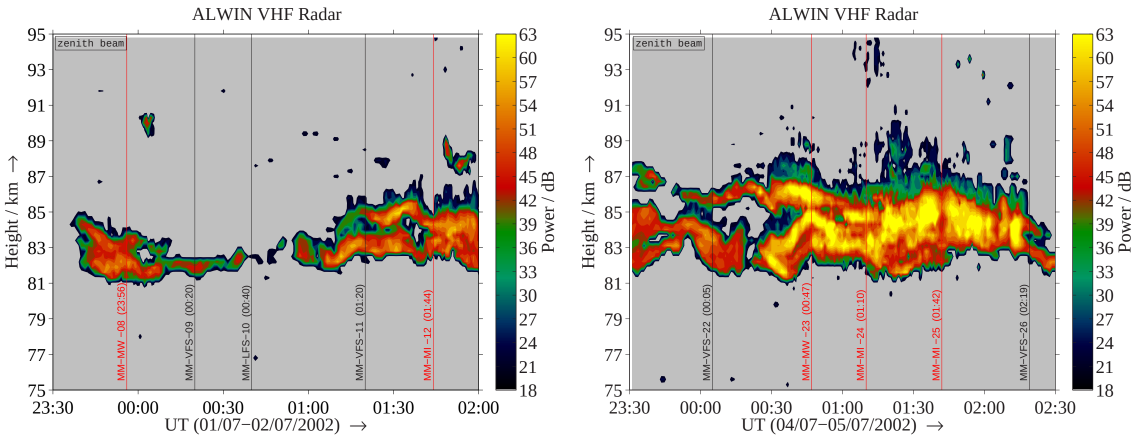

Figure 6.1: PMSE display recorded by the ALWIN radar during the MIDAS/MaCWAVE campaign in July 2002 [*Goldberg et al.*, 2004]. Vertical, labeled lines mark the time of rocket launches: black for MET-rockets and red for instrumented rockets. Courtesy of R. Latteck.

6.1.2 Measurements: Background atmosphere

The atmospheric background state parameters are the altitude-profiles of temperature, density, and other meteorological parameters, which are smoothed over some altitude interval such that they do not contain any small-scale structuring. Aside from the standalone importance of measuring the background state parameters, they are also needed for the small-scale analysis, namely for the quantitative analysis of the mesospheric turbulence structures (see section 5).

During the MIDAS/MaCWAVE campaign in summer 2002, three MIDAS payloads were aimed to measure in situ the density (direct measurements applying ionization gauge, section 4.5.1) and temperature altitude-profiles with a high precision. This technique, however, requires stable flight conditions. Specifically, the angle of attack (angle between the rocket velocity vector and symmetry axis of the rocket) must not exceed a value of 60 ° [see *Rapp et al.*, 2001, for details]. Apart from the direct in situ measurements of the background parameters with the CONE instrument, the indirect but extensive falling spheres (FS) soundings (see section 4.5) conducted throughout the entire campaign yielded reliable measurements of the density, temperature, and wind fields [*Goldberg et al.*, 2004; *Rapp et al.*, 2004]. Appendix B.2 summarizes the status of all the experiments conducted during this campaign.

The following figures (Fig. 6.2 and Fig. 6.3) summarize the measurements of the background atmosphere densities and temperatures conducted during the MIDAS/MaCWAVE campaign in summer 2002.

All the falling sphere density and temperature measurements are presented in Fig. 6.2(a) and 6.2(b), respectively.

The result of the background density measurements (CONE density measurements) conducted during the first flight (MM-MI-12) of the MIDAS payload is presented in Fig. 6.3(a) as a solid profile. The result of the neutral air temperature measurements (CONE temperature measurements) conducted during the same flight is presented in Fig. 6.3(b) as a bold profile.

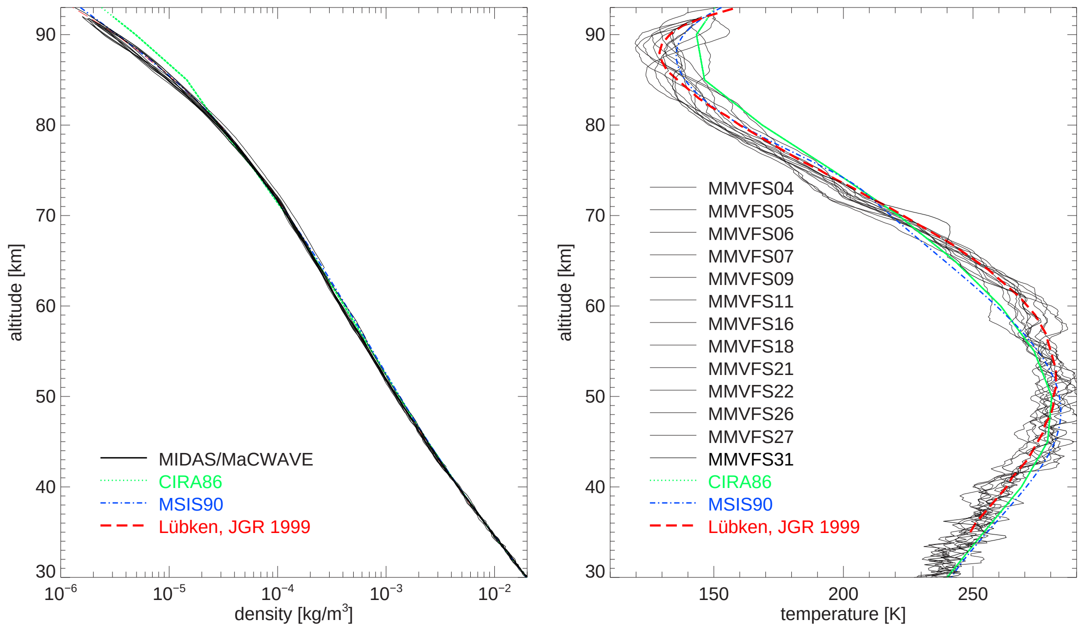

(a) (b)

Figure 6.2: FS measurements during MIDAS/MaCWAVE summer campaign in 2002. Reference profiles are taken from CIRA-86 [*Fleming et al.*, 1988] and MSIS-90 [*Hedin*, 1991] models and from FS-measurements by *Lübken* [1999].

In Fig. 6.4 the mean temperature derived from the falling sphere measurements during the MIDAS/MaCWAVE campaign is shown as red and during previous years as blue profile. One can see that the temperature around mesopause ($\sim$ 92 down to $\sim$ 82 km) is higher during MIDAS/MaCWAVE than in the "normal" case. Warmer mesopause might imply less upwelling and, therefore, weaker meridional winds at this region (see section 1.2.1, Eq. 1.3). Below that region, from $\sim$82 km down to $\sim$60 km, the MIDAS/MaCWAVE temperature is lower. The lower temperatures in turn imply stronger upwelling and, therefore, stronger (more southwards) meridional winds.

6.1.3 Measurements: Turbulence

As was described in the previous sections, for the turbulence analysis we use the background atmosphere as derived from the in situ measurements presented above.

The main steps (with some intermediate results) of our turbulence detection technique, described in chapter 5, are highlighted in the following subsections.

Neutral density fluctuations: Residuals

The relative neutral air density fluctuations (residuals) measured by the CONE instrument during the flights MM-MI-12, MM-MI-24, and MM-MI-25 are presented in Fig. 6.5, 6.6, and 6.7 respectively. These plots cover the altitude range from 100 down to 70 km. This is the height interval where the CONE instrument effectively works. Note that the flight MM-MI-24 (Fig. 6.6) had a low apogee of $\sim$ 90 km: That is, there is no data available above $\sim$ 90 km during this flight.

Note also that the percent-scale fluctuations seen in these plots correspond primarily to the large-scale eddies that contribute to the inertial part of the energy spectrum. As can be

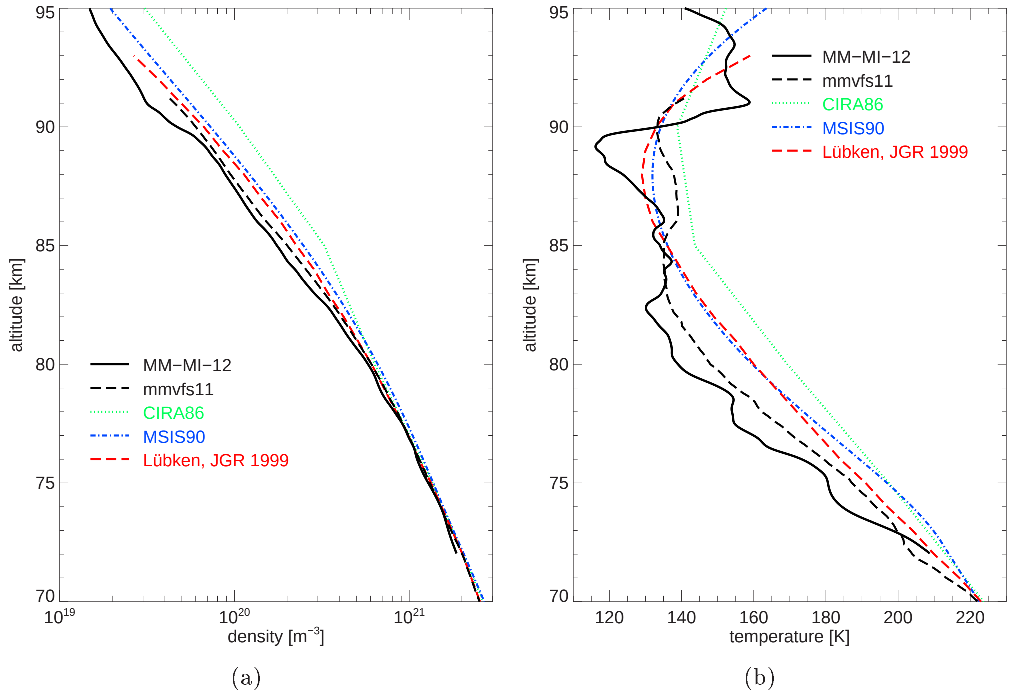

Figure 6.3: CONE measurements conducted during the flight MM-MI-12 (2-JUL-2002, 1:44 UT). Reference profiles are taken from CIRA-86 [*Fleming et al.*, 1988] and MSIS-90 [*Hedin*, 1991] models and from FS-measurements by *Lübken* [1999]. The FS measurements conducted $\sim$ 20 min before the MM-MI-12 flight are shown by the black dashed profile (mmvfs11, 2-JUL-2002, 1:20 UT).

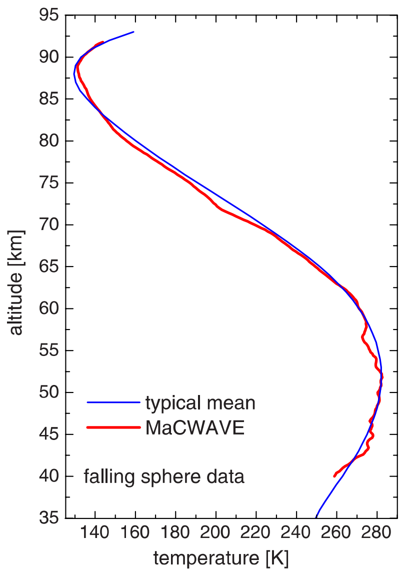

Figure 6.4: Mean falling sphere temperature measurements in summer 2002 (red) and during previous years (blue). Temperature gradient near the mesopause ($\sim$ 87 down to $\sim$ 82 *km*) is smaller, and from ~82 km down to ~60 km it is larger during MIDAS/MaCWAVE (red) than usual (blue). Also between 82 and 60 km the MIDAS/MaCWAVE temperature is lower than usually. After *Goldberg et al.* [2004].

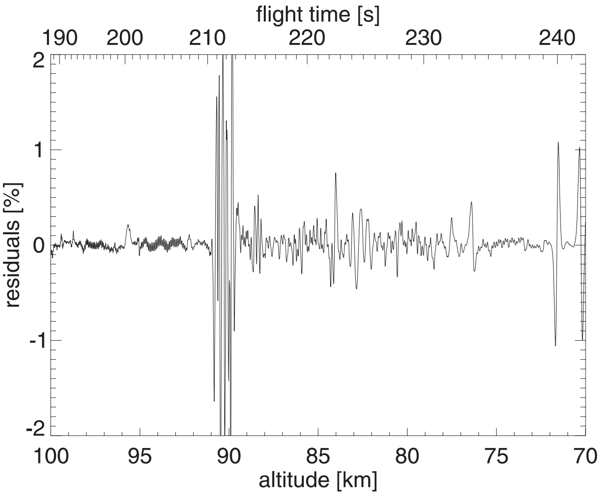

Figure 6.5: Relative neutral air density fluctuations (≡ residuals) altitude-profile measured by the CONE instrument during the flight MM-MI-12 (Andøya, 2-JUL-2002, 1:44 UT).

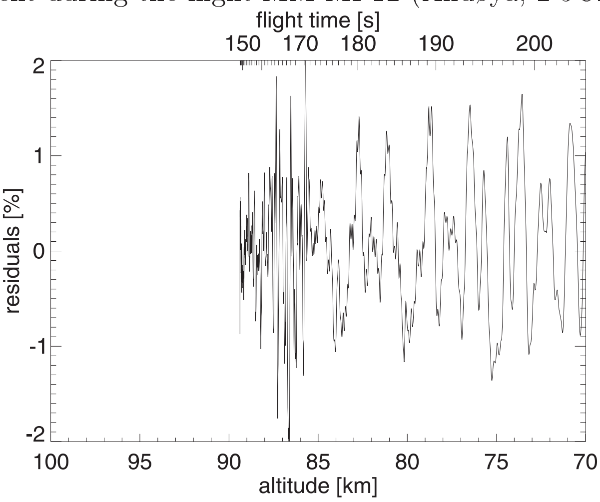

Figure 6.6: The same as 6.5 but for the flight MM-MI-24 (Andøya, 5-JUL-2002, 1:10 UT).

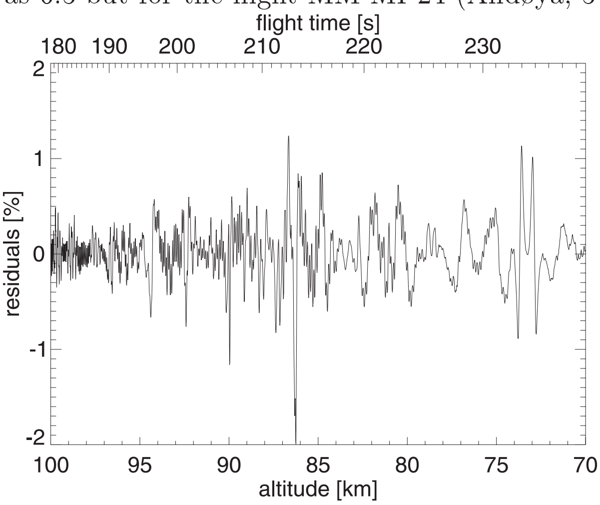

Figure 6.7: The same as 6.5 but for the flight MM-MI-25 (Andøya, 5-JUL-2002, 1:42 UT).

seen from the Kolmogorov spectrum (Fig 2.1), the fluctuations that contribute to the viscous part of the turbulent spectrum have amplitudes that are orders of magnitude smaller than the amplitudes of the inertial subrange fluctuations.

Neutral density fluctuations: Scalograms

In the following plots (Fig. 6.8, 6.9, and 6.10) we present the wavelet scalograms, derived as described in section 5.3 using Morlet-6 wavelet analysis, for the flights MM-MI-12, MM-MI-24, and MM-MI-25, respectively. The power (in units $[\%/s]^2$) is color-coded, as shown by the color bar on the right side. The dark-blue to black colors reflect the noise level of $\sim 10^{-8} - 10^{-9}\ s^{-2}$. White color reflects the highest power, exceeding the largest value shown in the color bar ($10^{-3}\ s^{-2}$).

As described in section 5.4.1, the largest variability of the turbulent structures occurs at the small scales (tens of meters to some meters). As can be seen from the plots, this is the case for all the three flights. It is also clear that the highest activity was observed around the mesopause region: that is, around ~85 to 90 km altitude.

Common features seen from all three scalograms include sharp, local gradients in both small- and large-scale structuring: that is, in both turbulent kinetic energy production and dissipation. Also, the large-scale regions are bounded by layers of active small-scale structuring accompanying vigorous turbulence (like, e.g., around 85 to 90 km heights).

One also has to mention that prominent horizontally organized bands within the ~50 to ~10 m scale-range are the unfiltered spin harmonics that do not disturb the quantitative analysis because they contain relatively few data points.

From these scalograms the energy dissipation rates are further deduced.

Energy dissipation rates

Five hundred local wavelet spectra were averaged to yield the global wavelet spectra at a vertical resolution of ~100 m (see section 5.3, 5.4.2, and Fig. 5.13). These global spectra in turn were fitted by the spectral model of *Heisenberg* [1948] to yield the energy dissipation rates, ε (see section 5.3).

The final result (ε altitude profiles) for all three MIDAS flights is presented in Fig.6.11. The bold black line represents the mean summer dissipation rates (ε_{mean}) derived from the 19 in situ rocket soundings using the same measurement technique and our standard analysis technique [*Lübken et al.*, 2002]. This mean profile does not show any turbulence activity below an altitude of 82 km. Hence, this was the lower altitude limit of summer mesospheric turbulence ever observed before the year 2002.

The common features usually observed near summer polar mesopause, which are also seen in the MIDAS/MaCWAVE result, include high turbulence energy dissipation rates and sharp local gradients in turbulent energy dissipation. There was also no turbulence detected above ~95 km during the MIDAS/MaCWAVE campaign.

There are, however, two specific and distinct features in the measurements presented in Fig. 6.11. The first is that turbulence was detected in a broad altitude range of about 20 km during all three flights. This must be compared to a typical extent of turbulence activity of just a few kilometers, seen during previous rocket flights [*Lübken et al.*, 2002; *Müllemann et al.*, 2003]. The second is that turbulence was also observed at lower altitudes compared to the mean. In other words, the results of the in situ measurements during the MIDAS/MaCWAVE 2002 summer campaign showed unusually active low-altitude (below 82 km) mesospheric turbulence at 69 °N in summer. This feature, as will be shown in the next sections, has important geophysical implication. Note also that these two features are not a consequence

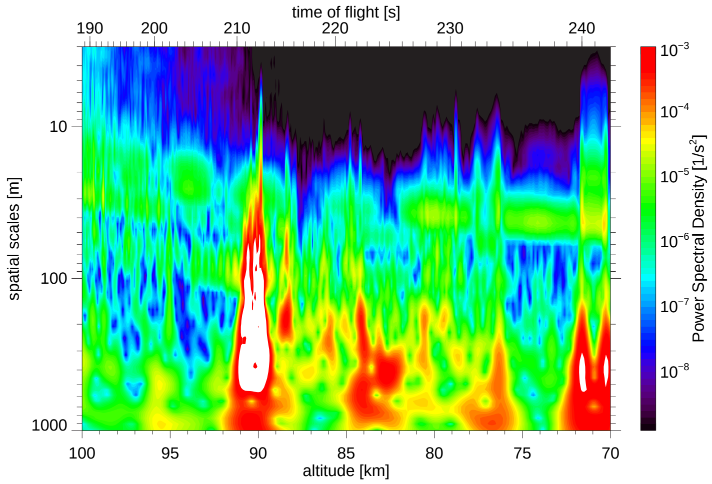

Figure 6.8: Wavelet power spectrum (derived using Morlet-6 wavelet function) of the residuals measured during the flight MM-MI-12 (Andøya, 2-JUL-2002, 1:44 UT).

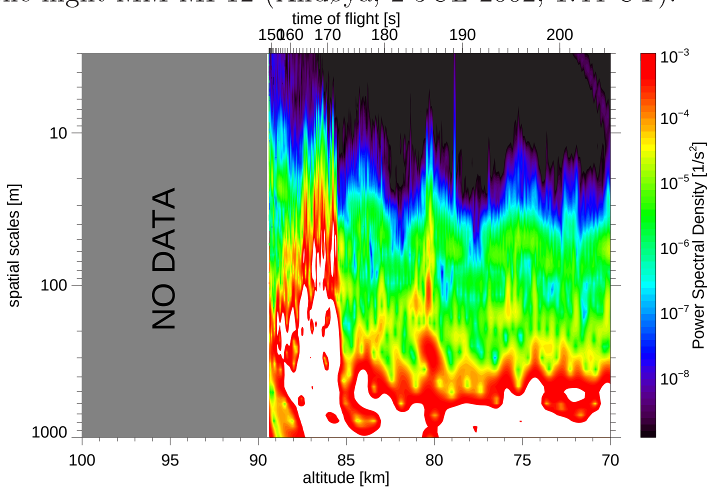

Figure 6.9: The same as 6.8 but for the flight MM-MI-24 (Andøya, 5-JUL-2002, 1:10 UT).

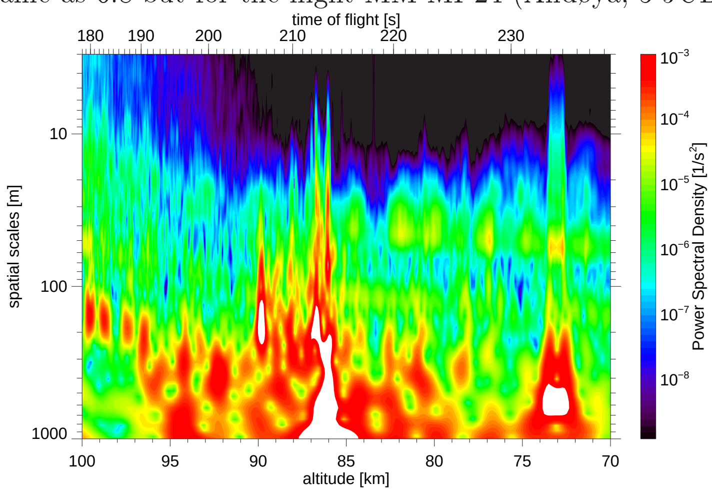

Figure 6.10: The same as 6.8 but for the flight MM-MI-25 (Andøya, 5-JUL-2002, 1:42 UT).

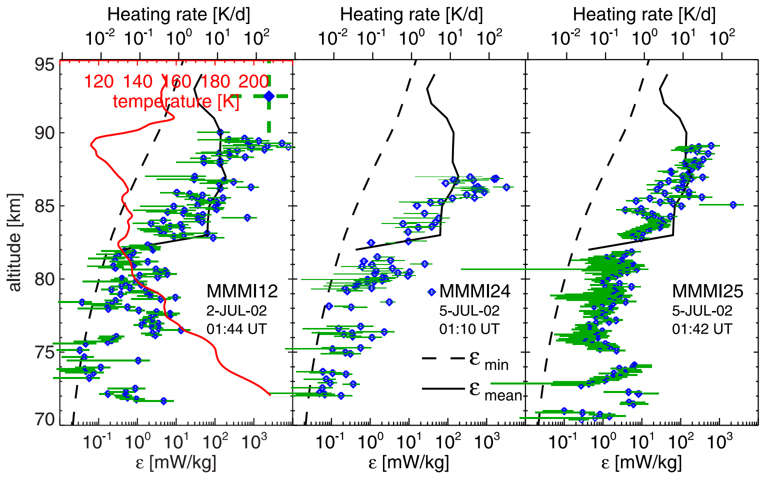

Figure 6.11: Turbulent energy dissipation rates (blue points) with error-bars (green) measured by the CONE instrument during the MIDAS/MaCWAVE 2002 campaign.

of the improved analysis technique. Rather, they represent the geophysical situation during the time of the soundings. This can also be seen in Fig. 5.17, where the result of the standard technique for the flight MM-MI-12 is compared to the result of the new technique, revealing a good agreement.

To understand the turbulence measurements results presented above we consider the other experiments simultaneously conducted during that campaign.

6.1.4 Accompanying measurements

As already mentioned above, gravity wave (GW) breaking is believed to be one of the major sources of turbulence generation near the mesopause region. Thus, the turbulence production at the lower altitudes (Fig. 6.11) might mean gravity wave breaking occurring at lower (than usual) altitudes.

GW signature

Now we investigate gravity wave signatures derived from the accompanying falling sphere (see section 4.5.3) temperature measurements [*Goldberg et al.*, 2004; *Rapp et al.*, 2004]. In Fig. 6.12 we compare two profiles of the quantity $(T'/T_0)^2$, one from twelve falling sphere measurements during the MIDAS/MaCWAVE campaign (red) and the other (black) from twelve falling sphere measurements accompanying the turbulence measurements during previous summers [*Lübken et al.*, 2002]. Here, $T' = \sqrt{\sum_{i=1}^{12}(T_i - T_0)^2/12}$ is the rms-variability of the twelve measurements at a fixed altitude, and T_0 is the corresponding mean temperature. Uncertainties of $(T'/T_0)^2$ are shown by the shaded area. Our analysis shows that differences are insignificant below ~75 km, but higher up there is a factor $\sim 2-4$ systematic difference in magnitudes. In order to identify the geophysical origin of this difference, it is instructive to compare the mean buoyancy frequencies, ω_B, of both data sets since gravity wave theory predicts that $(T'/T_0)^2 \propto \omega_B^3$ for unsaturated ($\propto \omega_B^2$ for saturated) waves [*Eckermann*, 1995]. From the mean temperature profiles underlying Fig. 6.12 we derive mean buoyancy frequencies at 81 km of $\omega_B^{MaCWAVE} = 0.019 \pm 0.001\ Hz$ for MIDAS/MaCWAVE and $\omega_B^{normal} = 0.015 \pm 0.001\ Hz$ for the "normal summer state." The ratio of these frequencies cubed (squared) is $[\omega_B^{MaCWAVE}/\omega_B^{normal}]^{3(2)} \approx 2$ (1.6) which largely explains the observed

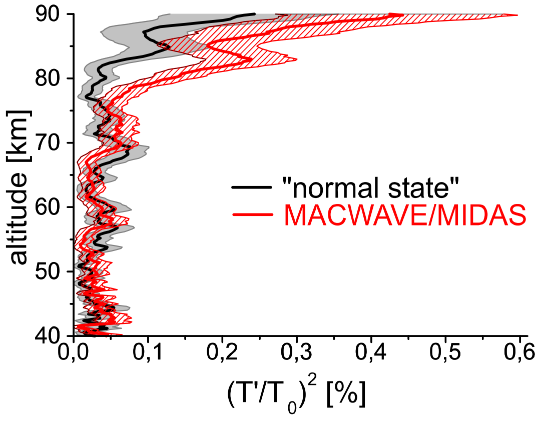

Figure 6.12: Profiles of $(T'/T_0)^2$ and corresponding uncertainties derived for 12 falling sphere measurements during the MIDAS/MaCWAVE project (red) and 12 falling sphere measurements accompanying the former turbulence measurements under polar summer conditions (black). After *Rapp et al.* [2004].

difference in $(T'/T_0)^2$. These considerations imply that the larger gravity wave amplitudes during MIDAS/MaCWAVE are a direct consequence of differences in the local stratification as compared to previous years.

Winds

Turbulence generation induces drag, which influences the wind system as briefly described in section 1 (see Eqq. 1.1, 1.4). Therefore, it might be reflected in accompanying wind measurements. Here we further continue our investigation by considering the accompanying falling sphere (see section 4.5.3) wind measurements.

Fig. 6.13 presents two mean altitude profiles of the falling sphere zonal wind measurements. One represents the MIDAS/MaCWAVE soundings (red), and the other shows the "typical" mean measured during other years (from the same location). A distinct feature to see from this plot is the reduced altitude of the mesospheric zonal wind maximum in MIDAS/MaCWAVE data compared to the former soundings (red vs blue).

We further compare the "normal" mean winds with the mean MIDAS/MaCWAVE wind profiles obtained from other, independent measurements with the ALOMAR MF radar [*Singer et al.*, 2005], in Fig. 6.14. One sees that the radar measurements show the same differences as the FS wind measurements. That is, both the zonal wind maximum and the wind reversal in the upper mesosphere are shifted to lower altitudes (i.e. by about 5 km). The meridional winds measured during this campaign shown in the right panel of Fig. 6.14 also exhibit significant differences. Specifically, the meridional wind (in the altitude range between ~80 and 90 km) is significantly reduced during the year 2002 as compared to other years. This is consistent with the temperature measurements that imply a weaker vertical motion (see section 6.1.2); therefore, through the continuity (as described in section 1.2.1) it must imply weaker meridional wind (see Eq. 1.3).

PMSE

The next piece of experimental evidence that the year 2002 was different from the other years comes from the statistics of PMSE observations, conducted with the ALOMAR VHF radar since 1999. Fig. 6.15 shows the PMSE occurrence rate as a function of the day of year

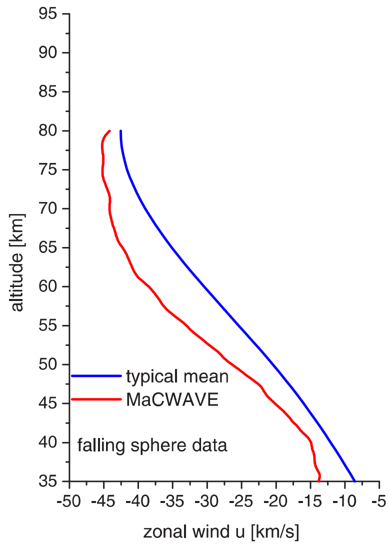

Figure 6.13: Mean falling sphere wind measurements show enhanced zonal winds below ~80 km and a reduced altitude of the zonal wind maximum. After *Goldberg et al.* [2004].

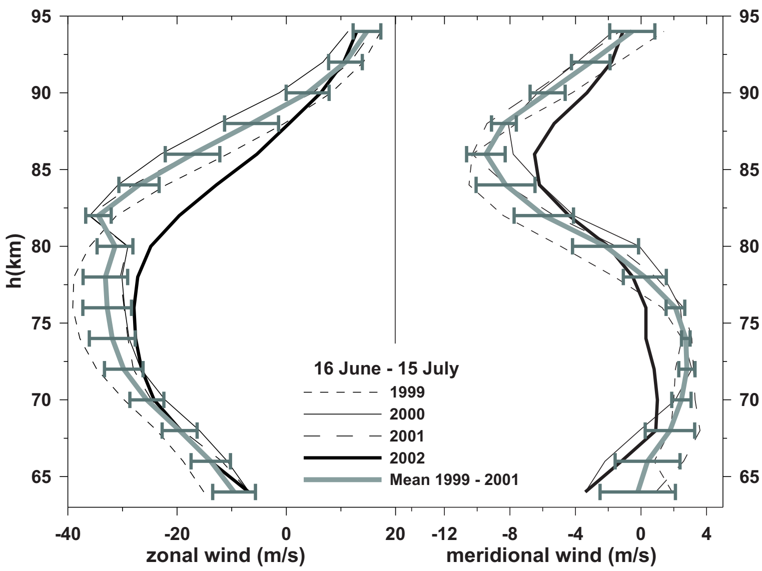

Figure 6.14: MIDAS/MaCWAVE mean radar wind measurements. Zonal winds (left panel) are shifted to the right of the "normal" state, and the altitude of the zonal wind maximum is reduced. Meridional winds (right panel) are weakened compare to the other years. After *Singer et al.* [2005].

[*Goldberg et al.*, 2004]. It is seen that in 2002 PMSE started to occur later than usual. In addition, the entire level of the occurrence rate in 2002 is lower than during the other years. The variability of the 2002 year profile is also larger than during the other years. According to our current understanding of PMSE [*Rapp and Lübken*, 2004] they require low temperatures (below the frost point for water ice) to allow for ice formation at around the mesopause region. Hence, the PMSE observations imply that the mesopause region in 2002 was warmer than in previous years, which is consistent with the temperature observations shown in Fig. 6.2(b) and 6.3(b).

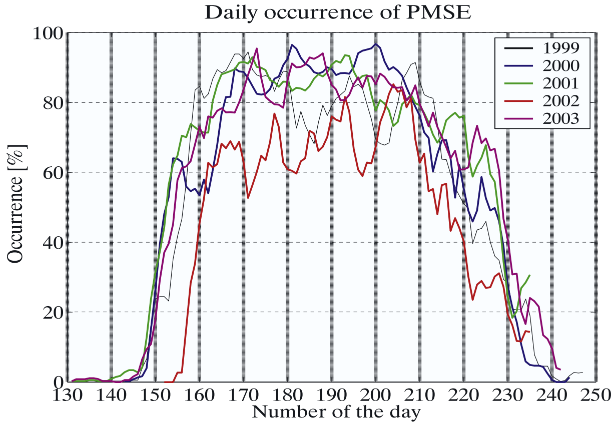

Figure 6.15: PMSE occurrence rate at Andøya, 69 °N for the years 1999-2003. After *Goldberg et al.* [2004].

6.1.5 Interpretation

With all this experimental evidence of the difference in the state of the MLT region during the summer of 2002 compared to the previous years, we can interpret all observed signatures as follows.

Guided by *Fritts* [2003] we sketch the principal understanding of the interplay among gravity wave saturation, momentum deposition, and its feedback on the zonal wind profile (Fig. 6.16). Fig. 6.16 illustrates that in the absence of gravity wave dissipation in the mesopause region, the

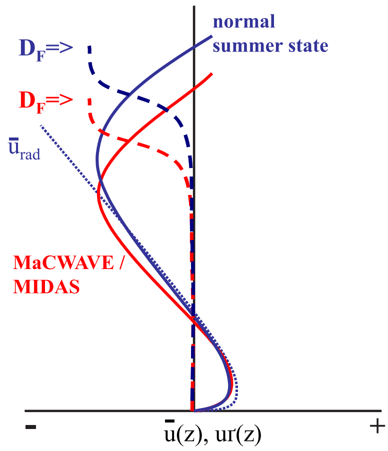

Figure 6.16: Schematic demonstrating the effect of GW breaking at lower altitudes. The dotted line shows the zonal wind as calculated from the radiative equilibrium. The dashed lines schematically show GW amplitude as it growth with height. When waves reach their breaking level, they become unstable and break. This produces wave drag D_F, which bends the wind profile to that shown by the solid line. The blue curves describe the normal summer state. The red curves demonstrate the MIDAS/MaCWAVE conditions. After *Fritts* [2003] and *Rapp et al.* [2004].

westwardly directed zonal wind should grow monotonically with increasing altitude (schematically shown by the blue dotted line); however, the amplitudes of upwardly propagating gravity waves (schematically shown by the blue dashed line) increase due to the density decrease of the atmosphere until they finally reach the altitude level at which the waves become unstable (either statically or dynamically) and break, thereby producing turbulence. This wave dissipation leads to a non-zero momentum flux divergence (or wave drag), D_F, due to the gravity wave and, hence, to a decelerated zonal wind, since $D_F \propto [-1/\rho][d(\rho\ \overline{u'w'})/dz]$, where ρ is the mass density and u' and w' are the gravity wave amplitudes of the zonal and vertical wind component (see also section 1.2, Eq. 1.1). This deceleration ultimately leads to a zonal wind reversal at an altitude near the mesopause.

Therefore, as described above, the differences in the mean stratification (described by the buoyancy frequency, ω_B) lead to larger gravity wave amplitudes (schematically shown in Fig. 6.16 by the red dashed line). Due to their larger amplitudes, the waves reach their breaking level at lower altitudes and produce turbulence at lower altitudes than normal. This wave dissipation then creates a wave drag at lower altitudes, hence leading to the lower altitude of the mesospheric zonal wind maximum (Fig. 6.13).

We note that this sequential explanation of the cause and effect might represent too simplified picture of the situation, since, for example, the altered mean stratification is itself a consequence of the altered gravity wave activity. Hence, it is rather impossible to conclude which property of the atmosphere changed first and then led to all subsequent changes.

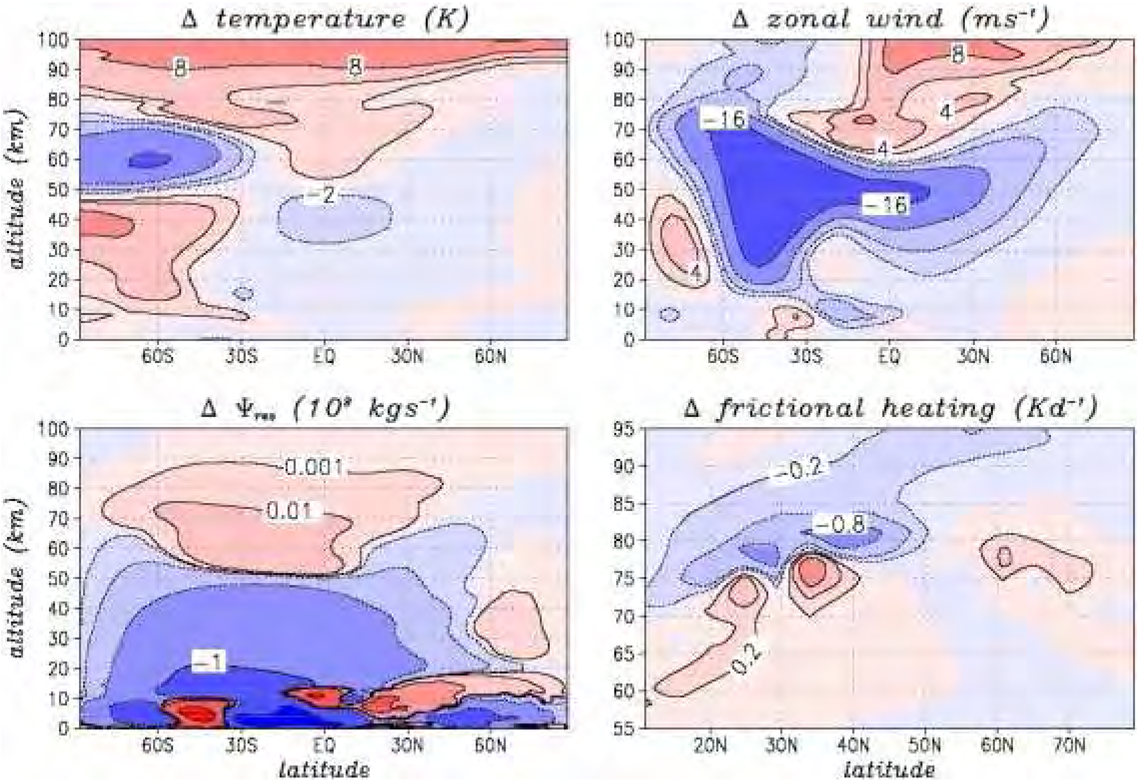

Figure 6.17: Zonal-mean climatological differences: *2002* minus *normal*. (a) Temperature difference. (b) Zonal wind difference. (c) Anomaly of the residual mass stream function. (d) Frictional heating signal. Positive and negative values are indicated by red and blue colors respectively. After *Becker et al.* [2004].

A possible explanation of this peculiar situation is presented in *Becker et al.* [2004], however. These authors examined the global effects of the unusually high Rossby wave activity in austral winter 2002 [see, e.g., observations by *Baldwin et al.*, 2003] using an idealized general circulation model and focusing on the modulation of gravity wave saturation via the altered mean winds in the mesosphere and lower thermosphere. *Becker et al.* [2004] utilized the

Kühlungsborn Mechanistic general circulation model (KMCM) [see e.g. *Becker and Schmitz*, 2001]. KMCM is an idealized general circulation model which explicitly resolves synoptic and planetary waves and where internal gravity waves are parameterized on the basis of Lindzen's saturation concept [*Lindzen*, 1981]. A possible mechanism of how planetary wave forcing in the winter troposphere can affect the summer mesopause region has been described in *Becker and Schmitz* [2003]. For the year 2002, the authors used the mechanism mentioned above [*Becker and Schmitz*, 2003] and a stronger Rossby-wave forcing in the winter troposphere. This leads to enhanced tropical upwelling and a stronger residual circulation in both the winter and summer stratosphere, accompanied by weaker westerlies in winter and stronger easterlies in summer. In the summer MLT the zonal wind becomes more westerly, which is consistent with a downward shift in gravity wave saturation. This reduces the gravity wave-driven residual circulation, giving rise to higher temperatures above about 80 km and some cooling below. These anomalies of mean winds, temperature, and wave dissipation, derived from the model calculations are presented in Fig 6.17. One can see that the model results qualitatively agree with the observational results presented in the previous section.

6.1.6 MIDAS/MaCWAVE summary

All the different and independent measurements conducted during the MIDAS/MaCWAVE sounding rocket campaign in summer 2002 showed results that deviate from many previous observations. When these results are interpreted, they appear to be consistent with each other in the context of our current understanding of gravity wave – mean flow interaction. Moreover, features locally observed in the northern polar latitudes were successfully connected to the global scale processes and ultimately to the local features detected in the southern hemisphere.

The geophysical implications of the results described above are that they gave a comprehensive and consistent set of evidence of the coupling between the small scale processes (turbulence) in the MLT region and larger-scale motions (gravity waves) up to the planetary scales (Rossby waves) and thereby of the interhemispheric coupling.

6.2 ROMA/SvalRak campaign (79 °N)

6.2.1 Campaign overview

In this section a short overview of the ROMA/SvalRak campaign is given, dealing only with the turbulence measurements. A more detailed overview of that comprehensive campaign can be found in *Strelnikov et al.* [2006].

This particular campaign was part of the larger **ROMA** project (**R**ocketborne **O**bservations of the **M**iddle **A**tmosphere). During this project many sounding rockets and a vast number of MET rockets were launched from different northern latitudes during different seasons. As a result, this entire project significantly contributed to in situ measured climatology of the northern hemisphere [see *Müllemann*, 2004, for more details].

From 29 June to 6 July 2003, the European sounding rocket campaign **ROMA-SvalRak** took place at Ny-Ålesund (Spitzbergen, 78.92 °N, 11.93 °E). **SvalRak** is the name of the rocket range located in Ny-Ålesund and operated by the Andøya Rocket Range (ARR). The main scientific aim of that campaign was to study small-scale processes related to neutral and plasma dynamics in the upper mesosphere and lower thermosphere/ionosphere, including turbulence, Polar Mesosphere Summer Echoes (PMSE), and Noctilucent Clouds (NLC). A total of three sounding rockets were launched while ground based measurements were performed with a VHF radar monitoring polar mesosphere summer echoes, a potassium lidar for the detection of noctilucent clouds, and magnetometers that gave evidence for disturbances of the auroral electrojet. The distinctive feature of that campaign is that it is the first summer sounding rocket campaign devoted to the investigation of the mesospheric small scale structuring at such high northern latitudes.

Different instruments onboard the sounding rockets provided simultaneous and high resolution measurements of neutral air density and temperature, electron density and temperature, and positive ion density. The radar observations were continuously conducted throughout the entire campaign period while the potassium lidar was always operated whenever weather conditions permitted.

In Appendix C.1 the most important technical details for this campaign are summarized.

As expected based on previous observations by *Rüster et al.* [2001] at such northern latitudes (79 °N), PMSE were almost continuously observed throughout the entire campaign. In Fig. 6.18 we show the PMSE and NLC observations for all three flights during the ROMA-SvalRak campaign. The vertical red line marks the rocket launch time in each case. The rocket flights are labeled RO-MI-01, RO-MI-02, and RO-MI-03, respectively. The grey scale contours in Fig. 6.18 show the signal-to-noise ratio (SNR) registered by the SOUSY radar [**?**] during the days of the rocket launches: i.e., July 1st, 4th, and 6th, 2003. The thick blue contour lines show the NLC observed by the IAP lidar [*Höffner et al.*, 2003]. The shown contour lines indicate the volume backscatter coefficient (BSC) of $2 \cdot 10^{-10}/(m \cdot sr)$ at a wavelength of 770 nm.

Unfortunately, during all three flights the payloads experienced a coning (tumbling), which impaired the data quality. This makes it difficult to derive reliable density and temperature profiles from the CONE measurements for the flights RO-MI-01 and RO-MI-02. This drawback, however, does not corrupt the small-scale analysis, since it primarily influences the large scales ($\sim$ some kilometers). The flight RO-MI-03 was sufficiently stable (angle of attack less then 30°) to derive reliable density and temperature profiles from CONE and also from the CPP measurements.

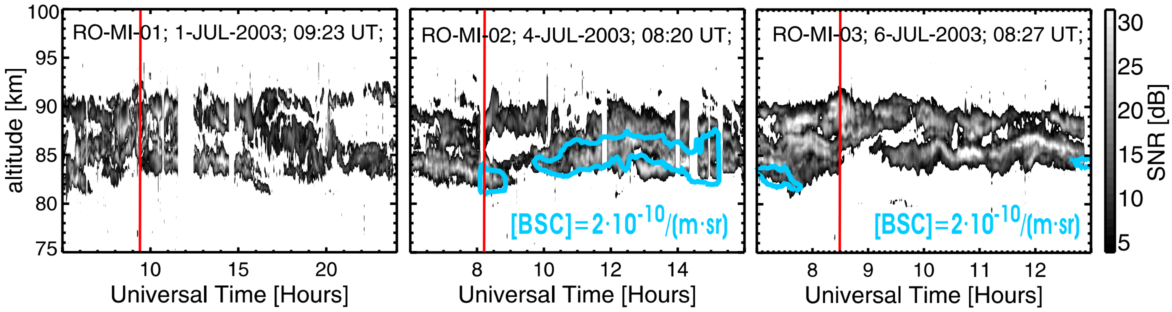

Figure 6.18: PMSE and NLC conditions for the ROMA-SvalRak campaign registered at Longyearbyen (78.20 °N, 15.83 °E). Grey scale contours show the SNR in dB recorded by the SOUSY-Svalbard radar during the days of the rocket launches. The names, dates, and times of launches are indicated in the figure. The time of rocket launch is also marked by the vertical line in all cases. The blue thick contour line shows the NLC registered by the potassium lidar.

6.2.2 Measurements: Background atmosphere

Unlike in the case of the MIDAS/MaCWAVE campaign, no FS measurements were conducted during the ROMA/SvalRak campaign. Hence, the only available in situ measurements of the background state were the absolute measurements onboard the sounding rockets. As mentioned above, successful absolute measurements were obtained during the rocket flight RO-MI-03 which was launched on 6 July at 08:27 UT.

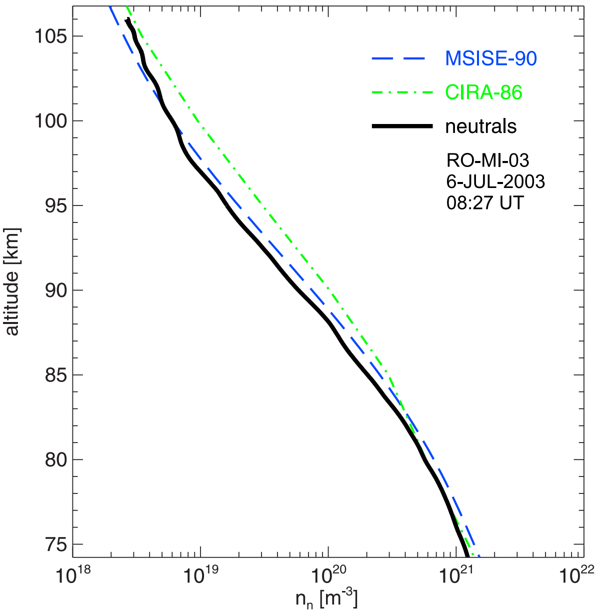

(a) Neutral air density measurements.

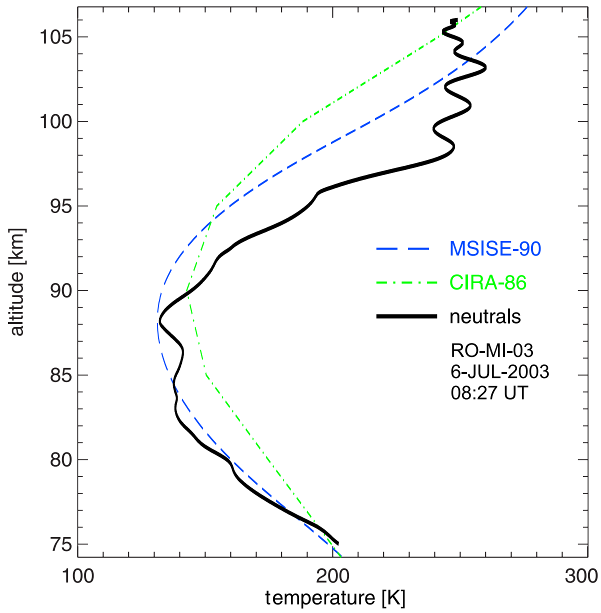

(b) Neutral temperature measurements.

Figure 6.19: In situ measurements of background atmospheric parameters conducted during the flight RO-MI-03 (Ny-Ålesund, 6-JUL-2002, 8:27 UT). Reference profiles: MSISE-90 [*Hedin*, 1991] as dashed and CIRA-86 [*Fleming et al.*, 1988] as dash-dotted.

First, we present the neutral air number density profile measured by the CONE instrument (see Fig. 6.19(a), solid bold line). In Figure 6.19(a) we further show two profiles taken from the

CIRA-86 (COSPAR International Reference Atmosphere, *Fleming et al.* [1988]) and MSISE-90 (Mass Spectrometer Incoherent Scatter, *Hedin* [1991]) reference atmospheres for 79 °N, 11 °S and the time of the rocket launch.

It is clear that the CIRA-86 model density profile practically coincides with the measured density profile in the height range from 75 km up to 82 km. For higher altitudes however, CIRA-86 shows densities that are too large by as much as a factor of 2. This observation generally agrees with the results of earlier comparisons between measured and CIRA-86 number densities at polar latitudes of 69 °N [*Lübken*, 1999; *Rapp et al.*, 2001]. In contrast, the MSISE-90 model density profile closely follows the measured density profile in the entire altitude range.

The neutral air temperature profile derived from the density measurements discussed above is shown in Fig. 6.19(b) by the solid bold profile. It shows a well defined mesopause around 88 km with a temperature of ~130 K. Note that the undulations seen above 97 km are probably the consequence of a strong coning of the rocket payload and may not be considered real atmospheric structures due, for example, to gravity waves. The reference profiles taken from CIRA-86 (dash-dotted line) and MSISE-90 (dashed line) models are also shown in this figure. As one can see, again, the MSISE-90 model is in somewhat better agreement with the in situ measurements than the CIRA-86 model is.

6.2.3 First in situ turbulence measurements at 79° N

Scalograms

In Fig. 6.20, 6.21, and 6.22 we present the wavelet spectrograms of relative neutral density fluctuations derived using Morlet-24 analysis for the flights RO-MI-01, RO-MI-02, and RO-MI-03 respectively.

As before, the power (in units $[\%/s]^2$) is color-coded, as shown by the color bar on the right side. The dark-blue to black colors reflect the noise level of $\sim 10^{-8} - 10^{-9}\ s^{-2}$. White color reflects the highest power, exceeding the largest value shown in the color bar ($10^{-3}\ s^{-2}$).

Similar to the MIDAS/MaCWAVE results (Fig. 6.8, 6.9, and 6.10), there are some common features for rocketborne turbulence measurements. They include sharp, local gradients in both small-scale (10 to 100 meters) and large-scale (100 to ~300 meters) structuring: that is, in both turbulent kinetic energy production and dissipation. Also, the highest activity occurs at around the mesopause region (that is around ~90 km altitude), and the largest variability of the turbulent structures occurs at the small scales. Also, in Fig. 6.20, 6.21, and 6.22 small-scale structuring appears within short time (altitude) intervals, indicating that turbulence activity is confined to narrow layers.

There are, however, some new, specific features. First, the structurings occur down to 70 km altitude, which is not a commonly observed feature at high northern latitudes. Such low-altitude turbulence (below 82 km) was only observed during the MIDAS/MaCWAVE campaign and (as shown in section 6.1) was interpreted as a specific feature of the year 2002. Second, the smallest scales, resolved by the scalograms, extend down only to ~10 meters (Fig. 6.20, 6.21, and 6.22), which is in contrast to the MIDAS/MaCWAVE results (Fig. 6.8, 6.9, and 6.10) where structuring occurs down to the scale of ~6 m. This implies significantly weaker turbulence. Third, the CONE measurements conducted during the flight RO-MI-03 yielded a very quiet spectrum (Fig. 6.22). There is some structuring, but the power values within the large scales (~300 m) do not reach the 10^{-4}-value. Also, the spectra (Fig. 6.22) are rather smooth at all scales, giving evidence of an almost completely non-turbulent MLT region.

One has to mention again that the horizontally organized structuring at ~30 m and ~50 m

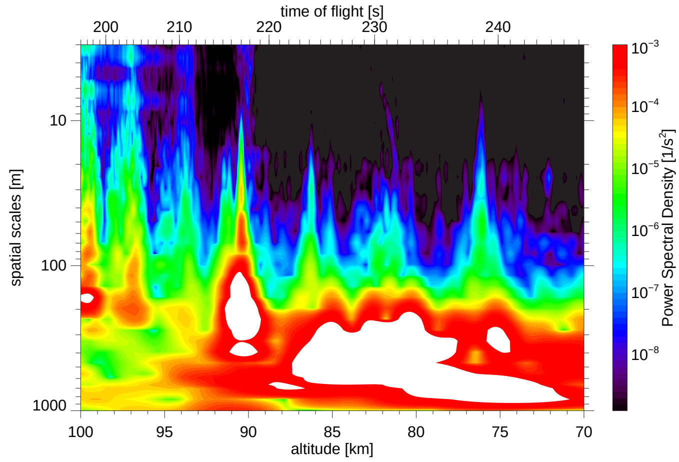

Figure 6.20: Wavelet power spectrum (derived utilizing Morlet-24 wavelet function) of the relative neutral density fluctuations (residuals) measured during the flight RO-MI-01 (Ny-Ålesund, 1-JUL-2003, 9:23 UT).

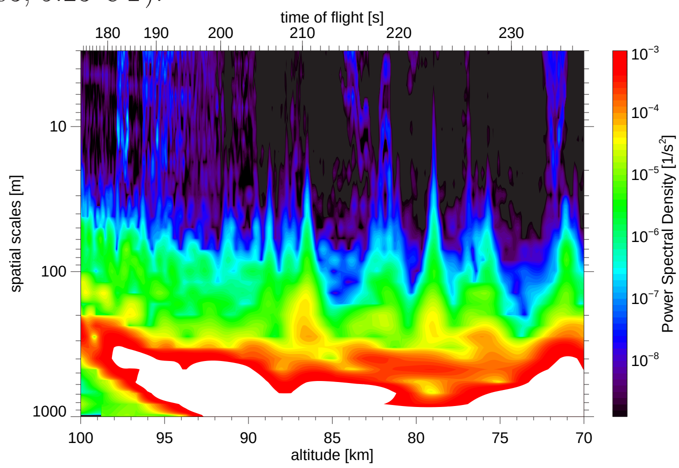

Figure 6.21: The same as 6.20 but for the flight RO-MI-02 (Ny-Ålesund, 4-JUL-2003, 8:20 UT).

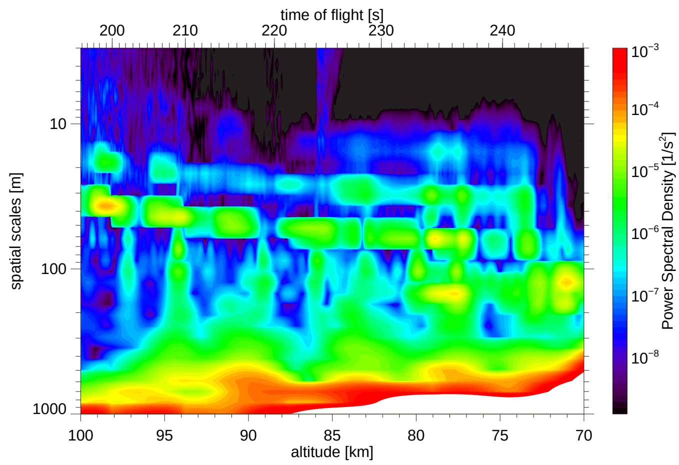

Figure 6.22: The same as 6.20 but for the flight RO-MI-03 (Ny-Ålesund, 6-JUL-2003, 8:27 UT).

are the unfiltered spin harmonics that do not disturb the quantitative analysis.

From these scalograms the energy dissipation rates are also deduced with 100 m altitude resolution.

Dissipation rates

In Fig. 6.23 we present the quantitative results of the turbulence analysis, performed for all three sounding rocket flights during the ROMA/SvalRak campaign.

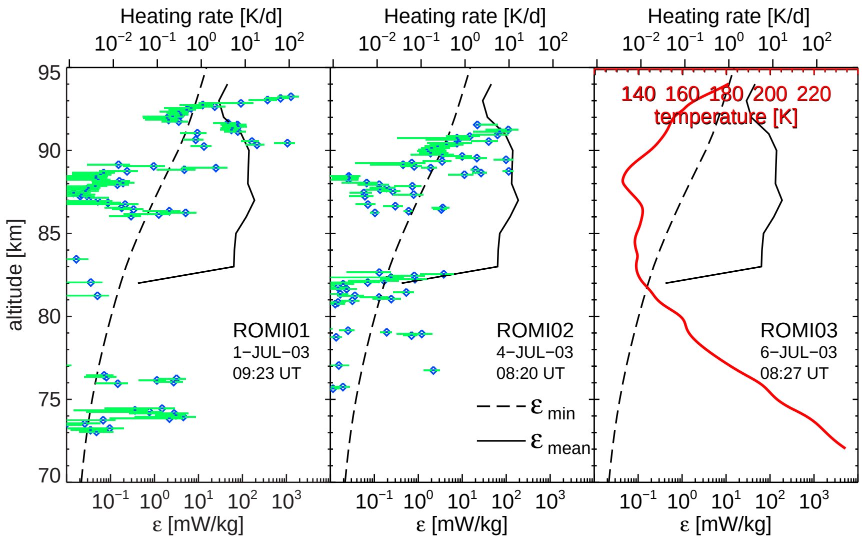

Figure 6.23: Turbulent energy dissipation rates (blue points) with error-bars (in green) measured by the CONE instrument during the ROMA/SvalRak campaign. July 2003.

This is another, more explicit representation of the same turbulence characteristics as described in the previous section. One can now see that most of the ε-values are several orders of magnitude less than the ε_{mean}-reference-profile derived from the in situ measurements by *Lübken et al.* [2002]. Also, the spectral model method does not allow the reliable derivation of any turbulence characteristics for the RO-MI-03 flight.

According to the previous observations by *Rüster et al.* [2001], PMSE are almost always present at such northern latitudes (79°N). Our current understanding of the PMSE (summarized in *Rapp and Lübken* [2004]) implies that at least some turbulence activity should be present in the MLT region. In this context, the case of a non-turbulent summer MLT at high northern latitudes (RO-MI-03 flight) is a surprising experimental fact which deserves a deeper study in future investigations.

6.2.4 69 °N versus 79 °N: Latitudinal variability of turbulence activity

Experimental facts

In this section we compare the results of the in situ turbulence measurements at Andøya, 69 °N, with the results of the first turbulence measurements at a higher (northern) latitude, 79 °N, at Ny-Ålesund, obtained during the ROMA/SvalRak sounding rocket campaign (section 6.2).

The energy dissipation rates derived at 69 °N and 79 °N are presented and discussed in sections 2.5, 6.1, and 6.2 respectively. In Fig. 6.24 we show:

1. The result of turbulence measurements at 69 °N from *Lübken et al.* [2002] (normal case, mean over 19 flights).

2. The result of turbulence measurements at 69 °N during the MIDAS/MaCWAVE campaign (special case, mean over three flights).

3. The result of turbulence measurements at 79 °N during the ROMA/SvalRak campaign (mean over three flights).

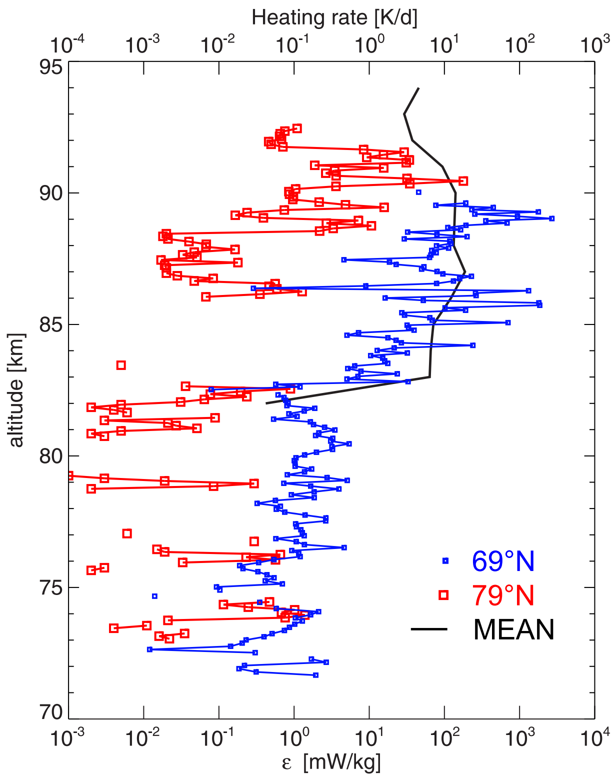

Figure 6.24: The results of the in situ turbulence measurements at 69 °N and 79 °N. The bold black line shows the normal mean state at Andøya, 69 °N [*Lübken et al.*, 2002]. The blue profile is the mean over three rocket flights during MIDAS/MaCWAVE (Andøya, 69 °N). The red profile is the mean over three rocket flights conducted during ROMA/SvalRak (Ny-Ålesund, 79 °N). After *Strelnikov et al.* [2006].

The first feature seen from this comparison is that at 79 °N turbulence is weaker than at 69 °N. The second feature is that at 79 °N turbulence was detected in a broad altitude range, which is similar to the special case of the MIDAS/MaCWAVE campaign but different from the normal mean state at 69 °N; however, in the case of the MIDAS/MaCWAVE, the broad altitude range is filled with the turbulent structures almost continuously, whereas at 79 °N we detected only a few narrow turbulence layers.

The measurement's statistics at 79 °N is, of course, poor for a meaningful statistical analysis of the in situ measured turbulence dissipation rates. Nevertheless, we take our observational results as a motivation to compare with predictions of a general circulation model and investigate the physical reason for the theoretically predicted latitudinal structure.

Interpretation

As highlighted in the previous sections (see also chapter 2), one of the major sources of mesospheric turbulence at high northern latitudes is the breakdown of gravity waves (GW).

We briefly consider the *Lindzen* [1981] type description of the wave−mean flow interaction. The Lindzen parametrization infers an altitude where the vertically propagating gravity waves start to break and thereby produce turbulence [see e.g. *Holton*, 1982, Eq. 21]:

$$z_b = 3H \ln \left(\frac{(\overline{u} - c)^{3/2}(u_0 - c)^{1/2}k}{B\omega_B} \right) \tag{6.1}$$

where the parameters B, k, and c are the amplitude, zonal wavenumber, and phase speed of the considered gravity wave, respectively. H is the scale height and ω_B is the Brunt-Väisälä (buoyancy) frequency. $\overline{u}(z)$ is the mean horizontal wind profile and $u_0 = \overline{u}(z_0)$ is the mean horizontal wind at the altitude z_0 of the GW generation. The GW-breaking produces turbulence as described in sections 1.2 and 6.1.3. The strength of turbulence can be described in terms of the eddy-diffusion coefficient, K, as described in section 2.3. The eddy-diffusivity resulting from the GW-breaking is given by [see e.g. *Lindzen*, 1981; *Holton*, 1982]:

$$K = \frac{k(c - \overline{u})^3}{2\omega_B} \left(\frac{c - \overline{u}}{H} + 3\frac{d\overline{u}}{dz} \right) \tag{6.2}$$

It is seen from Eqq. 6.1 and 6.2 that both the lowest altitude of turbulence generation, z_b, and the strength of turbulence, K, depend on the mean zonal wind, $\overline{u}$, and the GW phase velocity, c.

The GW phase velocity, c, lies most likely in the range from zero to the tropospheric flow speeds (see, e.g., Fig. 1.2(b)), for the GWs generated in the troposphere [*Lindzen*, 1981]. Also, the tropospheric jet (u_T in Fig. 6.25(a)) will filter the phase speed of the vertically propagating gravity waves such that only gravity waves with $c > u_T$ will path through to the mesospheric heights [see e.g. *Lindzen*, 1981, for more detailed explanation]. This implies that the zonal wind profile defines the heights and strength of the GW-induced mesospheric turbulence.

The *Lindzen* [1981] parametrization of the gravity wave saturation was implemented in the Kühlungsborn Mechanistic general Circulation Model (KMCM) by *Becker* [2004]. Fig. 6.25 shows the results of calculations using the KMCM model for summer conditions in the northern hemisphere. Two geographical latitudes of 45 °N and 80 °N were chosen to demonstrate the principles more obviously. Fig. 6.25(a) shows two profiles of zonal wind derived for 45 °N (solid) and 80 °N (dashed). The mid-latitude profile (solid line) when compared to the high-latitude profile (dashed line) reveals the higher $\overline{u}$-values in the mesosphere and implies stronger wave filtering by the background wind in the troposphere (which results in the higher c-values). That, in turn, implies that the altitude of the initial GW-braking, z_b, marked by the horizontal lines in Fig. 6.25 (and, therefore, lowest turbulence) will be reduced (Eq. 6.1) and that the turbulence strength, ε, will be smaller at high latitudes (Fig.6.25(b)).

Another property of the atmosphere underlying the fact that the turbulence weakens when moving to the north is that atmospheric density becomes higher. In other words, the same energy when dissipating per smaller mass results in a weaker energy dissipation rate, ε.

The results of the KMCM calculations by *Becker* [2004] over the entire latitudinal range from the southern to the north pole are displayed in Fig. 6.26. It shows the same behavior as qualitatively described above. That is, in the northern hemisphere in summer when following from middle to high latitudes, mesospheric turbulence become weaker, and the lower limit of turbulence generation slides down to the lower altitudes.

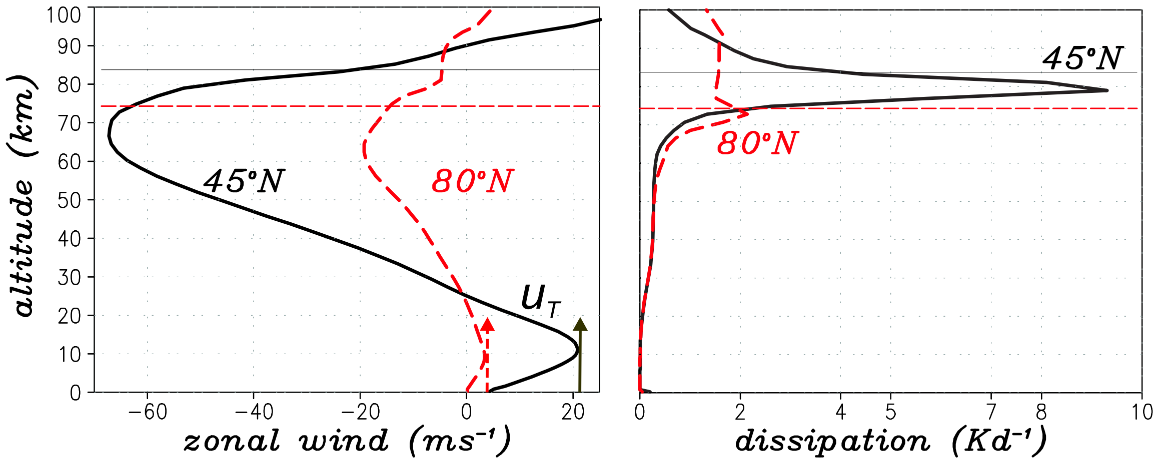

(a) Mean zonal wind altitude-profiles, $\overline{u}(z)$. Positive wind is eastwardly directed.

(b) Latitudinal variability of the dissipation field, ε, in K/day.

Figure 6.25: Latitudinal distribution of meteorological parameters derived from the GCM by *Becker* [2004] for July in the northern hemisphere. The solid and dashed profiles represent the latitudes of 45 °N and 80 °N respectively. The vertical arrows (marked by u_T, see text) show the minimum phase velocity of gravity waves which can propagate upwards without reaching the critical level ($c = \overline{u}$). The horizontal lines show the breaking level of gravity waves as derived from the model calculations. Courtesy of E. Becker.

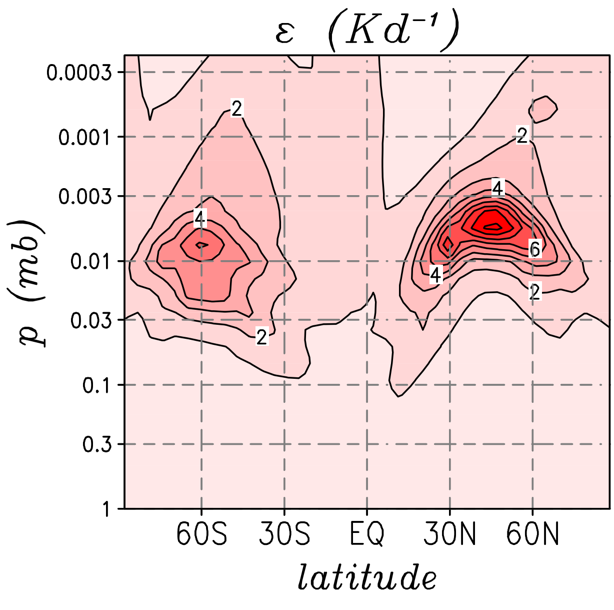

Figure 6.26: Latitudinal variability of the turbulence energy dissipation rates [*Becker*, 2004]

ROMA/SvalRak summary

Another novelty of this work is that it presents the first high-resolution in situ measurements of neutral air density, temperature, and turbulence conducted at northern latitudes as high as 79 °N in summer. The turbulence field reflected by our measurements showed some common properties for all the MLT rocket soundings and also some prominent differences from our previous observations at 79 °N. The challenging feature observed during this campaign is the non-turbulent MLT during the flight RO-MI-03. This feature can probably be explained after we finish developing analysis technique of the so-called "fossil" turbulence. This technique aims to gain insight into the state of development/decay: that is, to estimate the time of life of the turbulent structures (see chapter 8).

The next novelty of this work is that it presents the first comparison of in situ measurements of neutral air turbulence conducted at high northern latitudes at 69 °N and 79 °N in summer. The turbulence field reflected by our measurements showed some common properties for all the MLT rocket soundings and also some features that are specific for the 79 °N. This is discussed in section 6.2. The latitudinal dependence of the turbulence field reflected by measurements presented above is the first experimental check of our current understanding of the high-latitude MLT dynamics. We have shown that the numerical simulations can qualitatively reproduce the measurement results.

Chapter 7

Geophysical results: Plasma

In this chapter we discuss phenomena related to plasma dynamics of the high-latitude E-region observed during the ROMA/SvalRak campaign. A general overview of this campaign is given by *Strelnikov et al.* [2006] and in section 6.2.1 of this manuscript. First, we discuss in depth the results of two rocket flights: RO-MI-01 and RO-MI-03. Then we discuss potential implications of our findings for the MLT dynamics in section 7.2.6.

7.1 Background ionosphere

As for the neutral dynamical studies (chapter 6), we start with in situ measurements that describe the background state of the ionosphere: i.e., profiles, gradients, etc. The absolute values of the background parameters were only successfully measured during the flight RO-MI-03.

Absolute plasma density

In Fig. 7.1 we present the altitude profiles of the positive ion (black solid line) and electron number density (symbols) derived from measurements with the PIP instrument (section 4.5.2) and the radio wave propagation experiment (section 4.5.3), respectively. Electron measurements with the CONE instrument were unfortunately not available during this flight due to a malfunction of this part of the instrument (see appendix C.2). Note that the PIP current has been converted to <u>absolute</u> number densities by normalizing it to the result of the radio wave propagation experiment at an altitude of about 97 km. Triangles represent the electron density derived by the differential absorbtion technique (see section 4.5.3) of a 3.8 MHz frequency radio wave. The square represents the electron number density derived from the total reflection of a radio wave at a frequency of 1.3 MHz. Total reflection occurs when the frequency of an incident wave equals the plasma frequency f_p which is a unique function of the electron number density n_e: $f_p = 8.98 \cdot 10^3 \sqrt{n_e}$ where n_e is given in cm^{-3}.

Absolute electron temperature

In the frame of this campaign there were two different experiments that aimed to measure temperature onboard the sounding rockets (see appendix C.2). These are the CONE and CPP temperature measurements. The neutral air temperature and density derived from the CONE measurements were discussed in section 6.2.2 and are shown as a solid bold line in Fig. 7.2. The CPP instrument (see section 4.5.3) was first successfully operating during the flight RO-MI-03 [*Svenes et al.*, 2005]. This yielded an electron temperature profile in the

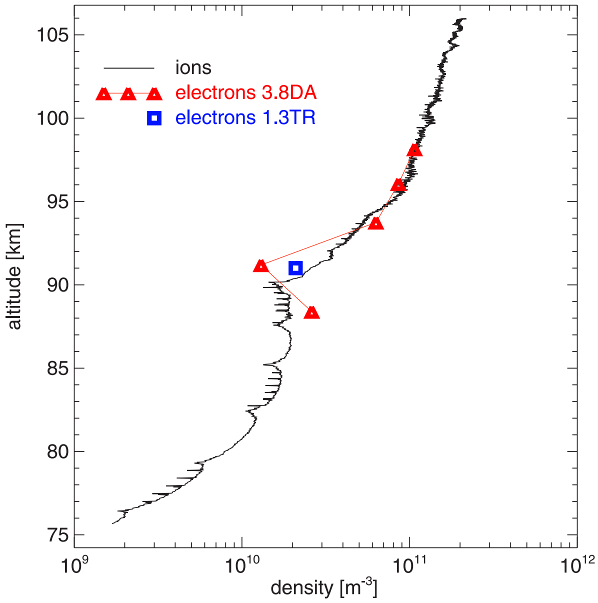

Figure 7.1: Positive ion number densities (black solid line) measured with the PIP instrument during the flight RO-MI-03 on 6 July 2003. Triangles represent the electron density derived by the differential absorption technique (see section 4.5.3) of a 3.8 MHz frequency radio wave (notation in the plot: 3.8DA). The square represents the electron number density derived from the total reflection of a radio wave of a frequency of 1.3 MHz (see text; notation in the plot: 1.3TR). Note that the PIP current has been converted to <u>absolute</u> number densities by normalizing it to the result of the radio wave propagation experiment at an altitude of about 97 km.

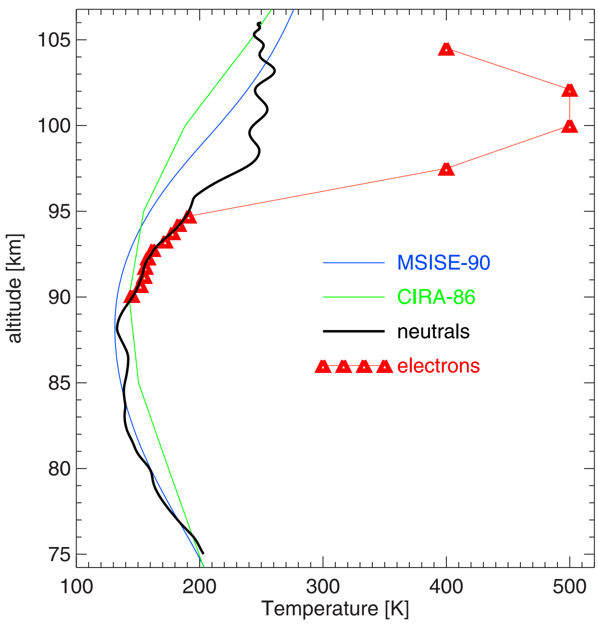

Figure 7.2: Temperature measurements conducted during the flight RO-MI-03 (Ny-Ålesund, 6-JUL-2002, 8:27 UT). Black bold profile: neutral temperature measurements with the CONE. Red profile: electron temperature measurements with the CPP.

altitude range between ~106 km and ~90 km.

In Fig. 7.2 we show the electron temperature measurements (triangles) conducted with the CPP instrument during the ascent part of the rocket trajectory. The electron temperature is shown in the altitude range from 90 km up to the apogee of the rocket trajectory of 106.1 km. Below 90 km temperatures cannot be derived at present with sufficient reliability because of plasma-aerodynamical effects and too low electron number densities [see *Svenes et al.*, 2005, for more details]. Between 90 and 95 km the electron temperatures are in agreement with the measured neutral temperatures. In the height range from 95 km up to 102 km, the electron temperature significantly exceeds the neutral air temperature and reaches values as large as 500 K. Higher up, the electron temperature is decreasing to 400 K at 105 km on the upleg of the rocket flight. On the downleg, still equal to 400 K at 105 km altitude, the electron temperature falls and again approaches the neutral air temperature at about 102 km altitude (not shown here). Starting from 102 km and farther down, the electron temperature measured during the descending part of the rocket trajectory equals the measured neutral temperature and is not shown in the plot.

The comparison of the neutral and electron temperatures, both measured in situ in the same volume, has never been done before and is a new experimental result [*Svenes et al.*, 2005; *Strelnikov et al.*, 2007].

The enhanced electron temperatures observed between 94 and 106 km on the ascent of the rocket trajectory are clearly indicative of a two-stream plasma instability that has the potential to heat the electron gas by as much as ~3000 K [e.g. *St.-Maurice et al.*, 1999]. We will come back to this issue and discuss the type of instability we observed in the next sections.

Summarizing this section, we have measured the neutral and plasma (positive ion and electron) number densities and neutral and electron temperatures, which makes it possible to precisely derive collision frequencies ν_i and ν_e and therefore ionospheric conductivity (see chapter 3). Among these measurements, the enhanced electron temperatures above ~95 km observed on the ascent of the rocket trajectory and its relaxation back to temperatures identical to the neutral temperature after the passing the apogee is a striking feature that will be analyzed in section 7.2.3.

7.2 Small scale plasma irregularities.

The ion density profile shown in Fig. 7.1 was measured with a time resolution on the order of milliseconds resulting in an altitude resolution of tens of centimeters (see section 4.5). Using wavelet analysis, this finely structured ion density profile was next examined with respect to its spectral content (see section 5.3 and *Strelnikov et al.*, 2003). First, we derive relative ion density fluctuations (also called residuals) using a reference profile n_i^{ref}:

$$r_i(t) = \frac{n_i(t) - n_i^{ref}}{n_i^{ref}}. \tag{7.1}$$

The reference profile was derived from a moving average of the measured time series over ~5 rocket spin periods (~5 Hz). Then a bandstop filter was applied to the derived residuals to filter out the spin frequency and its first harmonic. Resulting relative ion density fluctuations are shown in the upper panel of the Fig. 7.3 as a function of altitude or time of the rocket flight.

Next we applied the wavelet transform to these relative ion density fluctuations using the Morlet-24 wavelet function which results in an altitude resolution of $\sim 5l$, where l is the spatial scale (see section 5.3 for more details). That is, when following a structure in the scalogram (Fig. 7.3) at, for example, 10 m along the abscissa, the smallest length scale of the irregularities resolved by the analysis is ~50 m. In the lower panel of Fig. 7.3 we show the derived wavelet spectrogram (i.e. power spectral density as a function of both spatial scales and time/altitude) of the relative ion density fluctuations. The noise level of two percent residuals corresponds here to the blue color or power spectral densities on the order of 10^{-7} s^{-2}. The largest power values shown in this spectrogram correspond to the red color or power spectral densities on the order of 10^{-2} s^{-2}.

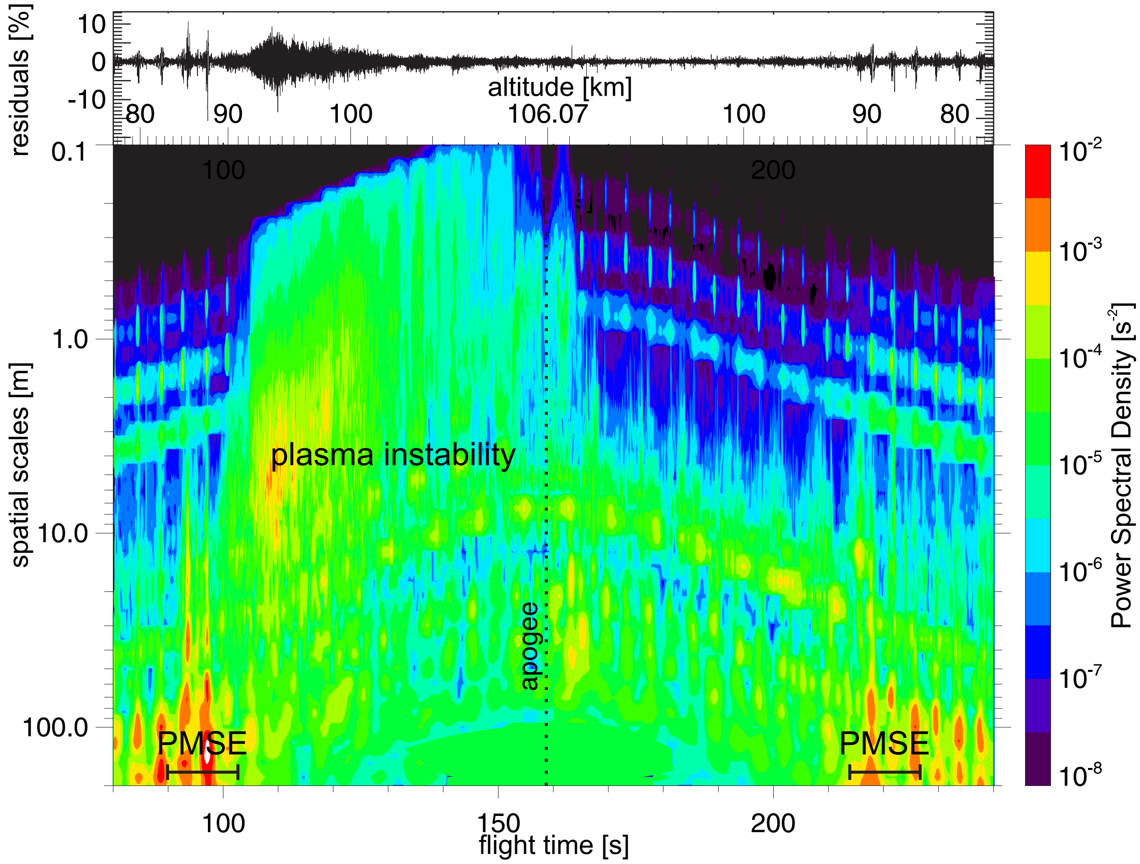

Figure 7.3: Upper panel: Relative ion density fluctuations (≡ residuals) measured with the PIP instrument during the flight RO-MI-03 on 6 July, 08:27 UT (see text). Lower Panel: Wavelet power spectrum of the residuals shown in the upper panel. The apogee of the rocket trajectory of 106.1 km is marked by the vertical dotted line. The PMSE altitude regions for upleg and downleg are marked by the two bold black bars and are labeled "PMSE." The altitude region where very small-scale positive ion structures were observed is marked by the shaded background in the upper panel and labeled in the lower panel as "Plasma instability." The deciphering of the color code is shown as a color bar on the right side.

This complicated figure reveals a wealth of features that we subsequently discuss in the following subsections.

7.2.1 PMSE

The first feature we want to discuss here is the enhanced power seen in the spectrogram (Fig. 7.3) between 90 and 105 seconds of the rocket flight time, which starts from the largest scales resolved in this spectrogram and extends down to ~1 m. A similar power increase also appears on the descending part of the rocket trajectory between approximately 212 and 228 seconds of the rocket flight time. These time intervals both correspond to an altitude range from ~84 km to 92 km. This is the altitude range where PMSEs are commonly observed at polar latitudes [**?**].

The scalogram within this time/altitude interval shows features similar to that observed in the small-scale neutral structures discussed in chapter 6. The neutral density irregularities were created by the turbulent motions. As discussed in section 1.2, the turbulent processes must also affect the plasma density at heights of the D-region.

In order to check whether the observed enhancement of spectral power at altitudes between 84 and 92 km is indeed in situ evidence of polar mesosphere summer echoes, we now consider the PMSE observations obtained with the SOUSY-Svalbard radar around the time of the in situ observations. In Fig. 7.4 we show a contour plot of the PMSE measurements carried out with the SOUSY radar between 7:00 and 13:00 UT. Note that we consider such an extended time interval of PMSE observations in order to account for the horizontal distance of ~100 km between the radar location and the rocket launch site (see section 6.2.1). As one can see, the SOUSY-Svalbard radar detected a strong, often double-layered PMSE at altitudes between 82 and 92 km during the entire period considered here. In this figure we compare the PMSE observations to our small scale plasma density measurements: According to, e.g., **?**, the power P observed by the radar is directly proportional to the power spectral density (PSD) of the absolute electron number density fluctuations (ΔN_e) at the radar Bragg scale λ_{Bragg} (i.e., the radar half wavelength):

$$P \propto PSD(\Delta N_e, k_{Bragg}) \tag{7.2}$$

where $k_{Bragg} = 2\pi/\lambda_{Bragg}$ is the wavenumber corresponding to the radar Bragg scale, which is 2.8 m in the case of the SOUSY radar.

As mentioned above (see also appendix C.2), high-resolution measurements of the electron number density that could be used to determine $PSD(\Delta N_e, k_{Bragg})$ are not available because the electron probe of the CONE instrument failed; however, it was shown by *Rapp and Lübken* [2003] and **?** that fluctuations of electrons, positive ions, and charged ice-aerosol particles that constitute the plasma at PMSE altitudes are coupled through multipolar diffusion processes. Hence, $PSD(\Delta N_e, k_{Bragg})$ and $PSD(\Delta N_i, k_{Bragg})$ are proportional to each other. This means that instead of directly comparing the radar signal to the amplitude of the electron number density fluctuations at the Bragg scale, we may also compare it to the corresponding positive ion density fluctuations [for further proof of this concept see also **?**, their Figure 5].

Profiles of $PSD(\Delta N_i, k_{Bragg})$ for both upleg and downleg of the rocket trajectory are overplotted on the PMSE display shown in Fig. 7.4 as the red and blue lines, respectively. As one can see, the in situ as well as the radar measurements show a well defined multilayer structure between 84 and 92 km altitude. In this altitude range the maximum backscattered power (contour plot) and $PSD(\Delta N_i, k_{Bragg})$, shown by the color profiles, both exceed the background signal by ~30 dB.

We also observed power enhancements at the SOUSY radar Bragg scale (~2.8 m) in ion density fluctuations within the PMSE altitudes measured during the flight RO-MI-01 [*Strelnikov et al.*, 2006]. Also, the electron fluctuations successfully measured during the flight RO-MI-01 show the same behavior. This is shown in Fig. 7.6 and 7.7, where we present the wavelet power spectrum of the relative ion and electron density fluctuations measured during this flight, respectively. In Fig. 7.5 we show the corresponding profiles of $PSD(\Delta N_i, k_{Bragg})$ and $PSD(\Delta N_e, k_{Bragg})$.

All these analyses show a similar power enhancement at the PMSE altitudes ($85 - 90$ km). Moreover, the structuring within these heights resembles that observed in the neutral density

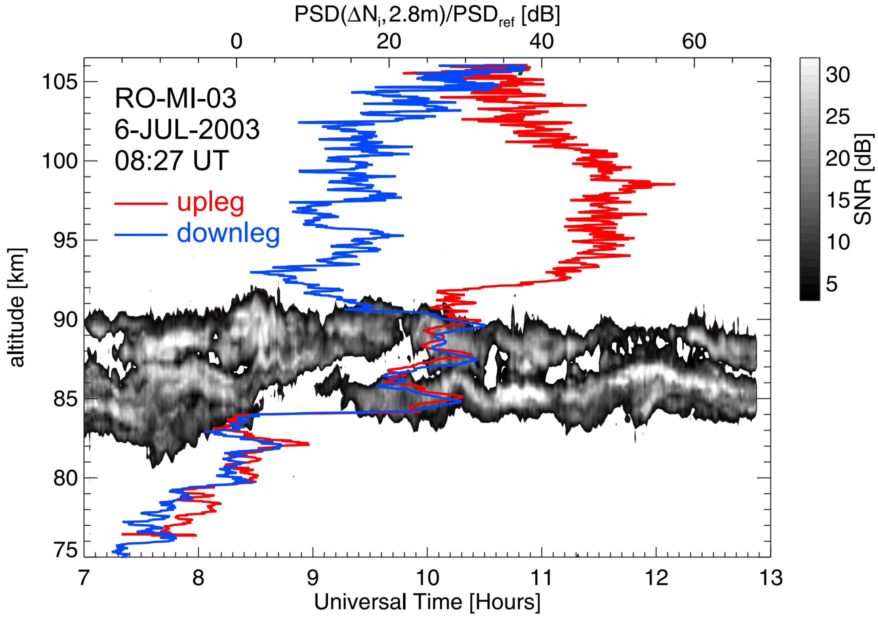

Figure 7.4: Gray scale contour plot of PMSE-SNR recorded by the SOUSY radar, which is located at Logyearbyen (78 °N, 16 °E). The red line represents the power spectral density (PSD) of positive ion density fluctuations at the radar Bragg scale of 2.8 m (see text). The corresponding PSD profile from the downleg part of the rocket trajectory is shown as a blue line. The lower abscissa shows the time of the radar measurements (contours) in UTC. The upper abscissa represents the values of the shown PSD profiles in dB. The color bar on right side decodes the contours into the power values in dB.

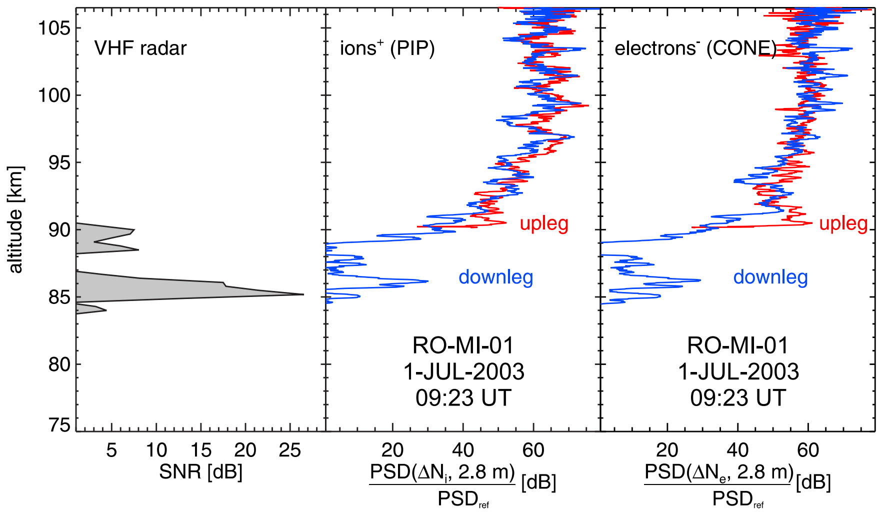

Figure 7.5: In situ measurements of small-scale plasma irregularities compared to the observations by means of remote sensing techniques. Grey shaded areas represent the mean of the PMSE measurements carried out with the SOUSY radar around the flight RO-MI-01 (1-JULY-2003, 09:23 UT). Four profiles are the power spectral densities (PSD) of the absolute ion (middle panel) and electron (right panel) number density fluctuations, ΔN_i and ΔN_e respectively, at the Bragg scale of the SOUSY radar (λ_{Bragg}=2.8 m), expressed in dB. Red profiles correspond to the upleg and blue to the downleg. After *Strelnikov et al.* [2006]

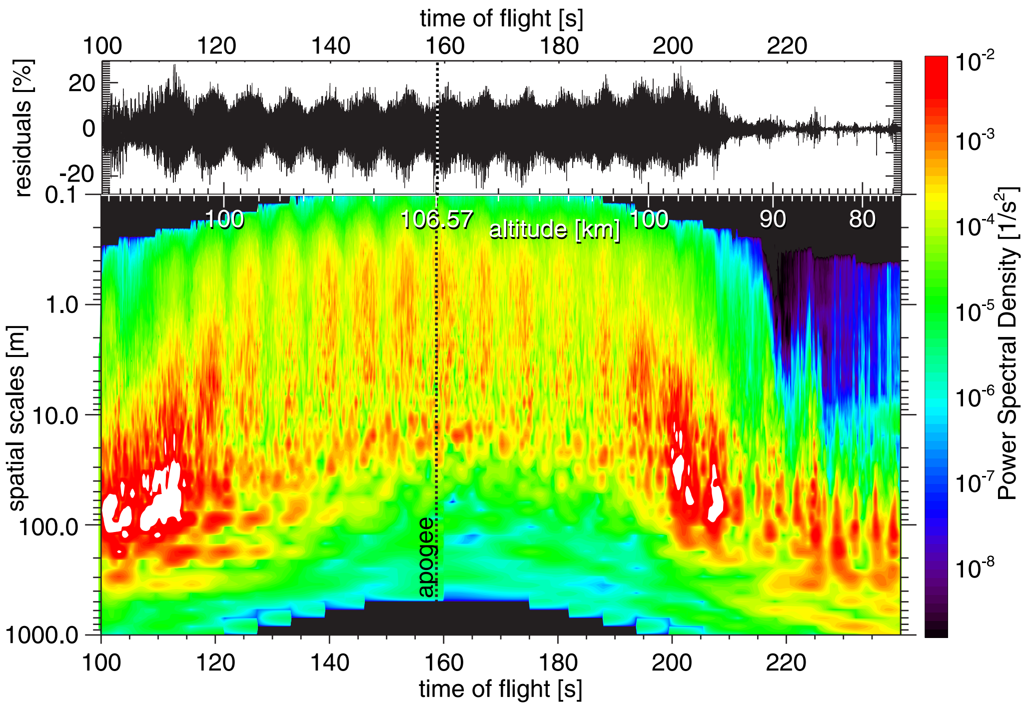

Figure 7.6: Relative ion density fluctuations (upper panel) and its scalogram (lower panel) measured during the flight RO-MI-01 (1-JULY-2003, 09:23 UT).

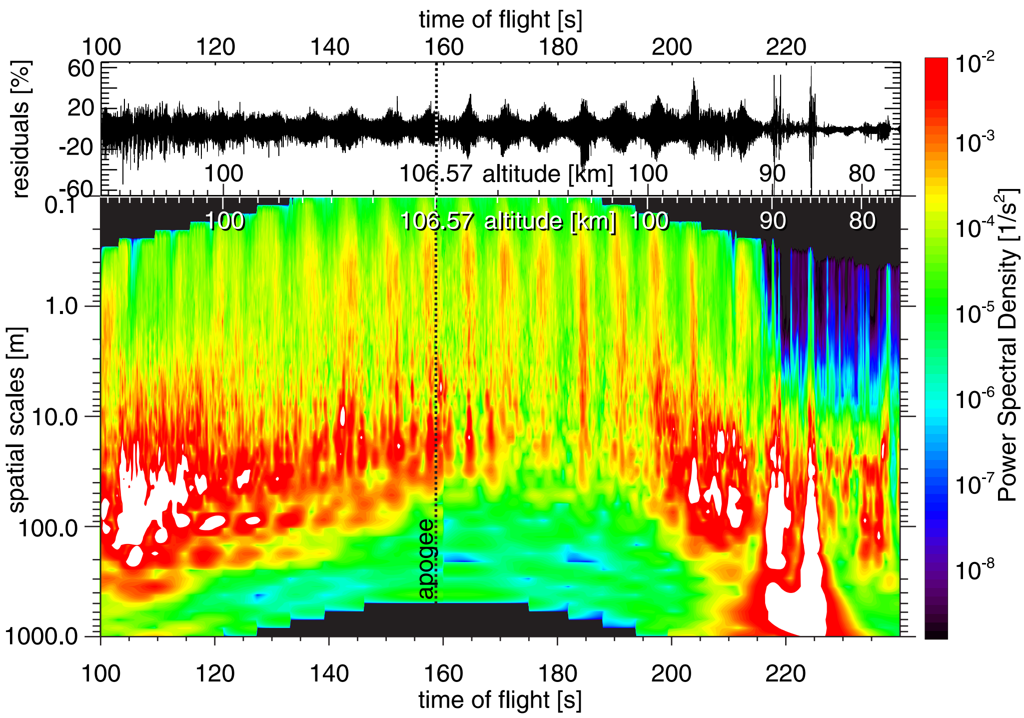

Figure 7.7: The same as Fig. 7.6 but for electrons.

measurements (see chapter 6, Fig. 6.20) that were created by turbulence. The difference is that the plasma structuring extends down to the spatial scales of ∼50 cm for ions and even ∼30 cm for electrons, while for neutrals the smallest structuring occur at 6 m. This is consistent with our current understanding of PMSE [*Rapp and Lübken*, 2004] which can be briefly explained as follows. The radar echo is created by the gradients in the refractive index which is directly proportional to the electron density at these altitudes [*Sato*, 1989]. These gradients are produced by neutral air turbulence combined with the effect of charged ice particles resulting in a reduced electron diffusivity [e.g. *Rapp and Lübken*, 2003]. Indeed, if one compares the structures (within 85-90 km region) in scalograms of neutral, ion, and electron density fluctuations (Fig. 6.20, 7.6, and 7.7 respectively) and with the ε-profile derived for this flight (the leftmost panel in Fig.6.23), the striking similarity implies that these structurings are the signatures of the turbulence activity.

7.2.2 Transition: PMSE to plasma instabilities

The slice of the scalogram shown in Fig. 7.6 taken at ~3 m along the altitude axis is shown in Fig. 7.5. Fig. 7.5 shows that the in situ measurements within the height range from ~85 km to ~92 km resemble the mean PMSE display shown by the shaded area; however, higher up from the PMSE signature the power of the in situ measured data further increases while the radar echo disappears. Note that the profile of in situ measured ion density fluctuations during the RO-MI-03 flight shows the same behavior during the ascending part of the rocket trajectory. These are the signatures of plasma instabilities which we will discuss in the next sections.

This spectacular manifestation of the in situ detected signature of PMSE, however, rises further questions. Why does radar echo disappear while the in situ measured $PSD(\Delta N_i, k_{Bragg})$ profile shows a power increase? We suggest the following explanation. As described in Chapter 3, the collision- to gyro-frequency ratio decreases with height (see Fig. 3.3). As a result the electrons become magnetized at altitudes of about 100 km (Fig. 3.3(a)). That is, they can freely move along the geomagnetic lines, thereby smoothing any structuring along this direction [e.g. **?***Fejer*, 1996; *Hunsucker and Hargreaves*, 2002]. As also described in Chapter 3, E-region plasma waves propagate transverse to the Earth's magnetic field, thereby creating structures in plasma density which are perpendicular to the B-field. These density perturbations create gradients in a refractive index which also produces radar echoes if radar probes almost horizontally at polar latitudes (i.e., perpendicular to the B-field). Such radars as SuperDARN, which comprises a network of HF radars at high latitudes in the northern and southern hemispheres, measure, amongst other things, the line-of-sight velocity of the ionospheric irregularities [**?**].

If we focus on the height region from 90 to ~92 km, we can see the large-scale signatures which are rather PMSE-specific features (Fig. 7.6 and 7.7). Higher up from this region the structuring at the largest scales vanishes while the power at the small-scales rises. In particular, one can also see a strong signal at 3 m scales in Fig. 7.5. Pronounced structuring at 50 m and smaller scales, and especially at centimeter-scales, is a typical plasma instability feature [e.g. *Fejer*, 1996]. At the height region from 90 to ~92 km, however, one can see both strong fluctuations at large scales of ~1 km and increasing power at very small scales of ~30 cm (Fig. 7.6 and 7.7). This is the altitude region of the transition from PMSE to plasma instabilities. There is no obvious spatial border between these different types of structuring. This transition region probably has both types of structuring: due to neutral air turbulence (which can create structures causing PMSE) and unstable plasma waves.

We begin the discussion of the E-region plasma instabilities with the case of the RO-MI-03 flight. In section 7.2.4 we return to the RO-MI-01 flight.

7.2.3 RO-MI-03 plasma instabilities

The next and even more striking feature that we want to discuss in this section is the small-scale ion density fluctuations which appear in the spectrogram (Fig. 7.3) at 105 seconds (92 km altitude) during the upleg of the rocket flight and extend to about 165 seconds of the rocket flight time. They disappear on the descending part of the rocket trajectory shortly after the apogee at about 106 km altitude.

These fluctuations appear in the range of spatial scales from approximately 80 m to 30 cm. These fluctuations are especially pronounced between 105 and 125 s of the rocket flight time (altitude range between 92 and 101 km) during the ascent of the rocket flight, where the power reaches values on the order of 10^{-2} s^{-2} (red color in the spectrogram). These large fluctuations are also clearly seen in the residuals in the upper panel of Fig. 7.3. At 105 s (92 km altitude) the amplitude of the relative ion density fluctuations (residuals) rises abruptly. Between 105 and 125 s of the rocket flight time (92 to 101 km altitude), the broadband density fluctuation level is of the order of 5 to 15 %. After that time (altitude), until 165 s of the rocket flight time (106 km altitude on the downleg), the ion density fluctuations are weaker but still significantly larger than the noise level of $\sim$2 %: i.e., they have an amplitude of 5 % on average. In the spectrogram (Fig. 7.3, lower panel) this weaker part of the small-scale fluctuations is reflected by the green color which corresponds to power values ranging from 10^{-6} to 10^{-4} Hz^{-1}.

Another representation of the observed small-scale plasma irregularities and its development (in the rocket flight time domain) is demonstrated by the altitude profiles of $PSD(\Delta N_i, k)$ shown in Fig. 7.4. During the upleg of the rocket flight (red line) immediately above the PMSE signature, the curve shows an increase over another couple of orders of magnitude. Starting from 102 km altitude this profile gradually decreases in magnitude. Around the apogee a smooth transition from the red upleg curve to the blue downleg curve takes place, with values being $\sim$3 orders of magnitude smaller than during the upleg. We do not consider it to be an effect of different flight conditions (upleg and downleg), since *Blix and Thrane* [1993] showed that small-scale structures are not influenced by this effect.

Note that the electron temperature measurements (section 7.1, Fig. 7.2) are fully consistent with the morphology of the positive ion density fluctuations described above: They only show a significant temperature increase in the same height range where strong positive ion density fluctuations were observed: i.e., between 94 and 102 km during the ascending part of the rocket flight. In contrast, no temperature increase was found during the downleg part. Under undisturbed ionospheric conditions the D-region plasma (i.e., electrons and ions) is collisionally dominated such that electrons and positive ions have the same temperature as the neutral gas; however, in the E-region electrodynamic processes can significantly heat the electron and ion gas such that their temperature can be much higher than the neutral temperature. Such enhanced electron temperatures in the height range from about 90 to 120 km were repeatedly observed at high latitudes [**????***Blix et al.*, 1994] and can be quantitatively explained in terms of heating by unstable plasma waves [**?**]. These waves are excited as a consequence of the well known modified two-stream instability [see e.g. **??***Blix et al.*, 1994].

In this context it is interesting to note that theoretical investigations of the E-region plasma instabilities supported by experimental results [see e.g. **??***Blix et al.*, 1994] show that the modified two-stream plasma instability occurs at spatial scales of 20 meters and less. This is well within the scale range where we see the power increase in Fig. 7.3. Hence, our measurements suggest that the observed small-scale positive ion number density fluctuations and enhanced electron temperatures are evidence of a two-stream plasma instability event. Interestingly, very strong plasma density fluctuations were only detected during a short part of the rocket flight between 105 and 125 seconds. Then they gradually decayed and finally disappeared shortly after the apogee of the rocket trajectory. Here we emphasize the fact that the plasma instability *"switched off"* at about the 165th second of the rocket flight time. A more detailed analysis of this event is presented in the next section.

Analysis of the instability

As described in the previous sections, both the small scale analysis of our positive ion density measurements as well as the electron temperature measurements suggest that we observed a plasma instability during the upleg part of the rocket trajectory which suddenly disappeared shortly after passing the apogee. In this section we investigate whether the sudden disappearance of the instability is due to a spatial or a temporal limitation of the instability region: Close to the apogee the rocket trajectory is almost horizontal, which might suggest that a spatial limitation of the plasma instability structure was observed. On the other hand, electric field mapping and electron acceleration in the crossed electric and magnetic fields are fast processes compared to the duration of the rocket flight. This might in turn mean that a temporal change of ionospheric conditions is the likely cause for the observed behaviour of the plasma instability.

As described in Chapter 3, the driving force for the E-region plasma instabilities is the electric field component, E, which is perpendicular to Earth's nearly vertical magnetic field, B. Thus, if either of the fields (E or B) changes, the plasma drift velocity V_D also changes. Therefore, to understand the situation, the instability threshold condition (Eq. 3.11) must be examined.

One way to determine whether the ionospheric state changed considerably during the time of our rocket flight is the consideration of ground-based magnetometer measurements. Changes of the ionospheric currents produce magnetic field variations which can be measured at the ground [see **?**, and references therein]. Particularly, the horizontal magnetic field component will significantly deviate from the baseline as the auroral electrojet becomes stronger. Conversely, the horizontal magnetic field, measured at the ground, will show a quiet behaviour with a nearly constant mean value (i.e., only defined by the Earth's static dipole field) when the electrojet decays, with only small diurnal variation (i.e., the Quiet Day Curve, QDC). In the upper panel of Fig. 7.8 we present measurements of the horizontal component of the Earth's magnetic field throughout the day of the RO-MI-03 launch. These were performed with ground based magnetometers at Ny-Ålesund and Longyearbyen (see section **??**). In the lower panel, we show electric field variation derived from magnetic field variation with respect to the QDC (shown as dashed line in the upper panel of Fig. 7.8; see **?** for details on how to derive the QDC).

By the red thick line we mark the magnetometer measurements performed exactly during the time interval of the rocket flight. This red line starts at a flight time of 0 seconds and stops at a flight time of 250 seconds where the rocket altitude is below 70 km. The vertical dotted line marks the apogee of the rocket trajectory of 158.6 seconds. As one can see, the horizontal magnetic field changed significantly exactly during the time of the rocket flight.

Another way to check the ionospheric state during the RO-MI-03 flight is to use CUTLASS radar measurements. SuperDARN [**?**] comprises a network of HF radars at high latitudes in the northern and southern hemispheres, which measure the line-of-sight velocity of F region ionospheric irregularities. During the time of the rocket launch, each radar of the SuperDARN network was running a standard 16 beam scan, with each beam sounding 70 range gates of 45 km each, starting at a range of 180 km. The dwell time for each beam was 7 s, with scans synchronized to start at two-minute intervals. Here data from the CUTLASS radar at Þykkvibær, Iceland, is presented. In addition to the line-of-sight data from this radar, the ionospheric equipotential flow streamlines have been calculated using the technique of **?**. Here the fit to the line-of-sight data is made to a sixth-order spherical harmonic expansion, with the fit stabilized by a statistical pattern keyed to the upstream IMF data from the ACE satellite, delayed by 43 min to allow for the propagation time from the spacecraft to the magnetopause. Such an equipotential map represents a best estimate of the global ionospheric flow.

In Fig. 7.9 we show the plasma velocity measurements from the CUTLASS Iceland radar at Þykkvibær around the rocket launch. In the upper panel the spatial variation of the radar flow measurements is presented for the rocket launch time. One can see that poleward of the launch site the radar measured ionospheric flows. The lower panel presents the time variation of the line of sight velocities from beam 2 of the radar, which is marked on the upper panel. Close to Ny-Ålesund the ionospheric flows maximized close to the launch time. Note that for the radar mode running at the time of launch the CUTLASS radar had a much coarser time resolution than the magnetometer measurements (two minutes against ten seconds). In addition radar data presented in Fig. 7.9 are averaged in time over seven seconds for each beam, but only sampled every two minutes.

Thus, ground based magnetometers have registered a significant variation of the horizontal component of the Earth's magnetic field exactly during the rocket flight time. This in turn means, that the ionospheric electric field was changing [**?**] and suggests that we observed the time variation of a plasma instability during the rocket flight. This hypothesis is strengthened by independent observations of the CUTLASS radar which also registered significant variations around the rocket launch time and near the rocket launch site.

In order to gain further insight into the observed plasma instability event we continue in the next section with an estimate of the auroral electrojet electric field variation from the ground based measurements of the magnetic field variations (section 7.2.3) and from the plasma velocity measurements with the CUTLASS radar (section 7.2.3).

Magnetometer data conversion

We are able to convert the observed magnetic field variations to variations of the E-region electric field, since most of the ionospheric parameters required for this conversion were simultaneously measured during the event we are studying. We follow the work of **?** who studied the geomagnetic variations caused by the ionospheric currents based on a large amount of data acquired with ground-based magnetometers and incoherent scatter radars that can directly measure parameters of the electrojet (ionospheric electric field and ionospheric electric currents). Summarizing their conclusions as they apply to our particular case, we recapitulate the following statements:

1. The horizontal component of the magnetic field B_x measured at the Earth's surface can be empirically represented by a linear fit to the ionospheric Hall current[1] $J_H = \Sigma_H E_x$ where Σ_H is the height-integrated Hall conductivity (Eq. 3.7):

$$B_x = a \cdot J_H + b \tag{7.3}$$

2. The coefficient a of this linear fit ranges between 0.55 nT/(A/km) and 0.67 nT/(A/km).

3. The value of the coefficient a tends to decrease when the ionospheric current approaches the site of observations and is estimated as 0.56 nT/(A/km) when the current is located over the magnetometer.

[1]Note that at the altitude range considered here the Hall conductivity (and therefore current) significantly dominates (see chapter 3 Fig. 3.1).

In our case

- We have measurements of the magnetic field B_x performed by the magnetometer.
- We can derive Σ_H on the basis of the in situ measured parameters.

The unknown is the horizontal electric field E_x which can be derived from Eq. (7.3) as:

$$E_x = \frac{B_x - b}{a \cdot \Sigma_H} \tag{7.4}$$

In this equation, the constant b can be derived from the condition that the electric field equals zero when the magnetic field equals the baseline value. We use the quiet day curve (QDC) as a baseline $\langle B_x \rangle$ to derive the relative magnetic field fluctuations. Thus, from Eq. (7.4), substituting $E_x = 0$ and $B_x = \langle B_x \rangle$ we get:

$$b = \langle B_x \rangle \tag{7.5}$$

Finally, for the electric field estimate we have:

$$E_x = \frac{B_x - \langle B_x \rangle}{a \cdot \Sigma_H} \tag{7.6}$$

The height-integrated Hall conductivity is given by Eq. 3.7, where the specific Hall conductivity, σ_H, can be derived by substituting in situ measured parameters in Eq. 3.3, where $B = B_z$ is the vertical component of the Earth's magnetic field.

In Eq. 3.7 the integration must be performed over the altitudinal extent of the electrojet. In principle the height region of the electrojet can be directly estimated from incoherent scatter measurements of the drift velocities of positive ions. Such direct measurements are, unfortunately, not available in our case; however, from previous observations we know, that the electrojet flows within the altitude range from ~75 up to ~130 km [see e.g. **???**]. Unfortunately, our measurements only extend from 75 km to the altitude of the rocket apogee at 106 km. Hence, Σ_H can only be directly derived by integration over this altitude range. By extrapolating our measurements to larger altitudes, however, we may examine the sensitivity of our derived results on this limitation. This will be discussed in further detail below.

In order to calculate Σ_H, we substitute the neutral and ion densities measured in situ into the Eq. 3.4. Electron densities and temperatures measured in situ further allow us to derive the electron collision frequency (Eq. 3.5).

Using Eq. (7.6), we calculated the electric field on the basis of our combined ground based and rocket borne observations. The result of these calculations for the magnetometer measurements performed at Ny-Ålesund and Longyearbyen is shown in the lower panels of Fig. 7.8. In these figures the electric field is shown as a grey shaded area indicating the uncertainty that accounts for both uncertainty in the definition of the coefficient a and our lack of knowledge about the actual vertical extent of the electrojet (see below for a more detailed discussion of this uncertainty).

E-field from velocity measurements

The CUTLASS radar measurements themselves can provide evidence for the ionospheric disturbances, their spatial structure and time evolution.

Fig. 7.9 presents the CUTLASS measurements performed during the RO-MI-03 flight. The first interesting feature in this figure is that the main region of the structuring appeared

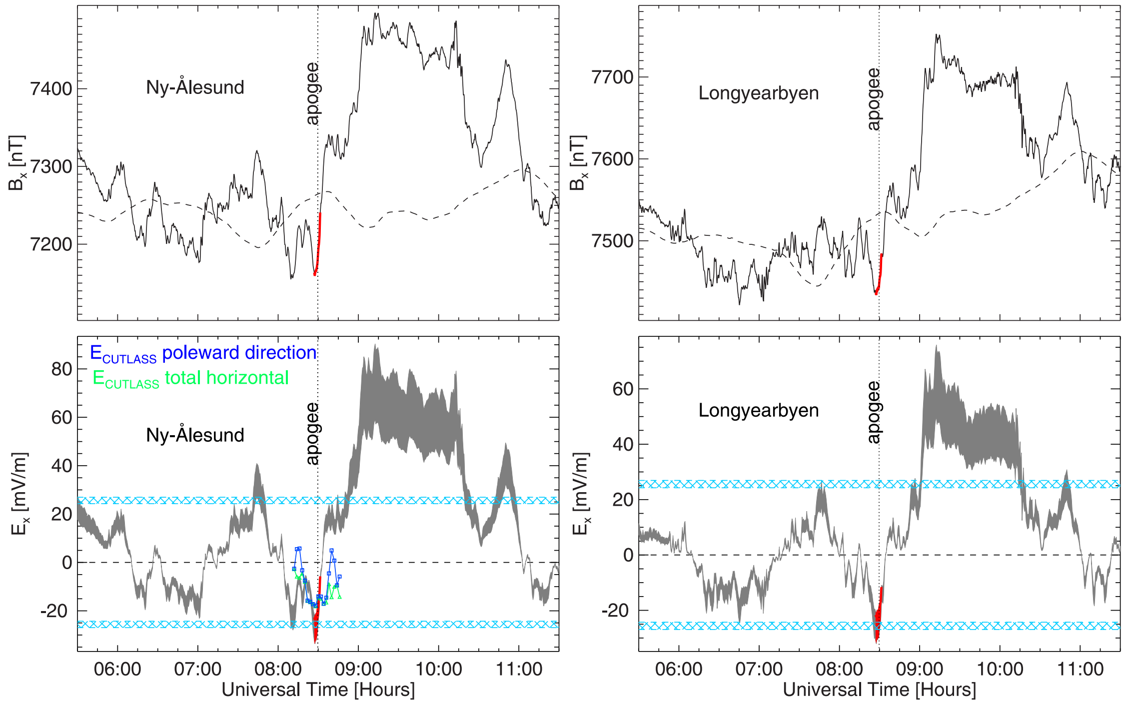

Figure 7.8: Variation of the horizontal component of the Earth's magnetic field (upper panels) measured by the ground based magnetometer at Ny-Ålesund (left panels) and Longyearbyen (right panels) throughout the day of RO-MI-03 launch. Lower panels: Electric field derived from the magnetometer measurements shown in the upper panels. The QDC shown by the dashed curve was taken as the baseline for the B to E field conversion (see text). This line corresponds to the dashed horizontal zero line in the lower panel. The red filled area in both the upper and lower panels indicates the time of the rocket flight. The vertical dotted line marks the apogee of the rocket trajectory of 106.1 km. Cross-hatched regions indicate the threshold electric field for the modified two-stream instability with uncertainty (see text). The green and blue profiles in the lower left panel show the total horizontal and poleward-directed E-field values as converted from the CUTLASS velocity measurements.

poleward of the rocket launch site. This feature suggests that the rocket entered the disturbed region rather than leaving it.

In this section we present another estimate of the ionospheric electric field based on the plasma velocity measurements. Here we use the estimates of the ionospheric flows at the location of the rocket derived from the ionospheric equipotential flow streamlines, which are shown for one two-minute scan as contours in the upper panel of Fig 8. This plasma drift velocity can further be converted to the horizontal ionospheric electric field as:

$$E_x = V_D \cdot B_z \tag{7.7}$$

where B_z is the vertical component of the Earth's magnetic field.

The results of this conversion are also shown in Fig. 7.8 as blue and green profiles. As one can see, the E-field values derived from the CUTLASS measurements qualitatively agree with the electric field converted from the magnetometer measurements. CUTLASS E-field estimates show a similar change during the time of the RO-MI-03 flight, although the absolute values derived from the velocity measurements are smaller.

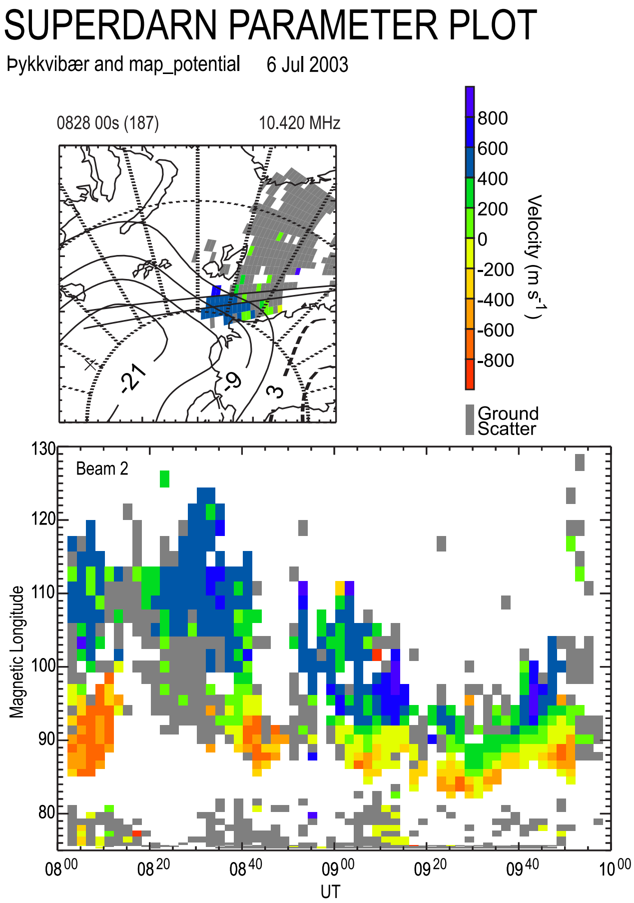

Figure 7.9: Plasma velocity measurements from the CUTLASS Iceland radar at Þykkvibær around the rocket launch. In the upper panel the spatial variation of the radar flow measurements is presented for the rocket launch time. The lower panel presents the time variation of the line of sight velocities from beam 2 of the radar, which is marked on the upper panel. Note that the radar data presented in this figure are averaged in time over 7 seconds for each beam, but only sampled every two minutes. Geomagnetic longitude of Ny-Ålesund is $\sim 110°$E. Courtesy of T. K. Yeoman.

Two-stream instability threshold.

The next step in our analysis of the observed plasma instability event is to estimate the theoretical threshold condition for the instability. As was already mentioned above, the two-stream instability requires the electric field to exceed a threshold value, which can be derived from Eq. (3.11), assuming pure electron $\boldsymbol{E}\times\boldsymbol{B}$ drift (because $V_e \gg V_i$) with a velocity $V_D = E_x/B_z$ [see e.g. *Blix et al.*, 1994]:

$$E_x \geq C_s(1 + \psi_0)B_z \tag{7.8}$$

At an altitude of 100 km, ψ_0 is of the order of 10^{-1}, and the threshold electric field estimated from Eq. (7.8) shows that an electric field of at least 20 mV/m is required for the instability to be excited [*Blix et al.*, 1994]. The threshold electric field value grows rapidly with decreasing altitude due to the nearly exponential increase of ψ_0 with increasing neutral number density. Hence, at 90 km the threshold value becomes already as large as 80 mV/m.

Using Eq. (7.8) we derived the threshold electric field for the RO-MI-03 flight. For all the involved parameters we used the relevant instant values measured during the rocket flight, so that the derived threshold electric field values correspond to the exact spatial coordinates of the rocket. One source of uncertainty for this derivation comes from the limitation that no ion temperature measurements were conducted during our rocket flight; however, according to numerous previous observations, in the altitude range of the RO-MI-03 rocket flight (that is below 106 km) the ion temperature will not exceed the electron temperature but rather closely approach the neutral temperature [**???***Blix et al.*, 1994]. Thus, we can estimate that the ion temperature lies somewhere between the electron and the neutral temperature. From Eq. (7.8) and Eq. (3.12) it is also seen that an ion or electron temperature increase stabilizes the plasma. As also expected from theory, the smallest derived values for the threshold electric field correspond to the apogee of the rocket trajectory at 106.1 km. In Fig. 7.8 we show the derived threshold electric field value taken at the apogee of the rocket trajectory as cross-hatched regions which accounts for the uncertainty of the ion temperature approximation. It is clearly seen already from Fig. 7.8 that the rocket passed the threshold condition around the apogee point.

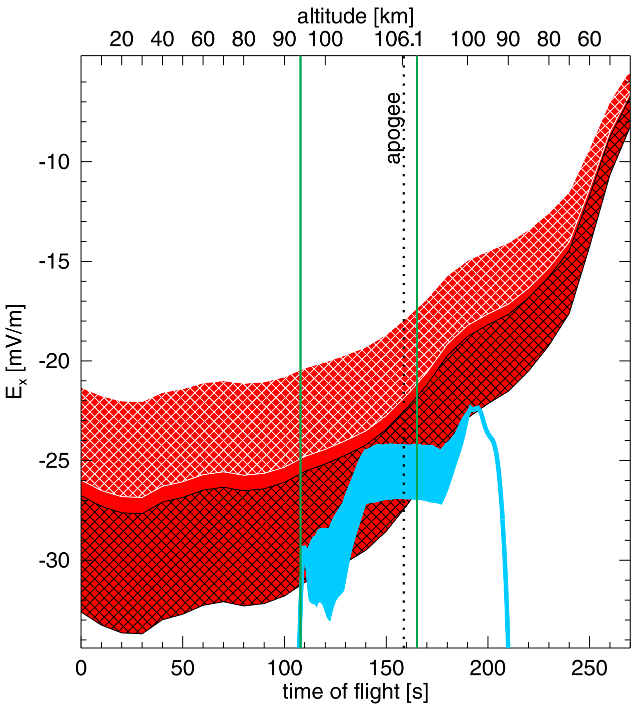

Figure 7.10: Variation of the horizontal component of the electric field derived for the RO-MI-03 launch. The red shaded area represents the uncertainty for the derived electric field which incudes both the uncertainty in the definition of the linear fit coefficient a and the indeterminacy of the altitudinal extent of the electrojet (see text). Cross-hatched regions indicate the uncertainty in the definition of the coefficient a. The white cross-hatched region corresponds to the maximum supposed altitudinal extent of the electrojet; black to the minimum (see text). The blue line with a filled area shows the threshold electric field with an uncertainty which comes from the approximation of the ion temperature between the measured electron and neutral temperatures. The vertical dotted line marks the apogee of the rocket trajectory. Vertical green lines show the time (altitude) interval in which the enhanced power in the Fig. 7.3 is seen.

Though the CUTLASS E-field qualitatively resembles the magnetometer-derived E-field profile, it does not reach the threshold electric field value (Fig. 7.8). This might be a consequence of the time resolution of the radar data. The magnetometer E-field profile clearly shows high values on a time scale smaller than the two-minute radar resolution, and smoothing will imply smaller absolute values for the magnetometer data.

To visualize more details of the developing situation, we show the electric field variation exactly during the time of the rocket flight in Fig. 7.10. The red shaded area here shows the same electric field values as the red area in the lower panel of Fig. 7.8. The vertical dotted line indicates the apogee of the rocket trajectory. The blue line with the filled area shows the threshold electric field derived from Eq. (7.8) with an uncertainty which comes from the approximation of the ion temperature between the measured neutral and electron temperatures. The upper border (smallest absolute values) corresponds to the ion temperature equal to the neutral temperature. The vertical green lines show the time (altitude) interval where we see the power increase in the Fig. 7.3. As long as the magnitude of the electric field is larger than the threshold (i.e, as long as any profile taken within the red shaded area lies below the blue line), the condition for the two-stream instability is fulfilled whereas otherwise the instability cannot be excited.

We have also considered the second type of uncertainty for the derivation of the electric field due to the uncertainty of the altitudinal extents of the electrojet (see section 7.2.3). The resulting variation in the derived electric field is shown in Fig. 7.10 as a red shaded area. We calculated the electric field for two additional supposedly different altitudinal extents of the electrojet, i.e., from 75 to 108 km and from 75 to 109 km. The black cross-hatched area corresponds to an altitudinal extent of the electrojet between 75 and 106 km: i.e, the altitude range where our measurements are available. The white cross-hatched area corresponds to the altitude range of the electrojet that was additionally extended by 3 km (i.e., from 75 to 109 km). To extend the height integrated conductivity we extrapolated the quantities involved in its calculation. Specifically, the neutral and plasma densities were linearly extrapolated in a logarithmic domain and the plasma temperature was approximated between the linear extrapolation of the measured neutral temperature and the plasma temperature derived at the apogee of the rocket trajectory (i.e. 400 K). The extended plasma density profiles resemble the ones derived by means of the International Reference Ionosphere (IRI-2001, *Bilitza* [2001]), and neutral density and temperature profiles, resemble the MSIS90-derived profiles.

The threshold profile remains unchanged because it depends on electron and ion temperatures only. The magnitude of the horizontal ionospheric electric field derived from Eq. (7.6) decreases when we increase the altitudinal extent of the electrojet in our calculations. Hence, a further broadening of the electrojet's height extent leads to a situation in which the modified two-stream instability is completely suppressed.

In any case, our analysis suggests that the magnetometer-derived electric field is close to or even larger than the threshold E-field during the ascending part of the trajectory. On the descending part, however, the inferred electric field decreases substantially such that an instability cannot be excited. Hence, our analysis suggests that the disappearance of small-scale irregularities on the downleg of our rocket flight could be due to a temporal variation of the ionospheric electric field.

Spatial variation

We have still not excluded the fact that we observed a spatial limitation of the instability region rather than a temporal development. To check this hypothesis we have performed the same electric field analysis for the Earth's magnetic field measured at Longyearbyen and other distant available stations (Fig. 7.11) assuming that our in situ measured plasma parameters also apply for these other stations. The derived electric field for Longyearbyen reveals the same abrupt decrease during the RO-MI-03 flight. In fact, even absolute values are very close to those at Ny-Ålesund. Then we checked the magnetic field measurements conducted with the next closest magnetometer, which is located at Hopen, approximately 290 km south of Ny-Ålesund. The ionospheric electric field derived under the same assumptions as described above for the case of Hopen shows a quieter behavior but still resembles that at Ny-Ålesund and Longyearbyen (Hopen values are not shown here). Finally, further to the south at Bjørnøya (geographical coord. 74.5°N, 19.0°E; geomagnetic coord. 71.5°N, 107.8°E), which is another 223 km south of Hopen, the electric field is very quiet and much weaker than any possible threshold for the two-stream plasma instability (magnetometer measurements at Bjørnøya are not shown here).

This situation is schematically summarized in Fig. 7.11. The grey shaded area shows the electric field values, derived for the apogee of the rocket trajectory with all the uncertainties discussed in section 7.2.3. The vertical bars are plotted to give an impression on the spatial resolution of the magnetometer measurements. The cross-hatched region represents the threshold electric field with its uncertainty, which comes from the approximation of the ion temperature between measured electron and neutral temperatures. The suggestion that the electric field is limited in space is demonstrated by the dashed line. The tendency, which is seen from the comparison of the magnetometer measurements shown, suggests that the DC component of the electric field changed rather gradually. This means that the electric field, as strongly as it was detected at Ny-Ålesund, most likely cannot have decayed at such small spatial scales as the horizontal projection of the rocket trajectory (i.e., less then ~50 km).

Turning to the CUTLASS measurements (Fig. 7.9), we see again, that they also show that the main region of strong electric fields appears to be concentrated poleward of the rocket launch site, with little evidence of strong fields at lower latitudes. This is consistent with our analysis of the latitude dependence of the electric field derived from magnetometer measurements. CUTLASS measures its strongest flows close to the rocket launch time, which supports the temporal rather than a spatial interpretation of the instability event.

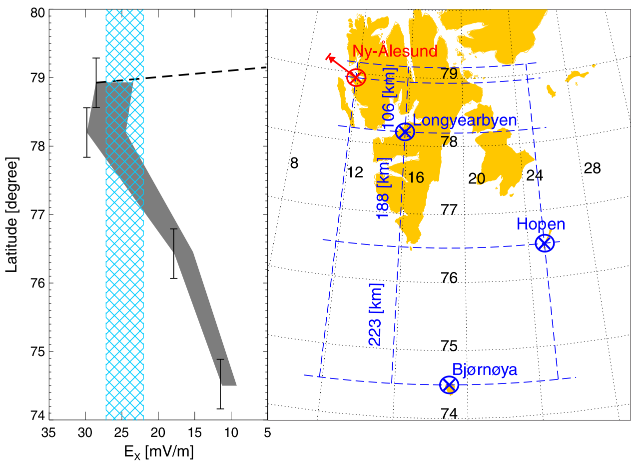

Figure 7.11: Map of Svalbard (right panel). DC component of the horizontal electric field while changing with latitude. Uncertainty derived from the magnetometer measurements for the apogee of the rocket trajectory is shown as a grey filled region in the left panel. Vertical error bars give an impression on the spatial resolution of the magnetometers. The cross-hatched region indicates the threshold electric field with uncertainty derived for the apogee of the rocket trajectory. The dashed line in the left panel demonstrates the suggestion that the spatial limitation of instability was detected.

On the other hand, neither the magnetometer nor the CUTLASS radar measurements resolve ionospheric structures at spatial scales of some kilometers. This fact does not allow us to ultimately exclude the interpretation of the observed structure as a spatial limit.

RO-MI-03 instability summary

We have presented in situ observations of a plasma instability obtained during a sounding rocket flight performed at Ny-Ålesund (Spitzbergen, 78.9°N) on 6 July of 2003 at 08:27 UT. The special feature of this event is the *"switch off"* of the instability just after the apogee. This can be explained by either a spatial or temporal limitation of the observed structure. To answer the question about the reason for this limitation we have quantitatively estimated the ionospheric electric field based on ground-based magnetometer measurements and in situ derived plasma parameters. The derived electric field variation during this flight, compared to the theoretical threshold condition for the two-stream plasma instability, can explain the limits of the observed structure. Independent measurements performed with the CUTLASS radar show that the electric field exhibits a similar behavior during the time of the rocket flight, and they support the time development interpretation of the observed structure.

In contrast, the assumption that a spatial rather than temporal variation of the plasma instability was observed is not consistent with the interpretation of the observed geomagnetic variation. Again, CUTLASS radar measurements show ionospheric structuring in the poleward direction of the rocket launch site: that is, along the direction of the rocket flight.

On the other hand, the spatial resolution of the ground-based instruments is much coarser than that of the in situ measurements. Therefore, it is not possible to absolutely exclude the interpretation of the observed disappearance of the plasma instability as a spatial border.

In contrast, rocketborne observations are able to detect different features of plasma structures at a very high spatial resolution. Hence, future in situ observations of E-region plasma structures should pay more attention to and gain closer insight into this particular feature.

7.2.4 RO-MI-01 plasma instabilities

As mentioned above, unusually strong plasma density fluctuations were detected during the flight RO-MI-01. In Fig. 7.12 and 7.13 we present density fluctuations and their spectrograms measured during the first rocket flight (RO-MI-01) for both positive ions and electrons.

As one can directly see from both the residuals (upper panels of Figs. 7.12, 7.13) and spectrograms (lower panels of Figs. 7.12, 7.13), very strong plasma density fluctuations were detected on both the upleg and downleg in the altitude range between ~90 km and the apogee of 106.57 km. Specifically, 20 % residuals were detected during this (RO-MI-01) flight, whereas 10 % residuals were measured during the last flight. This corresponds to power values which are three orders of magnitude higher than during flight RO-MI-03. Note also that the payload experienced a pronounced coning motion during this flight. Consequently, the signal is modulated at a wavelength of several kilometers.

It is also worth mentioning here that the ionospheric electric field estimated from the ground based magnetometer measurements showed a persistent large value of about 50 mV/m during the entire flight. This means that the threshold condition for the modified two-stream instability was fulfilled during the entire flight (see e.g. *Blix et al.* [1994]).

As in the case of the RO-MI-03 flight, we also see small-scale structures typical for the two-stream instability: i.e., in the spatial scale range from ~20 meters to tens of centimeters. One also can see the gradient drift mode in the spectrograms: i.e., a power enhancement at spatial scales of about hundreds of meters, which is weakened on the downleg compared to the upleg. Unfortunately, there was no radio wave propagation experiment incorporated during this particular rocket flight. Therefore we were not able to derive absolute plasma densities. Also, the electric field experiment incorporated during this particular flight failed, so we cannot examine this feature more quantitatively.

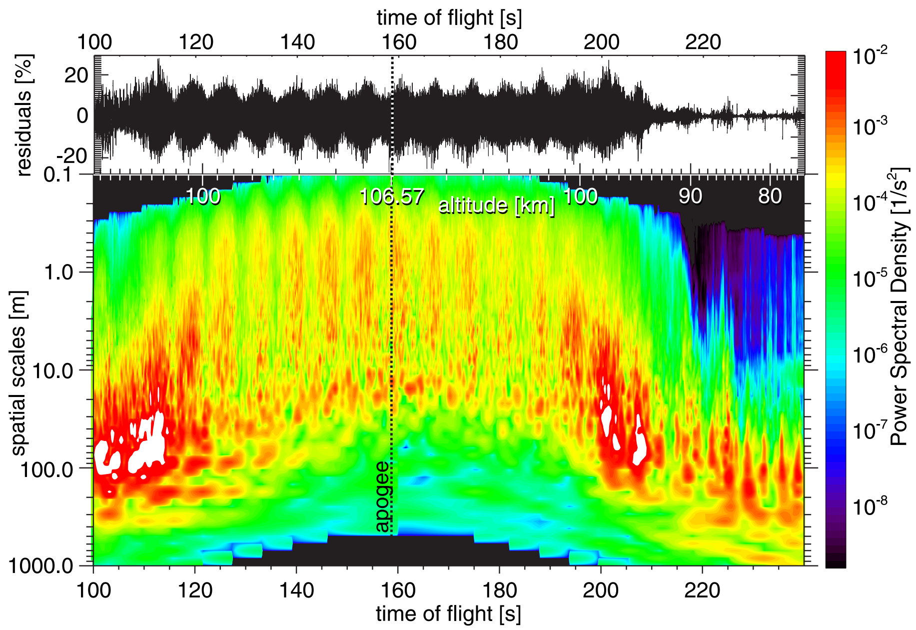

Figure 7.12: Upper panel: Relative density fluctuations ($\equiv$ residuals) of positive ions measured during the flight RO-MI-01. Lower panel: Wavelet spectrum of these relative ion density fluctuations: i.e., power spectra resolved both in time/altitude and spatial scales. The dotted line marks the apogee of the rocket trajectory of 106.57 km. After *Strelnikov et al.* [2005].

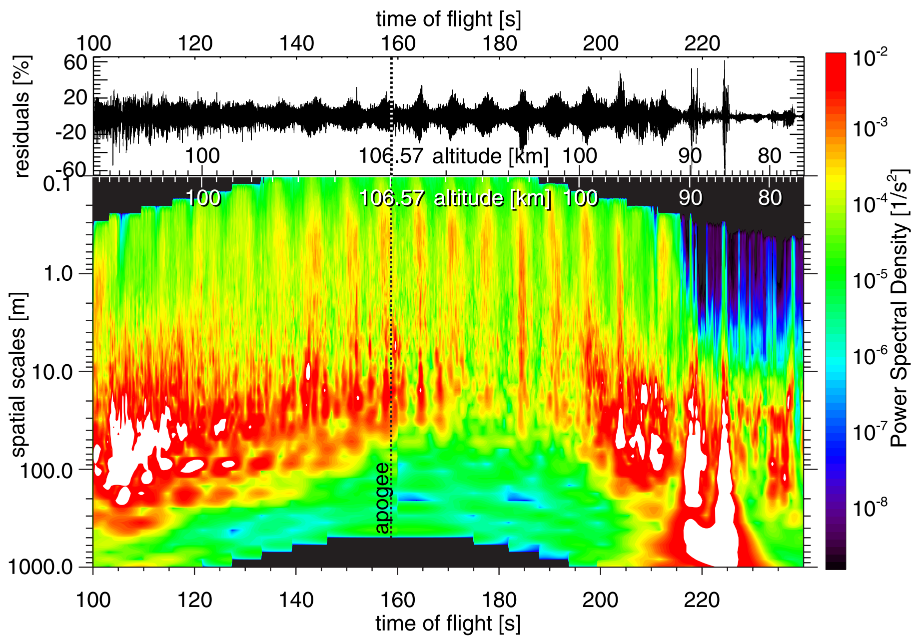

Figure 7.13: As Figure 4, but for electrons. After *Strelnikov et al.* [2005].

The most important feature we want to stress is the strength of the plasma density fluctuations measured during the flight RO-MI-01.

7.2.5 RO-MI-01 neutral fluctuations

Next, we come to the most astonishing part of our plasma dynamical studies, i.e. high frequency neutral air density fluctuations, detected during the first rocket flight (RO-MI-01) in the altitude range where the plasma instability discussed above was observed.

In Fig. 7.14 we present the same type of relative density fluctuations and the related spectrogram, as shown for the plasma species in Fig. 7.12 and 7.13 but derived from the neutral air density measurements performed by the CONE instrument.

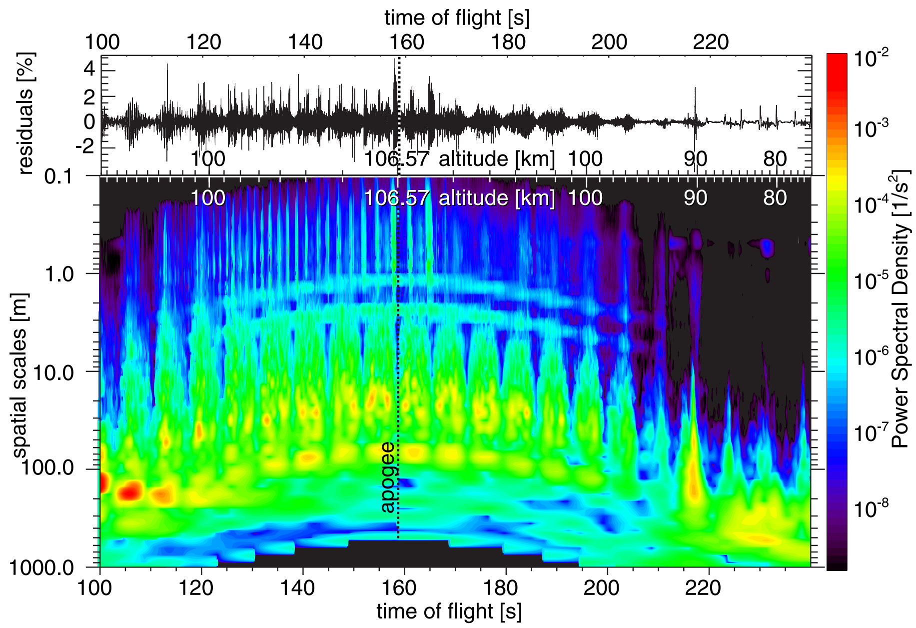

Figure 7.14: Upper panel: Relative density fluctuations (≡ residuals) of neutral air measured during the flight RO-MI-01. Lower panel: Wavelet spectrum of these relative neutral air density fluctuations: i.e., power spectra resolved both in time/altitude and spatial scales. The dotted line marks the apogee of the rocket trajectory of 106.57 km. After *Strelnikov et al.* [2005]

First, we comment on the residuals plot (upper panel of the Fig. 7.14). In the height range between ∼95 km and apogee, one sees very large relative density fluctuations, i.e. residuals showing amplitudes of about 2 % on average and often up to 4 %. It is also significant that the 1 % residuals in the altitude range from 93 to 73 km on the downleg reveal the occurrence of turbulence layers as identified by our spectral analysis technique (see *Strelnikov et al.* [2003] and section 6.2).

The next feature seen in both the residuals (Fig. 7.14, upper panel) and the spectrogram (Fig. 7.14, lower panel), is that the time/altitude range in which large and high frequency neutral density fluctuations were detected is enclosed in the time/altitude range of the strong plasma density fluctuations (Fig. 7.12, 7.13) discussed above.

Such very large high-frequency neutral density fluctuations were never observed in any of our previous flights. In the following we discuss the potential causes of these fluctuations. First, we must mention that all the payload channels providing information about the technical performance of our instruments were carefully checked and instrumental effects have been excluded.

The next hypothesis was that ions accelerated in the $\mathbf{E} \times \mathbf{B}$ fields could penetrate the shielding of the CONE instrument: i.e., anode potential of +85 V. A simple estimate, however, shows that to realize this situations, we need an ionospheric electric field of ∼1300 mV/m which is unreasonably high.

Can these neutral air density fluctuations around the apogee of the RO-MI-01 flight be induced by the plasma processes in the lower E-region? This is also hardly believable, taking into account the difference between the neutral air and plasma (i.e., electrons and ions) densities. The plasma density is smaller than neutral density by at least a factor of 10^7 m^{-3} at ∼100 km altitude (see density measurements presented in section 7.1).

Another possible mechanism can be the resonant charge exchange: that is the ion-neutral collisions that result in very fast ions' becoming neutrals and vice versa after the collision if their temperature is higher than 300 K [e.g. *Schunk and Nagy*, 2004]. We do not consider this a likely case because the ion temperature, as we estimated, is rather close to the neutral temperature: that is, not higher than 300 K.

The next hypothesis tested is that neutral air turbulence created the density perturbations we measured. In the upper panel of Fig. 7.15 we present a 1 km interval of relative neutral air density fluctuations measured during the flight RO-MI-01. This is the same data as presented in Fig. 7.14 but only for an altitude of 104±0.5 km. In the lower panel of Fig. 7.15 we present the Fourier power spectrum of the residuals shown in the upper panel. The long-dashed line represents the best fit by the Heisenberg spectral model (see e.g. *Lübken et al.* [2002]). Clearly, it is technically possible to fit such a theoretical spectrum of turbulence to the measured spectrum; however, the energy dissipation rate ε resulting from this fit gives an unexpected value of ∼202 GW/kg ±15 % which is certainly much too large.

Summarizing the whole discussion above, one has to say that we are convinced that the small-scale neutral density fluctuations observed during the flight RO-MI-01 are the real geophysical feature; however, this new experimental result cannot be interpreted using our current knowledge, and it is a challenging task for our future studies.

In the future we intend to investigate the energy balance at the altitudes under consideration. In particular, we intend to estimate the total energy contained in the plasma instability and compare this to the energy needed to create the observed 2 % fluctuations in the neutral gas. Should this comparison show that the plasma cannot drive the neutral density fluctuations, a yet unconsidered mechanism is needed in order to explain our observations.

7.2.6 Plasma irregularities: Summary

In this chapter we discussed plasma irregularities owing to different dynamical processes. These are 1) the PMSE, which, inferring both neutral and plasma dynamical properties originate, however, from the pure neutral dynamical process, and 2) the plasma instabilities produced due to the dynamical instability of plasma waves. The spatial separation of these different processes cannot be identified, which in turn might mean that they are at a certain rate coupled. This coupling is a subject of our future investigations and was not discussed in this manuscript.

The first and new result presented in this chapter which connects plasma and neutral air properties, is the comparison of the neutral and electron temperatures conducted in situ simultaneously in the same volume.

Another geophysical result that we presented in this manuscript is the manifestative evidence of coupling between the plasma irregularities and the neutral dynamical processes within the PMSE region. We presented in situ measurements of the density fluctuations in different plasma species and neutral air conducted simultaneously in the same volume. These

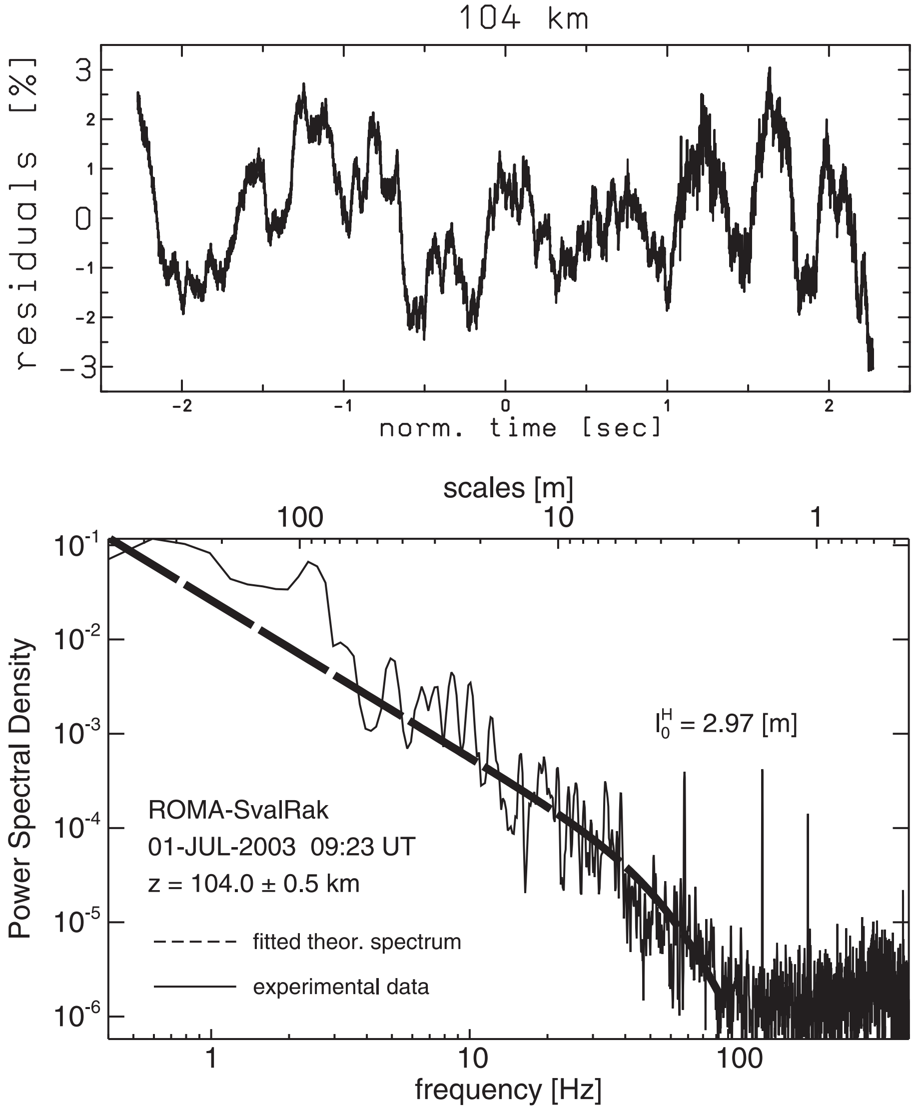

Figure 7.15: Upper panel: 1 km bin of relative neutral air density fluctuations measured during the flight RO-MI-01. Lower panel: Fourier power spectrum of the residuals shown in the upper panel. The long-dashed line represents the best fit curve of a Heisenberg spectral model. Derived energy dissipation rate $\varepsilon \simeq 202\ GW/kg\ \ \pm 15\ \%$ and inner scale $l_0^H \simeq 3\ m$. After *Strelnikov et al.* [2005].

measurements were compared with the PMSE display recorded by the ground based VHF radar, which agreed spectacularly. This result supports our current understanding of PMSE described by *Rapp and Lübken* [2004].

In this chapter we also discussed two different plasma instability events detected during the sounding rockets flights conducted from Ny-Ålesund (79°N). Spectral analysis showed that in both cases we simultaneously observed at least two known modes of plasma instabilities: the two-stream and gradient drift instability. The last rocket flight (RO-MI-03) revealed a switch-off of meter scale ionospheric structures shortly after the apogee of the rocket trajectory. This event was analyzed in section 7.2.3 and was interpreted as the time development of a two-stream plasma instability. The first rocket flight (RO-MI-01) revealed strong plasma density fluctuations on both the upleg and the downleg. Moreover, small-scale strong neutral density fluctuations were also detected during the first flight (RO-MI-01) in the same altitude range where strong plasma density fluctuations were measured. This new experimental result cannot be interpreted using our current knowledge and is to be studied in our future work.

Chapter 8

Summary and Outlook

8.1 Summary

In situ measurements of small-scale irregularities in neutral air and plasma densities in the northern summer MLT region are presented and analyzed. The measurements were conducted at two geographical latitudes: 69 °N (Andøya) and 79 °N (Spitsbergen).

First, in Chapter 5.4 a new technique to analyze the spectral content of small-scale irregularities is presented. This technique uses the wavelet analysis tool and was first applied to the analysis of the neutral air turbulence of the MLT region. In this manuscript we describe this method in detail. We use the continuous (nonorthogonal) wavelet transform. From the vast number of different wavelet functions, we chose the Morlet wavelet for, among the other reasons, the fact that it consists of the plane wave modulated by the a Gaussian and is, therefore, well comparable to the Fourier basis. We discuss the resolution problem of the wavelet technique in both time and frequency domain. Additionally, we compare the resolution of the wavelet technique with that of the Fourier analysis. We show that the Fourier analysis is not able to resolve quickly changing in-time small-scale (i.e., high-frequency) content of a time series. In contrast, the wavelet analysis resolves small-scale irregularities of limited spatial or temporal extent. This valuable property of the new spectral analysis tool makes it possible to see the change of the small-scale (i.e., high-frequency) structures along the measured time series. When applied to the measured time series, this means that we are able to see the full spectral content of the probed structure at each altitude point (the local wavelet spectrum) with very high altitude resolution.

In chapter 6 the new technique is applied to the neutral air density fluctuations measured in situ in a high-latitude summer MLT region. These small-scale structures created by neutral air turbulence are qualitatively investigated and the morphology of the irregularities is discussed. This is the first time/altitude − frequency/spatial scales representation ever made of the turbulent structures measured in situ in the MLT region with such high resolution.

The quantitative turbulence characteristic, the kinetic energy dissipation rate, ε, is retrieved using global wavelet spectra. The new analysis tool makes it possible to deduce the ε altitude profile with at least 100 m vertical resolution (i.e., the best resolution ever achieved of the measured turbulence parameters for the MLT region). This yields a realistic turbulence dissipation field that shows features important for understanding MLT turbulence. These are the sharp, local gradients in turbulent kinetic energy dissipation and magnitude. Additionally, such a highly resolved dissipation field measured in situ gives a valuable diagnostic tool for the turbulence modelers: That is, it allows us to verify model results by measurements.

In section 6.1 results of the MIDAS/MaCWAVE sounding rocket campaign that took place at Andøya (69 °N) in summer 2002 are presented. The different, independent measurements conducted during this campaign discovered special features that all deviate from the values previously observed from the same location by the same instruments. All these measured "unnormal" parameters, like turbulence energy dissipation rates, horizontal winds, and temperatures, appeared to be consistent with each other and were interpreted as a special feature of the year 2002. Interestingly, at the time of the MIDAS/MaCVAVE campaign at high northern latitudes, the dynamical situation of the south polar stratosphere was characterized by unusually large Rossby-wave activity. Finally, the dynamics of the high northern latitudes was connected to the dynamics of the high southern latitudes through the planetary waves activity, as shown by a general circulation model. The results of this campaign represent a comprehensive and consistent set of experimental data, to which we can give a physical interpretation based on our current understanding of the MLT dynamics. In section 6.1, using experimental data, we show the role of the small-scale processes in the MLT dynamics. Namely, the MIDAS/MaCWAVE results demonstrate that the neutral air turbulence in the MLT region affects the wind field. Also, appearing as a result of the waves−mean flow interaction, the small-scale processes are definitely indicative of the changes in the global circulation.

In section 6.2 results of the ROMA/SvalRak sounding rocket campaign that took place at Spitsbergen (79 °N) in summer 2003 are presented. We analyze the small-scale structuring in neutral air density owing to the turbulence activity in the MLT region. These are the first in situ turbulence measurements ever conducted at such high northern latitudes in summer utilizing relative neutral density fluctuations. These measurements appeared to be different from all the other similar ones conducted only 10 ° to the south of this geographical location. The differences are that the MLT turbulence at 79 °N is significantly weaker and spread over a broad altitude range compared to that usually observed at 69 °N. These features are interpreted using the KMCM model and thereby support our current understanding of the basic dynamical processes acting in the MLT region. Specifically, since neutral air turbulence is produced by the gravity waves breaking, turbulence properties depend on the wave characteristics around the mesospheric heights. The waves characteristics in turn depend on the background zonal wind field below those heights (in particular, in the troposphere). At 79 °N this results in a weaker waves filtering and leads to lower and weaker turbulence at higher latitudes.

In Chapter 7 the time resolving spectral analysis tool is further applied to investigate the small-scale structuring in the MLT plasma. As was expected from the previous observations, the D-region plasma reflects a similar structuring to that observed in the small-scale neutral irregularities produced by the MLT turbulence. This introduces the first such detailed insight ever made into the highly resolved spatial morphology of the structuring produced by the MLT turbulence in neutrals and both plasma species (electrons and ions), measured simultaneously in situ in the same volume.

In addition, high-resolution altitude profiles of the amplitude of plasma density perturbations at the VHF-radar Bragg scale deduced from the in situ electron and ion density measurements performed in the same volume by different instruments is also presented. This introduced a comprehensive comparison of the ground-based PMSE observations performed by radar and in situ measurements of density irregularities in both species (electrons and ions) of the D-region plasma measured simultaneously. This in turn gives additional experimental support for the interpretation of PMSE by *Rapp and Lübken* [2003].

In section 7.1 the results of the measurements of the background ionosphere in the MLT region are presented. Among these results the comparison of the in situ measured temperatures of neutral air and electrons, performed simultaneously in the same volume, is a new experimental result. This shows that D-region electrons are a suitable tracer for neutral air temperature measurements, and it gives experimental evidence that the plasma and neutral air within the PMSE altitudes have equal temperatures.

In section 7.2 we examined and discussed the small-scale plasma irregularities produced by unstable plasma waves. Using the time resolving spectral analysis technique, we identified two modes of plasma instabilities in our measurements: the two-stream and gradient drift instability. For the case of the RO-MI-03 flight, where the instability disappeared around the apogee of the rocket trajectory, we performed an additional study using different accompanying measurements, to deduce the ionospheric electric field, which is the driving force for this dynamical process. We concluded that this data set is likely experimental evidence of the two-stream plasma instability, which was likely a short-lived event in this case. The case of the RO-MI-01 flight revealed a strong plasma instability with signatures found in both plasma constituents. Additionally, the neutral air density was disturbed in the region of the strong plasma density fluctuations. This new experimental result cannot be interpreted based on our current knowledge about plasma to neutral dynamics coupling at that region.

The next question that remained open is the altitude region of the transition between small-scale structuring in plasma density produced by the neutral air turbulence (that is the PMSE heights) and plasma irregularities, produced by the unstable plasma waves (plasma instabilities). We briefly discussed this problem in this work, but we still cannot say whether these different dynamical processes interact with each other or just coexist in the same volume.

Taking all these results together, we summarize the new significant findings of this study as follows.

1. We adapted the wavelet analysis tool to derive MLT turbulence characteristics with very high altitude resolution.

2. Using the results of the MIDAS/MaCWAVE sounding rocket campaign we showed that the neutral air turbulence plays a key-role in the residual meridional circulation.

3. We presented the first in situ measurements of the MLT turbulence at very high northern latitudes (79 °N).

4. We presented the first results of in situ measurements of the latitudinal dependence of the MLT turbulence and interpreted it using our current knowledge.

5. We investigated the morphology of the small-scale plasma irregularities and compared it with the small-scale structuring in neutral air density in the height region where PMSE were observed. We also presented the first comparison of in situ measured electron and neutral temperatures in the D- and lower E- regions, performed in the same volume.

6. We applied the wavelet analysis tool to the small-scale plasma density perturbations, measured in situ, which allowed us to identify two modes of plasma instabilities and investigate their properties.

7. We presented experimental evidence of neutral air structuring that occurred in the region of strong plasma density perturbations. Gaining a fuller understanding of this is a challenging task for future studies.

8.2 Outlook

All these open issues motivate us for future investigations. Specifically, we plan to gain further insight into the plasma to neutral dynamical coupling in the MLT region gathering more experimental data obtained by different instruments during the ongoing project ECOMA [*Rapp et al.*, 2005]. The payloads, which will be launched during the next ~three years, will give us a more comprehensive set of the MLT plasma parameters, including density of not only the primary plasma constituents (electrons and ions) but also of the charged aerosols. The role of the charged aerosols in the dynamics of the small-scale process at heights around the mesopause region (its impact on the spectral behavior of the plasma), was theoretically predicted and estimated [see e.g. *Rapp and Lübken*, 2004]; however, simultaneous in situ measurements of the densities of all the plasma constituents, including electrons, ions, and charged aerosols, with high altitude resolution in the same volume, is necessary for an understanding of such phenomena as PMSE or NLC.

The next short-term plans that naturally arise from the presented study are as follows. Using presented turbulence analysis technique we can derive the quantitative turbulence characteristics, the kinetic energy dissipation rate, ε, not only from the neutral density fluctuations but also from the plasma (both electrons and ions) density perturbations. This can be done by fitting a proper spectral model suitable for the power spectra of the plasma density fluctuations. This in turn can be compared with the ε-values derived from the density fluctuations of the neutral gas. A systematic and consistent check can be performed over all the rocket data collected during many years of the soundings at high northern latitudes. The possibility of such a quantitative comparison of the simultaneous in situ measurements performed in the same volume suggests that we can also compare spectra within the PMSE altitude region where plasma is strongly collisionally dominated. The power spectra of the plasma density fluctuations at the PMSE heights depend on the Schmidt number, Sc, as shown in, e.g., *Rapp and Lübken* [2003]. The neutral spectra in turn are free of that dependence. This gives the possibility to derive the Sc altitude profile with very high altitude resolution from the in situ measurements, which has never been done so far with such very high altitude resolution. This result in turn will help to understand the nature of such phenomena as PMSE.

The open questions that can also be addressed in our future soundings include the local morphology of the MLT turbulence. Such questions which are classical for the general turbulence theory, are whether the turbulence is three-dimensional, isotropic, and homogenous. This can be answered by performing horizontal soundings, for example. The next question is the state of development of a turbulence structure. Using time resolving spectral analysis in combination with subsequent (in a short time run) soundings, we plan to gain deeper insight into this problem. Aside from these experimental studies, we also plan to apply our analysis technique to data simulated by *Achatz* [2005]. This will allow us to compare a turbulent structure, which has predefined parameters, a known state of development, and also the source (wave breaking or shear instability), with the measured and analyzed real structure. From the comparison of these structures we anticipate drawing some conclusions about the phase of development of structures detected in the MLT region.

Appendix A

Standard Turbulence Detection Technique

Here the recipe for the derivation of the turbulent energy dissipation rate, ε, from the relative neutral air density fluctuations, according to *Lübken* [1992, 1993, 1997] is presented.

First, we derive power spectrum of a passive and conservative scalar tracer [see e.g. *Lübken*, 1993, for a detiled discussion of different tracers]. Power spectrum is meant to be either the Fourier power spectrum [see e.g. *Jenkins and Watts*, 1969] or global wavelet spectrum [see e.g. *Torrence and Compo*, 1998].

To derive the Fourier spectrum, we perform the following steps.

1. Pad time series with zeros to the next power of two (zero padding), which speeds up the FFT algorithm and decreases edge effect.

2. Multiply time series by Hanning window [see e.g. *Numerical recipes in C, Press et al.*, 1989, p. 553].

3. Use the Fast Fourier Transform (FFT) algorithm to derive the power spectrum itself. Concerning the RSI IDL programming, which we used for the data analysis presented in this manuscript, IDL's implementation of the FFT is based on the Cooley-Tukey algorithm [see e.g. Numerical recipes in C. *Press et al.*, 1989, p. 509].

4. Normalization. According to our algorithm (to get consistent result with calculated model spectrum) the FFT result must be normalized to the variance, σ, of the time series [see e.g. *Lübken*, 1992; *Lübken et al.*, 1993]:
$PSD = |FFT|^2 = \sigma^2$
(IDL's implementation of the FFT keeps this normalization).
Additionally, we normalize the derived power spectrum [see e.g. *Giebeler*, 1995, for details]:

- Because of applied zero padding: $PSD = PSD \cdot \frac{N_{PAD}}{N}$, where N_{PAD} and N are the number of points in the padded and original time series respectively.
- Because of the applied Hanning window: $PSD = PSD \cdot (1.633)^2$.

As pointed out by *Lübken* [1992, 1997] or *Lübken et al.* [1993], we use the "spectral model method" to avoid unambiguities presented in the other methods (e.g. structure function method, see e.g. *Lübken* [1993] for more detailed discussion). We apply the *Heisenberg* [1948] spectral model which describes the inertial and viscous parts of the turbulence energy spectrum and transition between them. In the inertial subrange this model exhibits the classical $k^{-5/3}$ power law, and in the viscous subrange this model obeys the k^{-7} power law. Between these subranges a smooth transition takes place. Fig. 2.1 shows the spectrum as derived from the Heisenberg model. The energy vs frequency spectrum in this model is given by:

$$W(w) = \left[\frac{\Gamma(5/3)\sin(\pi/3)}{2\pi v_R}\right] C_n^2 f_a \left[\frac{(w/v_R)^{-5/3}}{(1+[(w/v_R)/k_0]^{8/3})^2}\right] \tag{A.1}$$

where Γ is the Gamma function ($\Gamma(5/3)$=0.902745), v_R is the rocket velocity. $w = 2\pi f$ is cyclic frequency measured in the rocket domain.

$$C_n^2 = a^2 N_\vartheta / \varepsilon^{1/3} \tag{A.2}$$

is the structure function constant, ε is the turbulent energy dissipation rate, N_ϑ is the variability (or inhomogeneity) dissipation rate [see *Lübken*, 1992, 1993, for more detailed explanation].

The f_a is the normalization factor (we use $f_a = 2$):

$$f_a = \begin{cases} 1, & \text{e.g. } \textit{Tatarskii} \text{ [1971]}, \\ \mathbf{2}, & \text{e.g. } \textit{Lübken} \text{ [1992]}. \end{cases} \tag{A.3}$$

Constant a^2=1.74 was obtained in the laboratory experiments [see e.g. *Lübken*, 1992, 1993, 1997].

The spatial scale (l) at which the transition between the inertial and viscous energy subranges takes place is called *inner scale* (l_0) and is related to the wave number (k_0), corresponding to this transition as:

$$l_0^H \equiv \frac{2\pi}{k_0} \tag{A.4}$$

The superscript H denotes that we use inner scale as defined in the *Heisenberg* [1948] spectral model. This characteristic scale was estimated to be:

$$l_0^H = 9.90 \cdot \eta \tag{A.5}$$

where η is the Kolmogorov microscale given by:

$$\eta = \left(\frac{\nu^3}{\varepsilon}\right)^{1/4} \tag{A.6}$$

So, to calculate the Heisenberg power spectrum from our rocket measurements, we have the following expression:

$$W(2\pi\boldsymbol{f}) = \frac{\Gamma(5/3)\sin(\pi/3)}{2\pi\boldsymbol{v_R}}\; a^2 \frac{N_\vartheta}{\varepsilon^{1/3}} f_a \frac{(2\pi\boldsymbol{f}/\boldsymbol{v_R})^{-5/3}}{\left(1+\left[\left(2\pi\boldsymbol{f}/\boldsymbol{v_R}\right)/\left(2\cdot 9.90\pi\left(\boldsymbol{\nu}^3/\varepsilon\right)^{1/4}\right)\right]^{8/3}\right)^2} \tag{A.7}$$

The bold symbols in Eq. A.7 denote the measured quantities. Two values (ε and N_ϑ) are the unknowns which characterize turbulence and are the final output of this technique. The other values included in Eq. A.7 are the constants described above.

Kinematic viscosity ν can be calculated from the measurements as recommended by the US Standard Atmosphere [*Sissenwine et al.*, 1962]:

$$\nu = \mu/\rho, \qquad \mu = \frac{\beta T^{3/2}}{T+S} \tag{A.8}$$

where μ is the dynamic viscosity; ρ is the mass density of the air; T is temperature; $S = 110.4\ K$ is Sutherland's constant; $\beta = 1.458 \cdot 10^{-6}\ kg/(s \cdot m \cdot K^{1/2})$ is another experimental constant. If there is no measurements available, ν can be derived from the models, like e.g. MSIS [*Hedin*, 1991].

Varying ε and N_ϑ we get different spectra from Eq. A.7. Thus we can fit this calculated spectrum to a measured spectrum using e.g. least square methods [see e.g. *Numerical recipes in C, Press et al.*, 1989]. The parameters ε and N_ϑ which correspond to the best fit are the final output of this technique.

Appendix B

MIDAS/MaCWAVE 2002

B.1 Launch list

Table B.1: The list of the rocket launches during the 1^{st} salvo

Label	date DD-MM-YYYY	time UT	apogee km	FS' mass g	FS' sn
MM-LFS-01	28-06-2002	17:10	88.0	153,3	A02-055
MM-LFS-02	01-07-2002	17:20	87.2	152,3	A02-051
MM-LFS-03	01-07-2002	19:20	84.1	154,3	A02-050
MM-VFS-04	01-07-2002	20:20	102.7	153,2	A02-028
MM-VFS-05	01-07-2002	21.20	108.6	152,8	A02-029
MM-VFS-06	01-07-2002	22:20	103.3	152,2	A02-030
MM-VFS-07	01-07-2002	23:20	104.9	153,6	A02-042
MM-MW-08	01-07-2002	23:56	129.5		
MM-VFS-09	02-07-2002	00:20	103.1	153,1	A02-034
MM-LFS-10	02-07-2002	00:40	86.5	154,8	A02-054
MM-VFS-11	02-07-2002	01:20	101.7	152,6	A02-035
MM-MI-12	02-07-2002	01:44	104.8		
MM-LFS-13	02-07-2002	02:20	86	151,7	A02-052
MM-LFS-14	02-07-2002	03:20	85.6	153,1	A02-053
MM-LFS-15	04-07-2002	19:18	83	154.4	A02-056

Flight label's acronyms:

MM = **M**IDAS/**M**aCWAVE campaign
MI = **MI**DAS payload (instrumented rocket)
MW = **M**aC**W**AVE payload (instrumented rocket)
V = **V**iper motor
L = Super**L**oki motor
FS = **F**alling **S**phere

Table B.2: The list of the rocket launches during the 2^{nd} salvo

Label	date DD-MM-YYYY	time UT	apogee km	FS' mass g	FS' sn
MM-VFS-16	04-07-2002	20:14	103	152.8	A02-040
MM-LFS-17	04-07-2002	20:45	84	154.7	5464
MM-VFS-18	04-07-2002	21:30	100	151.9	A02-032
MM-LFS-19	04-07-2002	22:15	failure	154.9	A02-043
MM-VFS-20	04-07-2002	23:00	failure	153.2	A02-041
MM-VFS-21	04-07-2002	23:20	104	150.5	A02-031
MM-VFS-22	05-07-2002	00:05	105	152.2	A02-030
MM-MW-23	05-07-2002	00:47			
MM-MI-24	05-07-2002	01:10			
MM-MI-25	05-07-2002	01:42			
MM-VFS-26	05-07-2002	02:19	100	153.7	A02-027
MM-VFS-27	05-07-2002	03:00	103	154.0	A02-033
MM-LFS-28	05-07-2002	04:00	86	152.5	5788
MM-LFS-29	05-07-2002	05:00	89	152.7	5787
MM-LFS-30	05-07-2002	06:00	91	152.6	5789
MM-VFS-31	05-07-2002	06:45	101	152.6	A02-039

Flight label's acronyms:

MM = **M**IDAS/**M**aCWAVE campaign
MI = **MI**DAS payload (instrumented rocket)
MW = **M**aC**W**AVE payload (instrumented rocket)
V = **V**iper motor
L = Super**L**oki motor
FS = **F**alling **S**phere

B.2 MIDAS payloads

Table B.3: Instruments onboard MIDAS payloads

MM-MI-12	MM-MI-24	MM-MI-25	Instrument	What Measures
Success	Success	Success	CONE	neutral density
Success	Success	Success	CONE	electron density
Success	Success	Success	PIP	positive ion density
Partly	Absent	Absent	E-field probes	E-field
Absent	Failed	Failed	Faraday Antennas	electron density
Failed	Failed	Failed	CPP	electron temperature
Success	Success	Success	Particle Detector	charged aerosols

Table B.4: Derived (Failed to derive) parameters

MM-MI-12	MM-MI-24	MM-MI-25	Output	Instrument
+	-	-	Neutral temperature	CONE
+	-	-	Absolute neutral density	CONE
+	+	+	Turbulence	CONE
+	+	+	High resolution electron density	CONE
+	+	+	High resolution positive ion density	PIP
-	-	-	Absolute electron density	Faraday
-	-	-	Electron temperature	CPP
+	-	-	Positively charged aerosols	Particle Detector
+	-	-	Negatively charged aerosols	Particle Detector
+	-	-	Electric field (AC)	E-field
-	-	-	Electric field (DC)	E-field

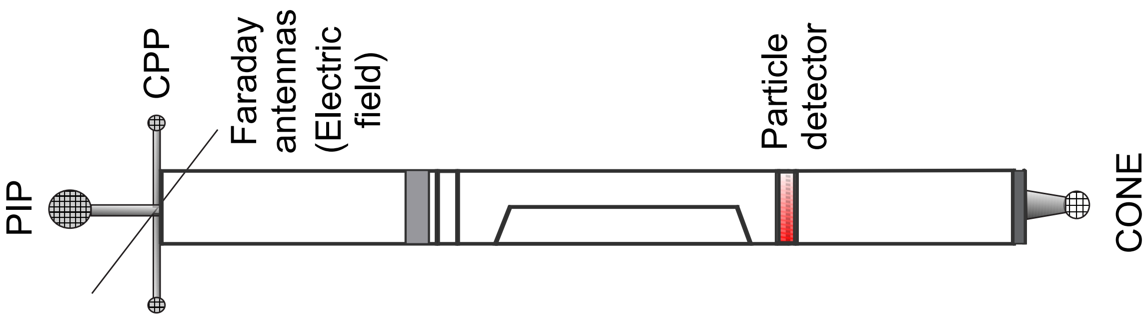

Figure B.1: Instruments onboard the MIDAS payload

Instruments' acronyms:

CPP = **C**old **P**lasma **P**robe
PIP = **P**ositive **I**on **P**robe
CONE = **CO**mbined instrument for **N**eutrals and **E**lectrons

Appendix C

ROMA/SvalRak 2003

C.1 Launch list

Table C.1: The list of the rocket launches during ROMA/SvalRak

Label	date DD-MM-YYYY	time UT	apogee km
RO-MI-01	01-07-2003	09:23	106.6
RO-MI-02	04-07-2003	08:20	101.5
RO-MI-03	06-07-2003	08:27	106.1

Flight label's acronyms:
RO = **RO**MA/SVALRAK campaign
MI = **MI**DAS payload (instrumented rocket)

C.2 MIDAS payloads

Table C.2: Instruments onboard MIDAS payloads

RO-MI-01	RO-MI-02	RO-MI-03	Instrument	What Measures
Success	Success	Success	CONE	neutral density
Success	Failed	Failed	CONE	electron density
Success	Failed	Success	PIP	positive ion density
Failed	Absent	Absent	E-field probes	E-field
Absent	Failed	Success	Faraday Antennas	electron density
Failed	Failed	Success	CPP	electron temperature
Failed	Success	Failed	Particle Detector	charged aerosols

Table C.3: Derived (Failed to derive) parameters

RO-MI-01	RO-MI-02	RO-MI-03	Output	Instrument
-	-	+	Neutral temperature	CONE
-	-	+	Absolute neutral density	CONE
+	+	+	Turbulence	CONE
+	-	-	High resolution electron density	CONE
+	-	+	High resolution positive ion density	PIP
-	-	+	Absolute electron density	Faraday
-	-	+	Electron temperature	CPP
-	+	-	Positively charged aerosols	Particle Detector
-	-	-	Negatively charged aerosols	Particle Detector
-	-	-	Electric field (AC)	E-field
-	-	-	Electric field (DC)	E-field

Bibliography

Achatz, U., On the role of optimal perturbations in the instability of monochromatic gravity waves, *Phys. Fluids*, *17*, 4107, 2005.

Andre, D., and W. Baumjohann, Joint two-dimensional observations of ground magnetic and ionospheric electric fields associated with auroral currents. V - Current system associated with eastward drifting omega bands, *Journal of Geophysics Zeitschrift Geophysik*, *50*, 194–201, 1982.

Andrews, D. G., and M. F. McIntyre, Planetary Waves in Horizontal and Vertical Shear: Asymptotic Theory for Equatorial Waves in Weak Shear., *J. Atmos. Sci.*, *33*, 2049–2053, 1976.

Baldwin, M., T. Hirooka, and S. Yoden, Major stratospheric warming in the Southern Hemisphere in 2002: Dynamical aspects of the ozone hole split, *SPARC Newsl.*, *20*, 2003.

Batchelor, G. K., *The Theory of Homogeneous Turbulence*, The Theory of Homogeneous Turbulence, Cambridge: Cambridge University Press, 1953, 1953.

Batchelor, G. K., Small scale variation of convected quantities like temperature in turbulent field, *J. Fluid Mech.*, *5*, 113–133, 1958.

Becker, E., Direct heating rates associated with gravity wave saturation, *J. Atmos. Terr. Phys.*, *66*, 683–696, 2004.

Becker, E., and G. Schmitz, Interaction between Extratropical Stationary Waves and the Zonal Mean Circulation., *J. Atmos. Sci.*, *58*, 462–480, 2001.

Becker, E., and G. Schmitz, Climatological effects of orography and land-sea heating contrasts on the gravity-wave driven circulation of the mesosphere., *J. Atmos. Sci.*, *60*, 103–118, 2003.

Becker, E., A. Müllemann, F.-J. Lübken, H. Körnich, P. Hoffmann, and M. Rapp, High Rossby-wave activity in austral winter 2002: Modulation of the general circulation of the MLT during the MaCWAVE/MIDAS northern summer program, *Geophys. Res. Lett.*, *31*, 24–+, 2004.

Bennett, F. D. G., J. E. Hall, and P. H. G. Dickinson, D-region electron densities and collision frequencies from faraday rotation and differential absorbtion measurements, *J. Atmos. Terr. Phys.*, *34*, 1321–1335, 1972.

Bilitza, D., IRI 2000, *Radio Sci.*, *36*, 261–276, 2001.

Blamont, J.-E., Turbulence in atmospheric motions between 90 and 130 km of altitude, *Planet. Space Sci.*, *10*, 89–101, 1963.

Blix, T. A., and E. Thrane, Middle atmosphere turbulence at high and middle latitudes, *Proceedings of the 10th ESA Symposium on European Rocket and Balloon Programmes and Related Research, Cannes-Mandelieu, France (ESA SP–317)*, *317*, 437–445, 1991.

Blix, T. A., and E. V. Thrane, Noctilucent Clouds and regions with polar mesospheric summer echoes studied by means of rocket-borne electron and ion DC-probes, *Geophys. Res. Lett.*, *20*, 2303–2306, 1993.

Blix, T. A., E. V. Thrane, and Ö. Andreassen, In situ measurements of fine-scale structure and turbulence in the mesosphere and lower thermosphere by means of electrostatic positive ion probes, *J. Geophys. Res.*, *95(D5)*, 5533–5548, 1990a.

Blix, T. A., E. V. Thrane, S. Kirkwood, and K. Schlegel, Plasma instabilities in the lower E-region observed during the DYANA campaign, *J. Atmos. Terr. Phys.*, *56*, 1853–+, 1994.

Blix, T. A., E. V. Thrane, S. Kirkwood, and K. Schlegel, Plasma instabilities in the lower E-region observed during the DYANA campaign, *J. Atmos. Terr. Phys.*, *56*, 1853–1870, 1994.

Blix, T. A., K. R. Svenes, U.-P. Hoppe, J. Gumbel, and B. Strelnikov, In situ measurements of neutral temperature in the middle atmosphere by means of swept langmuir probes, *35th COSPAR Scientific Assembly 2004*, *presented in poster session C2.5-0038-04*, P0062, 2004.

Blix, T. X., et al., Small scale structure observed in situ during MAC/EPSILON, *J. Atmos. Terr. Phys.*, *52*, 835–854, 1990b.

Cho, J. Y. N., T. M. Hall, and M. C. Kelley, On the role of charged aerosols in polar mesosphere summer echoes, *J. Geophys. Res.*, *97*, 875–886, 1992.

Corrsin, S., On the spectrum of isotropic temperature fluctuations in an isotropic turbulence, *J. Appl. Phys.*, *22, 4*, 469, 1951.

Croskey, C. L., J. D. Mitchell, R. A. Goldberg, T. A. Blix, M. Rapp, R. Latteck, M. Friedrich, and B. Smiley, Coordinated investigation of plasma and neutral density fluctuations and particles during the MaCWAVE/MIDAS summer 2002 program, *Geophys. Res. Lett.*, *31*, 24–+, 2004.

Daubechies, I., The wavelet transform, time-frequency localization and signal analysis, *IEEE Trans. Inf. Theory*, *36(5)*, 961Ũ1005, 1990.

Daubechies, I., *Ten Lectures on Wavelets*, vol. 61 of *CBMS-NSF Regional Conference Series in Applied Mathematics*, Society for Industrial and Applied Mathematics, Philadelphia, 1992.

Driscoll, R. J., and L. A. Kennedy, A model for the turbulent energy spectrum, *Phys. Fluids*, *26*, 1228–1233, 1983.

Eckermann, S. D., On the observed morphology of gravity-wave and equatorial-wave variance in the stratosphere, *J. Atmos. Terr. Phys.*, *57*, 105–134, 1995.

Farge, M., Wavelet transforms and their applications to turbulence, *Annual Review of Fluid Mechanics*, *24*, 395–457, 1992.

Farge, M., N. K.-R. Kevlahan, V. Perrier, and K. Schneider, Turbulence analysis, modelling and computing using wavelets, in *Wavelets in Physics*, pp. 117–+, 1999.

Fejer, B. G., *Natural Ionospheric Plasma Waves*, pp. 216–273, European Geophysical Society, Katlenburg-Lindau, 1996.

Fleming, E. L., S. Chandra, M. R. Schoeberl, and J. J. Barnett, *Monthly mean global climatology of temperature, wind, geopotential height and pressure for 0-120 km*, National Aeronautics and Space Administration, Technical Memorandum 100697, Washington, D.C., 1988.

Fritts, D., C. Bizon, J. Werne, and C. Meyer, Layering accompanying turbulence generation due to shear instability and gravity-wave beraking, *J. Geophys. Res.*, *108*, 2003.

Fritts, D. C., *Gravity waves*, pp. 1308–1314, Academic, San Diego, Calif., 2003.

Gibson, C. H., Fossil turbulence revisited, *J. of Marine Systems*, *21*, 147–167, 1999.

Giebeler, J., In-situ Messungen zur Untersuchung der Rolle von Turbulenz bei der Erzeugung von Radarechos in der polaren Mesosphäre im Sommer, Ph.D. thesis, Bonn University, 1995, BONN-IR-95-28.

Giebeler, J., F.-J. Lübken, and M. Nägele, CONE - a new sensor for in-situ observations of neutral and plasma density fluctuations, *Proceedings of the 11th ESA Symposium on European Rocket and Balloon Programmes and Related Research, Montreux, Switzerland (ESA SP)*, *ESA-SP-355*, 311–318, 1993.

Goldberg, R. A., and D. C. Fritts, Introduction to special section: The MaCWAVE-MIDAS Program to Study the Polar Summer Mesosphere, *Geophys. Res. Lett.*, *31*, 24–+, 2004.

Goldberg, R. A., et al., The MaCWAVE/MIDAS rocket and ground-based measurements of polar summer dynamics: Overview and mean state structure, *Geophys. Res. Lett.*, *31*, 24–+, 2004.

Grossmann, A., and J. Morlet, Decomposition of Hardy functions into square integrable wavelets of constant shape, *SIAM Journal on Mathematical Analysis*, *15*, 723–736, 1984.

Hall, C., T. A. Blix, and E. V. Thrane, Attractor dimensionality for mesospheric turbulence, *J. Geophys. Res.*, *97*, 153–158, 1992.

Hall, C. M., U.-P. Hoppe, T. A. Blix, E. V. Thrane, A. H. Manson, and C. E. Meek, Seasonal variation of turbulent energy dissipation rates in the polar mesosphere: a comparison of methods, *Earth Plan. Space*, *51*, 515–524, 1999.

Hedin, A. E., Extension of the MSIS thermosphere model into the middle and lower atmosphere, *J. Geophys. Res.*, *96*, 1159–1172, 1991.

Heisenberg, W., Zur statistischen Theorie der Turbulenz, *Z. Physik*, *124*, 628–657, 1948.

Hill, R. J., and S. F. Clifford, Modified spectrum of atmospheric temperature fluctuations and its application to optical propagation, *J. Opt. Soc. America*, *68*, 892–899, 1978.

Hillert, W., Untersuchung atmosphärischer Turbulenz in der Mesosphäre und unteren Thermosphäre mit Hilfe von in situ durchgeführten Messungen, Ph.D. thesis, Bonn University, 1992, BONN-IR-92-13.

Hillert, W., F.-J. Lübken, and G. Lehmacher, TOTAL: A rocket-borne instrument for high resolution measurements of neutral air turbulence during DYANA, *J. Atmos. Terr. Phys.*, *56*, 1835–1852, 1994.

Hocking, W. K., The dynamical parameters of turbulence theory as they apply to middle atmosphere studies, *Earth Plan. Space*, *51*, 525–541, 1999.

Höffner, J., C. Fricke-Begemann, and F.-J. Lübken, First observations of noctilucent clouds by lidar at svalbard, 78 °N, *Atmos. Chem. Phys.*, *3*, 1101–1111, 2003.

Holschneider, M., Localization properties of wavelet transforms, *J. Math. Phys.*, *34(7)*, 3227–3244, 1993.

Holton, J. R., The role of gravity wave induced drag and diffusion in the momentum budget of the mesosphere, *J. Atmos. Sci.*, *39*, 791–799, 1982.

Holton, J. R., *An introduction to dynamic meteorology*, Academic Press, Amsterdam, 2004.

Hunsucker, R. D., and J. K. Hargreaves, *The High-Latitude Ionosphere and its Effects on Radio Propagation*, The High-Latitude Ionosphere and its Effects on Radio Propagation, by R. D. Hunsucker and J. K. Hargreaves, pp. 638. ISBN 0521330831. Cambridge, UK: Cambridge University Press, December 2002., 2002.

Jenkins, G. M., and D. G. Watts, *Spectral analysis and its applications*, Holden-Day Series in Time Series Analysis, London: Holden-Day, 1969, 1969.

Jordan, D., R. W. Miksad, and E. J. Powers, Implementation of the continuous wavelet transform for digital time series analysis, *Review of Scientific Instruments*, *68*, 1484–1494, 1997.

Kelley, M. C., and J. C. Ulwick, Large- and small-scale organization of electrons in the high-latitude mesosphere - Implications of the STATE data, *J. Geophys. Res.*, *93*, 7001–7008, 1988.

Kelley, M. C., T. Hall, J. C. Ulwick, J. Roettger, and B. Inhester, Intense turbulence in the polar mesosphere - Rocket and radar measurements, *J. Atmos. Terr. Phys.*, *52*, 875–891, 1990.

Kelley, M. C., C. A. Kruschwitz, C. S. Gardner, J. D. Drummond, and T. J. Kane, Mesospheric turbulence measurements from persistent Leonid meteor train observations, *J. Geophys. Res.*, *108*, 22–+, 2003.

Kolmogoroff, A., The local structure of turbulence in incompressible viscous fluid for very large Reynolds' numbers, *Dokl. Akad. Nauk SSSR*, *30*, 301–305, 1941.

Kumar, P., and E. Foufoula-Georgiou, Wavelet analysis for geophysical applications, *Reviews of Geophysics*, *35*, 385–412, 1997.

Labitzke, K., J. J. Barnett, and B. Edwards, *Middle Atmosphere Program, MAP Handbook, Volume 16*, University of Illinois, Urbana, 1985.

Laframboise, J. G., and L. J. Sonmor, Current collection by probes and electrodes in space magnetoplasmas - A review, *J. Geophys. Res.*, *98*, 337–357, 1993.

Landau, L. D., and E. M. Lifschitz, *Hydrodynamik*, Akadamie-Verlag, Berlin, 1966.

Latteck, R., W. Singer, and H. Bardey, The ALWIN MST radar - technical design and performances, in *Proc. 14th ESA Symp. on European Rocket and Ballon Programmes and Related Research*, edited by B. Kaldeich-Schürmann, vol. ESA SP-437, pp. 179–184, 1999.

Lehmacher, G. A., C. L. Croskey, J. D. Mitchell, M. Friedrich, F.-J. Lübken, M. Rapp, E. Kudeki, and D. C. Fritts, Intense turbulence observed above a mesospheric temperature inversion at equatorial latitude, *Geophys. Res. Lett.*, *33*, 8808–+, 2006.

Lewalle, J., Tutorial on continuous wavelet analysis of experimental data, Syracuse University, 1995.

Lewalle, J., M. Farge, and K. Schneider, *Wavelet Transforms. Section D 1.6.*, p. to appear, Springer-Verlag, 2005.

Lindzen, R. S., Turbulence and stress owing to gravity wave and tidal breakdown, *J. Geophys. Res.*, *86*, 9707–9714, 1981.

Lloyd, K. H., C. H. Low, B. J. McAvaney, D. Rees, and R. G. Roper, Thermospheric observations combining chemical seeding and ground-based techniques -I. winds turbulence and parameters of the neutral atmosphere, *Planet. Space Sci.*, *20*, 761–788, 1972.

Lübken, F. J., TOTAL: A new instrument to study turbulent parameters in the mesosphere and lower thermosphere, in *ESA SP-270: European Rocket & Balloon Programmes and Related Research*, pp. 215–218, 1987.

Lübken, F.-J., On the extraction of turbulent parameters from atmospheric density fluctuations, *J. Geophys. Res.*, *97*, 20,385–20,395, 1992.

Lübken, F.-J., Experimental results on the role of turbulence for the heat budget of the upper atmosphere, Master's thesis, Bonn University, 1993, BONN-IR-93-51.

Lübken, F.-J., Seasonal variation of turbulent energy dissipation rates at high latitudes as determined by insitu measurements of neutral density fluctuations, *J. Geophys. Res.*, *102*, 13,441–13,456, 1997.

Lübken, F.-J., Thermal structure of the arctic summer mesosphere, *J. Geophys. Res.*, *104*, 9135–9150, 1999.

Lübken, F.-J., W. Hillert, G. Lehmacher, and U. von Zahn, Experiments revealing small impact of turbulence on the energy budget of the mesosphere and lower thermosphere, *J. Geophys. Res.*, *98*, 20,369–20,384, 1993.

Lübken, F.-J., M. Rapp, and P. Hoffmann, Neutral air turbulence and temperatures in the vicinity of polar mesosphere summer echoes, *J. Geophys. Res.*, *107(D15)*, 4273–4277, 2002.

Mazaudier, C., C. Senior, and E. Nielsen, Global convection electric field and current - Comparisons between model's predictions and data from STARE, Saint-Santin, and magnetometers, *J. Geophys. Res.*, *92*, 5991–5999, 1987.

Meyer, W., Investigations on large and small scale dynamic processes in the mesosphere and upper stratosphere by means of wind and density measurements above northern Scandinavia in the framework of the MAP/WINE Project, *Ph.D. Thesis*, 1988.

Müllemann, A., Temperaturen, Winde und Turbulenz in der polaren Sommermesosphäre, Ph.D. thesis, Leibniz-Institut für Atmospärenphysik, 2004, Kühlungsborn-ISSN 1615-8083.

Müllemann, A., M. Rapp, F.-J. Lübken, and P. Hoffmann, In situ measurements of mesospheric turbulence during spring transition of the Arctic mesosphere, *Geophys. Res. Lett.*, *29*, 115–1, 2002.

Müllemann, A., M. Rapp, and F.-J. Lübken, Morphology of turbulence in the polar summer mesopause region during the MIDAS/SOLSTICE campaign 2001, *Adv. Space Res.*, *31*, 2069–2074, 2003.

Novikov, E. A., The energy spectrum of incompressible turbulent flow, *Dokl. Akad. Nauk SSSR*, *139*, 331–334, 1961.

Oboukhov, A. M., Structure of the temperature field in the turbulent flow, *News of the AN SSSR, Geographics and Geophysics*, *13, 1, 58*, 1949.

Perrier, V., T. Philipovitch, and C. Basdevant, Wavelet spectra compared to Fourier spectra, *Journal of Mathematical Physics*, *36*, 1506–1519, 1995.

Press, W. H., B. P. Flannery, S. A. Teukolsky, and W. T. Vetterling, *Numerical recipes in C. The art of scientific computing*, Cambridge: University Press, 1989, 1989.

Rapp, M., and F.-J. Lübken, On the nature of PMSE: Electron diffusion in the vicinity of charged particles revisited, *J. Geophys. Res.*, *108(D8)*, 8437, 2003.

Rapp, M., and F.-J. Lübken, Polar mesosphere summer echoes (PMSE): Review of observations and current understanding, *Atmos. Chem. Phys.*, *4*, 2601–2633, 2004.

Rapp, M., J. Gumbel, and F.-J. Lübken, Absolute density measurements in the middle atmosphere, *Ann. Geophys.*, *19*, 571–580, 2001.

Rapp, M., F.-J. Lübken, A. Müllemann, G. E. Thomas, and E. J. Jensen, Small scale temperature variations in the vicinity of NLC: Experimental and model results, *J. Geophys. Res.*, *107(D19)*, doi: 10.1029/2001JD001,241, 2002.

Rapp, M., B. Strelnikov, A. Müllemann, F.-J. Lübken, and D. C. Fritts, Turbulence measurements and implications for gravity wave dissipation during the MaCWAVE/MIDAS rocket program, *Geophys. Res. Lett.*, *31*, 24–+, 2004.

Rapp, M., J. Hedin, I. Strelnikova, M. Friedrich, J. Gumbel, and F.-J. Lübken, Observations of positively charged nanoparticles in the nighttime polar mesosphere, *Geophys. Res. Lett.*, *32*, 23,821–+, 2005.

Rees, D., R. G. Roper, K. H. Lloyd, and C. H. Low, Determination of the structure of the atmosphere between 90 and 250 km by means of contaminant releases at Woomera, May 1968, *Phil. Trans. R. Soc. Lond.*, *271*, 631–663, 1972.

Roper, R. G., Dissipation of wind energy in the height range 80 to 140 kilometers, *J. Geophys. Res.*, *71*, 4427–4428, 1966.

Röttger, J., and C. La Hoz, Characteristics of polar mesosphere summer echoes (PMSE) observed with the EISCAT 224 MHz radar and possible explanations of their origin, *Journal of Atmospheric and Terrestrial Physics*, *52*, 893–906, 1990.

Rüster, R., J. Röttger, G. Schmidt, P. Czechowsky, and J. Klostermeyer, Observations of Mesospheric Summer Echoes at VHF in the Polar Cap Region, *Geophys. Res. Lett.*, *28*, 1471–1474, 2001.

Rycroft, M. J., G. M. Keating, and D. Rees, Upper atmosphere models and research; Proceedings of Workshops X and XI and the Topical Meeting of the 27th COSPAR Plenary Meeting, Espoo, Finland, July 18-29, 1988, *Adv. Space Res.*, *10*, 1990.

Sato, T., Radar Principles, in *Middle Atmosphere Program. Handbook for MAP. Volume 30*, edited by S. Fukao, pp. 19–+, 1989.

Schmidlin, F. J., Derivation and application of temperature corrections for the United States radiosonde, in *Symposium on Meteorological Observations and Instrumentations, 7th, New Orleans, LA, Jan. 14-18, 1991, Preprints (A92-32051 12-47). Boston, MA, American Meteorological Society, 1991, p. 227-231.*, pp. 227–231, 1991.

Schmidlin, F. J., H. S. Lee, and W. Michel, The inflatable sphere - A technique for the accurate measurement of middle atmosphere temperatures, *J. Geophys. Res.*, *96*, 22,673–+, 1991.

Schunk, R. W., and A. F. Nagy, Ionospheres, *Ionosphere*, 2004.

Singer, W., R. Latteck, P. Hoffman, B. P. Williams, D. C. Fritts, Y. Murayama, and K. Sakanoi, Tides near the Arctic summer mesopause during the MaCWAVE/MIDAS summer program, *Geophys. Res. Lett.*, *32*, 7–+, 2005.

Sissenwine, N., M. Dubin, and H. Wexler, The U. S. Standard Atmosphere, 1962, *J. Geophys. Res.*, *67*, 3627–+, 1962.

Smith, L. G., *Middle Atmosphere Program, 8, Electron density measurements in the middle atmosphere by radio propagation technique*, vol. 19, SCOSTEP, University of Illinios, 1406 W. Green Street, Urbana, Illinois 61801, 1986.

St.-Maurice, J.-P., C. Cussenot, and W. Kofman, On the usefulness of E region electron temperatures and lower F region ion temperatures for the extraction of thermospheric parameters: a case study, *Annales Geophysicae*, *17*, 1182–1198, 1999.

Strelnikov, B., M. Rapp, and F.-J. Lübken, A new technique for the analysis of neutral air density fluctuations measured in situ in the middle atmosphere, *Geophys. Res. Lett.*, *30*, 2052, doi:10.1029/2003GL018,271, 2003.

Strelnikov, B., M. Rapp, T. A. Blix, and M. Friedrich, In situ observations of small plasma processes in the lower E-region at 79 °N, in *ESA SP-590: 17th ESA Symposium on European Rocket and Balloon Programmes and Related Research*, 2005.

Strelnikov, B., M. Rapp, T. A. Blix, N. Engler, J. Höffner, J. Lautenbach, F.-J. Lübken, B. Smiley, and M. Friedrich, In situ observations of small scale neutral and plasma dynamics in the mesosphere/lower thermosphere at 79°N., *Adv. Space Res.*, *38*, 2388–2393, doi:10.1016/j.asr.2005.03.097, 2006.

Strelnikov, B., M. Rapp, F.-J. Lübken, N. Engler, T. A. Blix, M. Friedrich, and T. K. Yeoman, In situ observations of an E-region plasma instability: A case study., *Ann. Geophys.*, *to be submitted*, 2007.

Svenes, K. R., T. A. Blix, U.-P. Hoppe, J. Gumbel, and B. Strelnikov, In-situ measurements of neutral temperature in the middle atmosphere by using electrons as proxy, in *ESA SP-590: 17th ESA Symposium on European Rocket and Balloon Programmes and Related Research*, 2005.

Sweldens, W., and P. Schröder, Building your own wavelets at home, in *Wavelets in Computer Graphics*, pp. 15–87, ACM SIGGRAPH Course notes, 1996.

Tatarskii, V. I., *The effects of the turbulent atmosphere on wave propagation*, Jerusalem: Israel Program for Scientific Translations, 1971.

Thrane, E., T. Blix, U.-P. Hoppe, F.-J. Lübken, W. Hillert, G. Lehmacher, and D. Fritts, A study of small-scale waves and turbulence in the mesosphere using simultaneous *in situ* observations of neutral and plasma fluctuations, *J. Atmos. Terr. Phys.*, *56*, 1797–1808, 1994.

Thrane, E. V., *Middle Atmosphere Program, 6, DC-probe measurements in the middle atmosphere*, vol. 19, SCOSTEP, University of Illinios, 1406 W. Green Street, Urbana, Illinois 61801, 1986.

Thrane, E. V., and B. Grandal, Observations of fine scale structure in the mesosphere and lower thermosphere, *J. Atmos. Terr. Phys.*, *43*, 179–189, 1981.

Thrane, E. V., et al., Small scale structure and turbulence in the mesosphere and lower thermosphere at high latitudes in winter, *J. Atmos. Terr. Phys.*, *49*, 751–762, 1987.

Torrence, C., and G. P. Compo, A practical guide to wavelet analysis, *Bull. of the Am. Met. Soc.*, *79*, 61–78, 1998.

Ulwick, J. C., K. D. Baker, M. C. Kelley, B. B. Balsley, and W. L. Ecklund, Comparison of simultaneous MST radar and electron density probe measurements during STATE, *J. Geophys. Res.*, *93*, 6989–7000, 1988.

von Weizsäcker, C., Das Spektrum der Turbulenz bei großen Reynoldsschen Zahlen, *Z. Physik*, *124*, 614–627, 1948.

Weinstock, J., Analytical approximations in the theory of turbulent diffusion, *Physics of Fluids*, *21*, 887–890, 1978.

Yaglom, A. M., About the local structure of the temperature field in the turbulent flow, *Report of the AN SSSR*, *69, 6, 743*, 1949.

Zimmerman, S. P., and K. S. W. Champion, Transport processes in the upper atmosphere, *J. Geophys. Res.*, *68*, 3049–3056, 1963.

Zimmerman, S. P., and E. A. Murphy, *Stratospheric and mesospheric turbulence*, pp. 35–47, D. Reidel Publ. Comp., Dordrecht, Holland, 1977.

Acknowledgments

I thank my supervisor, PD Dr. Markus Rapp, for inestimable help and all-round support during my work on the thesis. I am grateful to Prof. Franz-Josef Lübken for giving me the excellent possibility to work in his sounding-rocket group which enabled me to produce the results of this thesis. I thank Hans-Jürgen Heckl, an excellent master of the hardware for our experiments. I also thank Arno Müllemann who helped me to start my work.

I thank Dr. Tom Arild Blix, his team from FFI (Stig Karsrud, Vidar Killingmo, Terje Angeltveit), and Prof. Martin Friedrich from Technical University of Graz, for their brilliant collaboration and pleasant companion during rocket campaigns.

I also thank Prof. Jörg Gumbel and his Middle Atmosphere Group of MISU at Stockholm University for different types of collaboration and their help in extending my knowledge in atmospheric science.

I thank the DLR-Moraba (Mobile rocket base) and the staff of the Andøya Rocket Range who are an inseparable part of our rocket-based research.

I thank all the IAP staff for the friendly environment, for many insightful conversations during the development of the ideas in this thesis, and for helpful comments on the text.

I specially thank Frau Roswitha Mehl for her inestimable help in our accommodation in Kühlungsborn.

I also thank all German friends of mine and of my family for their friendship and best-side introduction of German culture.

I specially thank Hägar Holste for his incredible help in submitting my thesis by taking care of all the bureaucracy at the time of my stay in Northern Norway during another sounding rocket campaign.

Finally, I also appreciate Prof. Grossmann's willingness to review this thesis.

Summary

In situ measurements of small scale irregularities of neutral air and plasma constituents were performed in the polar summer mesosphere using sounding rockets. Two campaigns were carried out, one at Andøya (69 °N) and one at Svalbard (79 °N). Small scale irregularities were analyzed using wavelet methods, hence allowing a yet unprecedented altitude resolution of neutral air turbulence parameters and plasma instability structures. Measurements performed at Andøya provided strong and compelling evidence for a disturbed residual circulation as revealed in the altitude distribution of mesospheric turbulence, and the thermal and dynamical structure, i.e., temperatures and winds. This disturbed state was presumably caused by an extraordinarily strong Rossby-wave activity in the southern hemisphere. Measurements at Svalbard provided the first in situ information on mesospheric turbulence at such high latitudes and indicated that turbulence becomes weaker towards the pole, in agreement with predictions of state-of-the art general circulation models. During the same rocket flights, comprehensive information was obtained on the characteristics of plasma parameters in the presence of simultaneously measured strong radar echoes from the mesopause region, known as polar mesosphere summer echoes. Finally, measurements of plasma parameters at altitudes above 90 km resulted in a comprehensive characterization of E-region plasma parameters, in terms of electron- and positive ion fluctuation amplitudes and electron temperature profiles. In particular, the (first) simultaneous measurement of neutral- and electron temperatures provides and excellent opportunity to test existing theories of these instabilities.

Zusammenfassung

Im Rahmen zweier Messkampagnen in Andøya (69 °N) und Svalbard (79 °N) wurden in situ Messungen von kleinskaligen Neutralgas- und Plasmaparametern im Höhenbereich der Mesopausenregion durchgeführt. Diese kleinskaligen Strukturen wurden erstmalig mit Hilfe von Wavelets auf ihren spektralen Gehalt analysiert. Diese neue Methode ermöglicht es erstmalig die Höhenstruktur von Turbulenz und Plasmainstabilitäten in der mittleren Atmosphäre auf vertikalen Skalen von <100 m zu analysieren und damit einen Einblick in die wirkliche Ausdehnung solcher atmosphärischer Zellen zu erlangen. Die Messungen in Andoya ergaben überzeugende Hinweise auf eine gestörte residuelle Zirkulation, was sich in gemessenen Turbulenzprofilen und Temperaturen und Winden belegen ließ und auf eine erhöhte planetare Wellenaktivität auf der südlichen Hemisphäre zurückgegführt werden konnte. Die Messungen in Svalbard ergaben die ersten experimentellen Ergebnisse zur Höhenverteilung von Turbulenz in sehr hohen polaren Breiten und weisen darauf hin, dass die Turbulenzstärke zum Pol hin abnimmt. Dieses experimentelle Ergebnisse wird durch Vorhersagen von generellen Zirkulationsmodellen unterstützt. Während derselben Flüge wurden hochaufgelšte Messungen von Elektronen- und Ionendichten in der Umgebung von starken Radarechos durchgeführt, die auch als Polare Mesopshären Sommer Echos bekannt sind. Zum Schluš konnten in Höhen von oberhalb 90 km Plasmainstabilitäten in der E-Schicht durch Messungen von Elektronen- und Ionenfluktuationen und Elektronen- und Neutralgastemperaturen charakterisiert werden. Insbesondere die (erstmaligen) gleichzeitigen Temperaturmessungen sowohl geladener als auch neutraler Atmosphärenbestandteile bieten eine herausragende Gelegenheit, unser derzeitiges Verständnis dieser Instabilitäten zu überprüfen.

Erklärung

Hiermit versichere ich, dass ich die vorliegende Arbeit selbstständig angefertigt und ohne fremde Hilfe verfasst habe, keine außer den von mir angegebenen Hilfsmitteln und Quellen dazu verwendet habe und die den benutzten Werken inhaltlich oder wörtlich entnommenen Stellen als solche kenntlich gemacht habe.

Die Arbeit wurde bisher weder im Inland noch im Ausland in gleicher oder ähnlicher Form einer anderen Prüfungsbehörde vorgelegt. Weiterhin erkläre ich, dass ich ein Verfahren zur Erlangung des Doktorgrades an keiner anderen wissenschaftlichen Einrichtung beantragt habe.

Kühlungsborn, den 23. August 2006

Lebenslauf

Name	Boris Strelnikov
Geburtsdatum	15.09.1975
Geburtsort	Omsk, Russland
Familienstand	verheiratet
Staatsangehörigkeit	Russisch
Wohnsitz	Omsk, Russland
Nebenwohnsitz	Kühlungsborn, Deutschland
1983 – 1990	Allgemeinbildende Mittelschule Nr. 66 in Omsk
1990 – 1992	Physikalisch-mathematische Schule Nr. 64 in Omsk
Juni 1992	Abitur
1992 – 1998	Studium an der Omsker Staatliche Universität, Omsk, Russland, Studiengang: Diplom Physik
1997 – 1998	Diplomarbeit in Plasmaphysik in der Omsker Staatlichen Universität zum Thema: "HFI-Entladung und ihre Anwendung bei heterogenen plasmachemischen Prozessen"
Juni 1998	Diplom in Physik
1998 – Oktober 2001	Aspirant in der Omsker Staatlichen Universität
seit Januar 2002	Promotion im Studienfach Physik am Leibniz-Institut für Atmosphärenphysik an der Universität Rostock e.V., Anfertigung der Dissertation